INFLUENCE OF THE MICROSTRUCTURE ON THE CREEP BEHAVIOUR OF SEMI-SOLID PROCESSED MAGNESIUM-ZINC ALLOYS

Vom Promotionsausschuss der
Technischen Universität Hamburg-Harburg
zur Erlangung des akademischen Grades
Doktor-Ingenieurin (Dr.-Ing.)
genehmigte Dissertation

von
Emma Deyanira Morales Garza

aus
Monterrey, Mexiko

2013

Erster Gutachter: Prof. Dr.-Ing. Karl Ulrich Kainer

Zweiter Gutachter: Prof. Dr.-Ing. Joachim Albrecht

Vorsitzender des Prüfungsausschusses: Prof. Dr.-Ing. Wolfgang Hintze

Tag der mündlichen Prüfung: 14.06.2012

SUMMARY

In the automotive industry the currently used magnesium components are made with AM and AZ alloys and are mainly manufactured by high pressure die casting processes. These alloys, however, are prone to creep failure above temperatures of 120°C precluding them from further automotive applications, where the operative temperature can approach or even exceed 150°C. Most of the compositions proposed for these applications are excluding aluminum but including rare earth elements, reaching excellent creep properties, but being expensive and/or difficult to cast. Low-cost alternative candidates are Zn-based magnesium alloys enhanced with rare earths and/or calcium. Semi-solid processing not only enables to cast these alloys but has the advantages of lower energy consumption, lower porosity, net-shape formed parts and fine microstructures.

The main aim of this work is to find a relationship between the semi-solid cast microstructure and the creep properties of two low-cost zinc-containing magnesium alloys. The first studied alloy, referred as MEZ, is based on the Mg-Zn-RE-Zr system, while the second, referred as ZECa, is a novel promissory composition based on the Mg-Ca-Zn system, with additions of RE and Sr. Creep tensile tests over the temperature range from 135 to 200°C and 50 to 100 MPa were conducted and evaluated in the thixocast state in order to understand the creep mechanisms. The good creep resistance was mainly attributed to the bimodal microstructure reached after thixocasting preventing grain boundary sliding. For the MEZ alloy, low creep rates based on dislocation climb on the basal plane even for high stresses are observed up to 175°C. Above this temperature cross slip from basal to the prismatic plane sets in. The creep mechanism of the ZECa remains dislocation climb on the basal plane up to the investigated temperature of 200°C. An application of this alloy is promising up to about 175°C and about 80 MPa, up to which no tertiary creep sets in. Above these temperatures grain boundary sliding sets in, induced by thermal softening of the ternary $Mg_6Zn_3Ca_2$ phase. Even though the ZECa alloy shows higher minimal creep rates than the MEZ alloy, the ZECa alloy is a promissory material where initial loading plays an important role, like in the case of bolted connections in power train components because of its lower primary creep values.

ACKNOWLEDGMENTS

First of all, I want to thank my academic supervisor, Prof. Dr. Karl U. Kainer, for giving me the opportunity to join his magnesium group as his Ph.D. student in its early stages of formation and for the patient supervision of this work.

Many, many thanks also to Dr. Norbert Hort, head of my former department, for the numerous reviews of the draft thesis. Special thanks to Dr. Hajo Dieringa for his help with the creep experimentation and for the suggestions and corrections on the written work. Thanks to Dr. Yuanding Huang for helping with the Transmission Electron Microscopy analysis. Special thanks to Mr. Volker Kree for his valuable support, advices and, last but not least, good mood during the many hours of metallographic preparation and etching of the magnesium samples. Thanks also to Mr. Volker Ventzke for giving me the opportunity to use the Scanning Electron Microscopy facilities. Thanks to Dr. Carsten Blawert, from the corrosion department where I happily worked for some years, for the suggestions on the experimental setup and for his constant encouragement words.

Special acknowledgments should be mentioned to Leichtmetall Kompetenz Zentrum (LKR) in Austria for providing the facilities for casting of the magnesium samples.

Thanks to the German Academic Exchange Service (DAAD) for giving me the financial support with a scholarship to start this work.

Thanks to all my beloved friends who supported me with their smiles and words during the long way of this work from the very beginning to the very end: Enrique Martínez, Rodolfo González, Enrique Meza, Israel Martínez and Rosario Silva.

Thanks to my family, especially to my dear cousin Juany for being always there, at the other side of the computer and telephone, through the sunny and the stormy days of my stay in Germany.

Finally, I want to specially thank my husband, Nico, for his tireless motivation through the years, for the many days and nights dedicated to discuss this work, for his valuable suggestions to improve it, and for his strong patience and love.

This work is dedicated with all my love to my little prince and sunshine, Felix, who was the final motivation to bring it to an end.

TABLE OF CONTENTS

1 INTRODUCTION 1

2 LITERATURE OVERVIEW 3

2.1 Fundamentals of magnesium 3

2.1.1 Deformation mechanisms of magnesium 3

2.1.2 Influence of alloying on pure magnesium 6

2.2 Fundamentals of creep 8

2.2.1 Creep in metallic materials 8

2.2.2 Diffusional creep 10

2.2.3 Dislocation creep 10

2.2.4 Grain boundary sliding 11

2.3 Creep in pure magnesium 12

2.4 Creep resistance and strengthening in magnesium alloys 14

2.4.1 Magnesium - calcium alloys 15

2.4.2 Magnesium - zinc alloys 15

2.4.3 Magnesium - calcium - zinc alloys 17

2.4.4 Magnesium - rare earths alloys 18

2.4.4.1 Magnesium - rare earths (cerium subgroup) - zinc alloys 20

2.4.4.2 Magnesium - rare earths (yttrium subgroup) - zinc alloys 21

2.5 Casting of magnesium alloys 24

2.5.1 Conventional casting methods 24

2.5.2 Semi-solid processing 25

2.5.3 Feedstock material in the thixocasting process 29

3 AIMS AND OBJECTIVES 31

4 EXPERIMENTAL METHODS 32

4.1 Feedstock material and its processing 32

4.1.1 Extruded feedstock material 32
4.1.2 Partial remelting of the extruded alloys 32
4.1.3 Semi-solid casting of the extruded alloys 33
4.1.4 Aging of the thixocast alloys 34
4.2 Characterization techniques 35
4.2.1 Differential thermal analysis 35
4.2.2 X-ray diffraction 35
4.2.3 Metallographic sample preparation 35
4.2.4 Optical microscopy 36
4.2.5 Scanning electron microscopy (SEM) coupled with EDX 37
4.2.6 Transmission electron microscopy (TEM) 37
4.3 Mechanical tests of the thixocast alloys 38
4.3.1 Hardness tests 38
4.3.2 Tensile and compression tests 38
4.3.3 Tensile creep 38
5 MICROSTRUCTURAL CHARACTERIZATION 40
5.1 MEZ-System 40
5.1.1 Characterization of the extruded feedstock material 40
5.1.1.1 Hardness and chemical composition 40
5.1.1.2 Microstructure 40
5.1.1.3 Phase identification 41
5.1.2 Characterization of the extruded material during its partial remelting 42
5.1.2.1 DTA analysis 43
5.1.2.2 Microstructural evolution 44
5.1.2.3 Grain size evolution 47
5.1.3 Characterization of the thixocast material 48
5.1.3.1 Chemical composition 48

5.1.3.2 Microstructure at lower magnification 48
5.1.3.3 Microstructure 50
5.1.3.4 Phase identification 53
5.2 ZECa-System 55
5.2.1 Characterization of the extruded feedstock material 55
5.2.1.1 Hardness and chemical composition 55
5.2.1.2 Microstructure 55
5.2.1.3 Phase identification 56
5.2.2 Characterization of the extruded material during its partial remelting 59
5.2.2.1 DTA analysis 59
5.2.2.2 Microstructural evolution 59
5.2.2.3 Grain size evolution 63
5.2.3 Characterization of the thixocast material 64
5.2.3.1 Chemical composition 64
5.2.3.2 Microstructure at lower magnification 64
5.2.3.3 Microstructure 66
5.2.3.4 Phase identification 68
6 MECHANICAL BEHAVIOUR OF THE THIXOCAST MATERIAL 71
6.1 MEZ-System 71
6.1.1 Mechanical properties at room temperature 71
6.1.1.1 Hardness tests, tension and compression tests 71
6.1.1.2 Microstructural analysis of deformed samples 72
6.1.2 Microstructural stability with temperature 75
6.1.2.1 Hardness evolution after aging 75
6.1.2.2 Microstructural evolution after aging 76
6.1.3 Creep behaviour 78
6.1.3.1 Creep curves 78

6.1.3.2 Microstructural evolution after creep 80
6.2 ZECa-System 88
6.2.1 Mechanical properties at room temperature 88
6.2.1.1 Hardness, tension and compression tests 88
6.2.1.2 Microstructural analysis of deformed samples 89
6.2.2 Microstructural stability with temperature 92
6.2.2.1 Hardness evolution after aging 92
6.2.2.2 Microstructural evolution after aging 92
6.2.3 Creep behaviour 93
6.2.3.1 Creep curves 93
6.2.3.2 Microstructural evolution after creep 96
7 DISCUSSION 102
7.1 Microstructural evolution during processing 102
7.1.1 Feedstock extruded material 102
7.1.2 Partial remelting of the extruded material 103
7.1.3 Thixocast material 105
7.2 Mechanical properties at room temperature 108
7.2.1 Thixocast MEZ alloy 110
7.2.2 Thixocast ZECa alloy 111
7.3 Determination of the stress exponent and activation energy 113
7.3.1 Creep rate analysis of the thixocast MEZ alloy 113
7.3.2 Creep rate analysis of the thixocast ZECa alloy 115
7.4 Creep mechanisms 118
7.4.1 Creep of the thixocast MEZ alloy 118
7.4.2 Creep of the thixocast ZECa alloy 121
8 CONCLUSIONS 124
9 BIBLIOGRAPHY 126

1 INTRODUCTION

The currently used automotive magnesium components, including instrument panels, steering wheel armatures, steering column supports, seats, valve covers, and transfer cases are mainly manufactured by high pressure die casting processes with the conventional magnesium alloys (AM and AZ alloys). However, the poor resistance to creep above temperatures of 120°C precludes theses alloys from further automotive applications, e.g. power train components, such as engine blocks and automatic transmission cases, where the operative temperature can approach or even exceed 150°C with the presence of cyclical thermal and mechanical loadings [03Pek]. Several aluminium based alloys with higher creep resistance than AZ alloys such as aluminium-rare earths (AE) alloys were proposed. However, it has been found that sufficient creep resistance is limited up to temperatures of about 150°C [01Pow].

The search of creep resistant magnesium alloys for automotive engine components has continued afterwards and different alloying systems have been proposed since then. Promising candidates are Zn containing alloys, which have shown to have better high temperature performance than equivalent Mg-Al alloys [00Kin]. Zinc has a high hardening potential in magnesium. An alloy with high creep resistance, known as MEZ alloy, was presented by Magnesium Elektron on the basis of Mg-RE-Zn. The creep resistance in the pressure die cast state has proven to be significantly superior to AE alloys; however, a relatively poor strength at room temperature and a relatively fast onset of tertiary creep were observed [03Mor], which could be traced back to microstructural defects due to the casting process.

Zinc-based alloys show low castability due to the high shrinkage of the Mg-Zn system, leading to porosity in the casting. Therefore, the semi-solid casting process has been considered as an alternative. In this process the material is cast at a temperature between liquidus and solidus in a partially solid state, thus providing a lower amount of turbulences and less shrinkage, resulting in lower porosity. Additionally, the lower casting temperature reduces energy costs and increases the lifetime of casting equipment. Furthermore, the microstructure can be controlled to a certain extent by precursor material and the casting conditions, which can have a significant influence on the mechanical properties of the part.

On the other hand, prerequisite for the semi-solid-process is a material with a suitable globular microstructure, precluding cast material as direct precursor material. Consequently, a variety of methods have been developed in order to produce a globular microstructure. These methods are usually highly costly when implemented into a mass production. Recently, it was demonstrated on aluminum alloys that a suitable globular microstructure forms on cast and extruded material upon simple heating into the semi-solid range [04Kle, 05Seo, 05Kli].

Another alloying system, with the potential to further reduce alloying costs is Mg-Ca-Zn. Ca shall provide good castability and improve creep resistance. This system is known to have high hardening potential, and the microstructure at different compositions has been well characterized [01Lar, 04Jar, 04Zil, 05Gao]. High yield and ultimate strength in combination with good ductility were detected on squeeze cast material and semi-solid squeeze cast material [98Cha]. However, no systematic study of the creep behaviour exists.

Therefore, the route of using extruded material in a semi-solid casting process is applied in the present work to produce creep resistant magnesium-zinc-rare earths alloys with refined microstructure. For this purpose, the alloy MEZ (Mg-2.6wt%RE-0.4Zn-0.13Mn-0.12Zr) is chosen as a reference and is compared to a novel proposed alloy composition based on the magnesium-zinc-calcium system enhanced with RE and Sr (Mg-2.8Zn-1.9Ca-0.32RE-0.08Sr), further referred as ZECa.

The microstructure of the feedstock material after reheating at different temperatures and times has been analyzed to confirm and understand the formation of globular microstructure before casting. The microstructure of the thixocast alloys after deformation at room temperature and after creep has been studied to understand the creep mechanismus identified after calculation of creep parameters. The creep properties are compared with those of the state of the art die cast alloy AE42 to show the improvement of creep resistance achieved with thixocasting of magnesium-zinc alloys.

2 LITERATURE OVERVIEW

2.1 Fundamentals of magnesium

2.1.1 Deformation mechanisms of magnesium

Pure magnesium has a close-packed hexagonal crystal structure with a measured axial ratio c/a of 1.6236, quite close to the ideal value of 1.633 [67Par]. The close-packed hexagonal structure has a low symmetry and as a consequence the number of slip systems that can be activated simultaneously is limited. A slip system consists of a slip plane, which is the plane of maximum atomic density, and of a slip direction, which is the closest-packed direction within the slip plane. Fig. 1 shows the main slip planes and directions of magnesium crystal [81Yoo]. The slip systems of hexagonal metals are shown in Table 1.

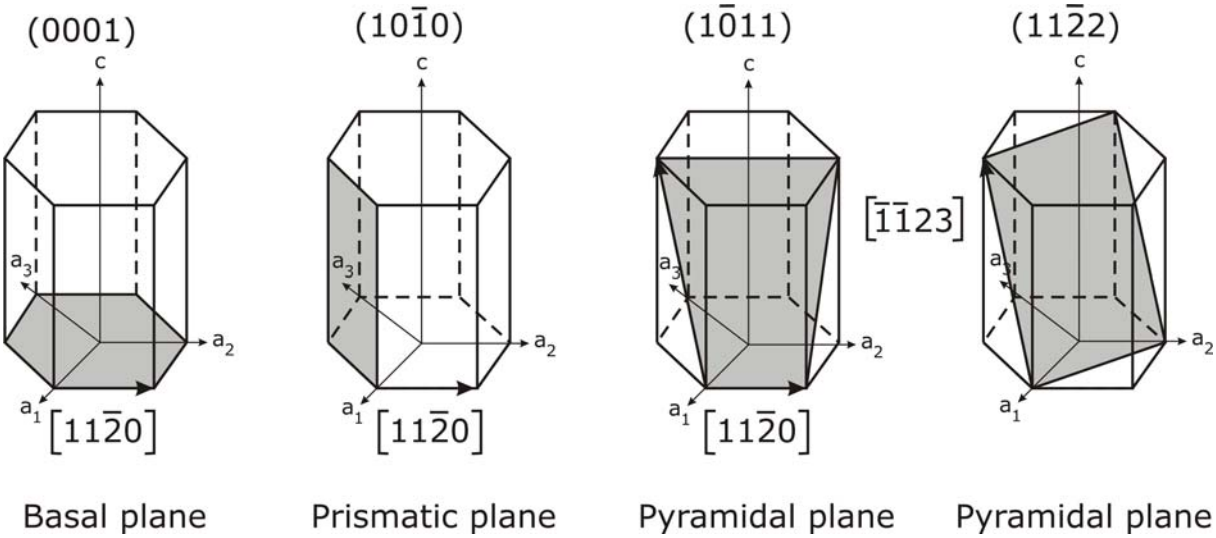

Fig. 1 : Lattice structure of magnesium crystal showing its main slip planes [81Yoo] (light grey, assigned in round brackets) and directions (in rectangular brackets).

The movement of a dislocation along a slip plane is the onset of the plastic deformation of a crystal. The stress required to move a dislocation is called critical resolved shear stress (CRSS). At low temperatures, the CRSS for the prismatic slip in magnesium is two orders of magnitude higher than the CRSS for basal slip [81Yoo]. As a result, the basal plane is the main slip plane at room temperature, leading to slip without any significant hardening [98Num]. According to Taylor, subsequently to von Mises too, at least five independent slip systems must operate in polycrystalline materials to allow uniform deformation without failure at grain boundaries [81Yoo]. The basal plane has only three geometrical and two

independent slip systems and therefore non-basal slip as well as twinning need to be active.

Magnesium exhibits therefore a propensity for mechanical twinning. Twinning supports dislocation controlled plastic deformation by changing the orientation of grains which are unfavourably oriented with regard to basal glide [67Par]. At room temperature, primary twinning occurs predominantly across the pyramidal {$10\bar{1}2$} planes in the ‹$10\bar{1}1$› direction. Secondary twinning occurs typically across the {$30\bar{3}4$} planes [81Yoo]. However, the plastic deformation allowed by twinning is limited. Twinning in the {$10\bar{1}2$} direction can produce only a 7% axial strain in any given grain [05Agn], which explains the low ductility of magnesium in tensile load at room temperature.

Table 1 : Independent slip systems in h.c.p. metals after [67Par].

Slip system	Burgers vector type	Slip direction	Slip plane	Number of slip systems	
				Total	Independent
1	a	<$11\bar{2}0$>	basal (0001)	3	2
2	a	<$11\bar{2}0$>	prismatic {$10\bar{1}0$}	3	2
3	a	<$11\bar{2}0$>	pyramidal {$10\bar{1}1$}	6	4
4	c+a	<$11\bar{2}3$>	pyramidal {$11\bar{2}2$}	6	5
5	c	<0001>	prismatic {$10\bar{1}0$}	3	2
6	c	<0001>	prismatic {$10\bar{1}0$}	3	2

Primary slip in magnesium and its alloys at room temperature occurs on the basal plane {0001} in the most closely packed direction ‹$11\bar{2}0$›. Secondary slip occurs on the prismatic plane {$10\bar{1}0$} in the ‹$11\bar{2}0$› direction. At elevated temperatures, slip also occurs on the pyramidal plane {$101\bar{1}$} in the ‹$11\bar{2}0$› direction [81Yoo]. At room temperature, primary twinning occurs across the pyramidal {$10\bar{1}2$} planes in the ‹$10\bar{1}1$› direction. Secondary twinning occurs across the {$30\bar{3}4$} planes. At elevated temperatures, twinning also occurs across the {$10\bar{1}3$} planes, although it becomes

less important with respect to slip deformation. Effect of twinning to general plastic flow is that unfavourably oriented grains for slip and twinning are reoriented into a more favourable position upon twinning. Therefore, the total plastic strain can be increased considerably by the advent of second-order twinning, for example $\{10\bar{1}1\}$ twinning followed by $\{10\bar{1}2\}$ twinning in magnesium [81Yoo].

The sometimes significantly higher strains at room temperature found under compressive load cannot be explained by the action of basal slip and twinning alone, leading to the conclusion that further slip systems are activated in magnesium and its alloys even at room temperature. The activation of further slip systems is also reflected in the stress-strain curve of magnesium alloys, showing, in particular under compressive load, three stages in the strain hardening rate. The presence of dislocations in the prismatic and pyramidal planes has also been evidenced by TEM investigations [05Agn]. The activation of further slip systems is also supported by texture measurements on Mg-Li and Mg-Y alloys using neutron diffraction, showing a rotation of grains that can only be explained by the action of further slip planes [01Agn].

An explanation for the three distinct regions of strain hardening in Mg-Zn alloys is given by Blake et al [05Bla]. The stress-strain curve is divided into three stages according to its decreasing slopes:

- elastic deformation and plastic slip on the basal plane and twinning
- basal slip, twinning and prismatic slip
- basal, prismatic and pyramidal slip and twinning

The poor ductility of magnesium alloys has been attributed to highly anisotropic dislocation slip behaviour. According to reported data, the CRSS (critical resolved shear stress) of a basal slip system at room temperature is approximately 1/100 those of non-basal slip systems on prismatic and pyramidal planes, therefore, plastic deformation occur almost entirely by basal slip [03Koi].

While at room temperature the deformation mechanism of magnesium is not completely clarified, the activation of further slip systems is evident at elevated temperatures and reflected in the good high temperature ductility of magnesium and its alloys [05Agn]. The stress necessary to obtain slip (CRSS) in the prismatic plains decreases strongly with the temperature, while the CRSS for slip in the basal plain

decreases only slightly with the temperature [98Num]. Therefore, at higher temperatures, secondary slip occurs on the prismatic plane $\{10\bar{1}0\}$ in the $\langle 11\bar{2}0\rangle$ direction [06Fri].

Additionally, at elevated temperatures, slip also occurs on the pyramidal plane $\{101\bar{1}\}$ in the $\langle 11\bar{2}0\rangle$ direction and twinning also occurs across the $\{10\bar{1}3\}$ planes, although it becomes less important with respect to slip deformation.

According to former studies by Yoo [02Yoo] and Agnew [02Agn], three main types of dislocations are observed in magnesium:

- <a> dislocations, with a Burgers vector of $<11\bar{2}0>$, which may glide on basal {0001}, prismatic $\{10\bar{1}0\}$ and pyramidal $\{10\bar{1}1\}$ planes
- <c> dislocations, with Burgers vector (0001)
- <c+a> dislocations, with Burgers vector $11\bar{2}3$, which can glide on pyramidal planes $\{10\bar{1}1\}$ or $\{11\bar{2}2\}$

Deformation occurs easily along the <a> axis via glide of <a> dislocations on the (1000) basal and prismatic planes but deformation is difficult along the c axis because the motion of both <c+a> dislocation and twinning dislocation requires high stress levels [02Yoo].

2.1.2 Influence of alloying on pure magnesium

Although magnesium is commercially available with 99.8% of purity, it is rarely used pure for engineering applications. Due to its atomic diameter of 0.320 nm, magnesium forms solid solutions with a diverse range of elements that have a ±15% atomic size difference, Table 2. Small difference in valence is another factor that causes high solubility [04Agh]. Elements of practical importance like Al, Zn, Y or Ag meet both requirements of size and valence and therefore have relatively high solubility in magnesium. These elements have decreasing solubility with decreasing temperature; therefore, they allow super-saturation by a solution heat treatment or melting and precipitation upon cooling or during subsequent aging. The precipitation hardening effect is nevertheless significant only in alloys where fine coherent precipitates of GP zones are formed, like in Y, Nd and Th [04Agh].

On the other hand, experiments with binary magnesium alloys have shown that elements like Al, Zn, Ag, Ce, Cu and Th increase both strength and ductility in

tension while increasing alloying element concentration up to a maximum, Table 2. Elements like Sn, Pb, Bi and Sb strengthen but are accompanied by reduction of ductility [04Agh].

Fig. 2 summarizes a variety of binary systems of magnesium with common elements, characterized by the melting temperature of the phase in equilibrium with magnesium and its solubility. Elements preferred to be alloyed with magnesium are those which form thermally stable phases (higher eutectic temperature) and posses a higher solubility to allow precipitation hardening, although due to price and availability, some compromises are achieved when solute elements are selected [02Pet].

Table 2 : Approximate solid solution strenghthening effect of several solutes on Mg [04Agh].

Solute element in Mg	Approximate atom diameter size difference, %	Percentage increase for each wt % of solute, YS
Al	+10	25
Zn	+16	45
Ag	+9	23
Ca	-24	110
Ce	-14	148
Th	-13	212
Cu	+20	35

One of the highest solubility in magnesium is observed by scandium; however, together with Ag, Y and Sr, scandium is avoided due to its high price. Therefore, Al, Zn and RE, the late commonly used as misch metal, are most preferably found as main strengthening element in common magnesium alloys. Zinc results in a much higher strengthening rate than Al in super saturated solid solutions of Mg [02Cac, 05Bak], nevertheless, its drawback its that its eutectic melt at a lower temperature.

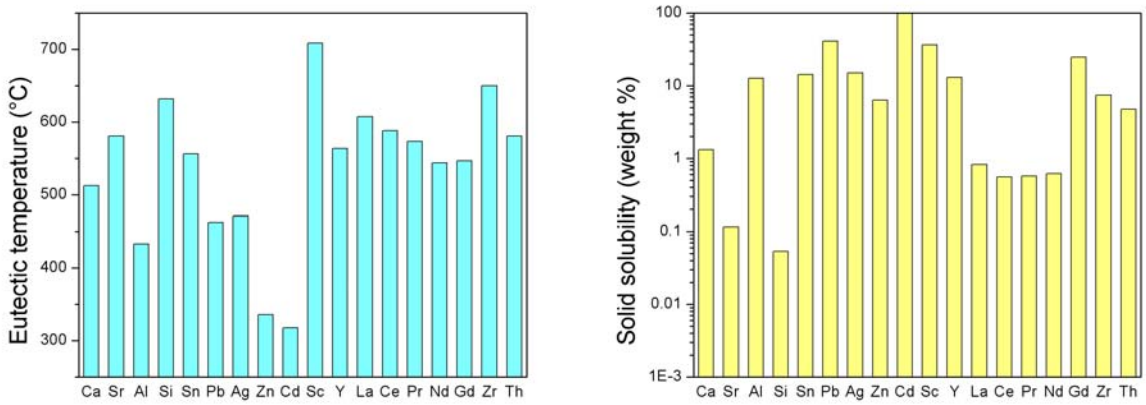

(a) Eutectic temperature (°C) (b) Solid solubility (wt. %)

Fig. 2 : Eutectic melting temperatures (left) and solid solubilities (right) of some elements in binary magnesium alloys (after [02Pet]).

2.2 Fundamentals of creep

2.2.1 Creep in metallic materials

Creep is the plastic flow under constant stress below the yield stress under the influence of temperature and a prolonged period of time. There are three types of creep associated with increasing temperature for a given stress level [95Nav]: logarithmic creep (up to about $0.3T_m$), high temperature creep, also called recovery creep, (in a temperature range about $0.6T_m$), and diffusional creep (above $0.9T_m$). For components used in automotive or aerospace applications, high temperature creep is the most important [97Hum]. This type of creep is characterized by an elongation vs. time curve, such as the one shown in Fig. 3. The creep curve can be divided into three parts: primary, secondary and tertiary creep.

Transient or primary creep, referred as stage I, is associated with the plastic deformation of the material after the initial loading. During this deformation, the material undergoes work hardening. Primary creep is often described by the phenomenological equation

$$\varepsilon = \varepsilon_0 + \beta_1 t^{1/3} \qquad \text{(Eq. 1)}$$

where ε is the creep strain, ε_0 is an extrapolated constant, approximately equal to the instantaneous strain (elastic and plastic) on loading, β_1 is a constant and t is the time [00Kas].

Secondary creep, or stage II, is characterized by a constant strain rate and may last very long time, possibly years. In this stage, a dynamic equilibrium of recovery and deformation strengthening is obtained. In the third stage there is increased elongation, which is associated with cavity growth at grain boundaries and interfaces and finally leads to failure [97Hum]. The fracture is usually related to the binding energy between grains. The grains are separated from other grains by bulky and continuous cavities, reducing the effective area of the alloy supporting the load, resulting in rapid increase of the strain rate.

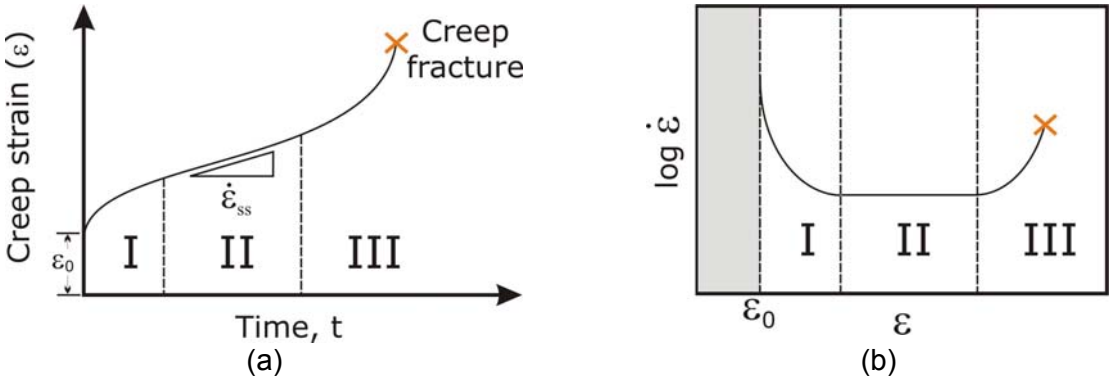

Fig. 3 : Schematical sketch of a creep curve (ε_0 is the initial strain) showing the three different stages of creep.

During creep as with all forms of plastic deformation of polycrystalline materials, the grains change their shape. However, there are two main differences between creep and a rapid tensile test. First, because of the elevated temperature, more slip systems may be operating in creep than in a tensile test at room temperature; and second, at elevated temperatures, grain boundaries become glissile and the motion of these contributes to the creep strain [95Nav].

In general, a single creep mechanism is often dominant, and this mechanism controls the creep behaviour through a limited range of stress and temperature. However, when the range of experimental conditions is wide, two or more mechanisms may operate.

Creep mechanisms in a metal or alloy can be identified by determining the activation energy and the stress exponent for creep from the Arrhenius relationship of minimum creep rate and reciprocal temperature. The minimum creep rate in steady-state (or secondary creep) is obtained from long-term creep tests. The values of activation energy and stress exponent are used to determine which thermally activated creep mechanism is predominant in a particular temperature and stress range [03Pek].

Based on applied stresses and operating temperatures, the creep deformation mechanisms for most engineering materials can be classified into two main groups: dislocation creep and diffusion creep, where the former follows a power-law behaviour, and the later exhibits a linear-viscous behaviour [03Hu]. Sometimes also three main mechanisms are categorized, adding also grain boundary sliding.

In all mechanisms operating during creep diffusion, creep rates are closely related to the Arrhenius equation of diffusion [93Eva]:

$$D = D_0 \exp\left(-\frac{\Delta Q}{RT}\right) \qquad \text{(Eq. 1)}$$

In this equation D is the diffusion rate at temperature T, Q is the activation energy for diffusion, R is the gas constant and D_0 is the diffusion rate at reference temperature. The different mechanisms of creep are described in the following, explaining their influence on the creep rate.

2.2.2 Diffusional creep

Diffusion creep becomes the rate controlling mechanism at elevated temperatures and relatively low stresses ($\sigma/G<10^{-4}$) (stress/shear modulus$<10^{-4}$) and it is governed by stress-directed atomic diffusion [03Hu]. At relatively high temperatures (T around $0.7T_m$ and above), diffusion takes place through the crystal lattice by vacancies flow from boundaries under tension to those under compression, process known as Nabarro-Herring Creep. At lower temperatures (around $0.4T_m$), when diffusion takes place by vacancy transfer along grain boundaries, the process is called Coble creep [84Hon, 93Eva, 03Hu]. Both diffusional creep processes lead to the elongation of grains in polycrystalline materials and require the operation of grain boundary sliding to maintain the grain contiguity during diffusion flow [03Hu].

Since high temperatures and low stresses are a prerequisite for this kind of creep, it is considered of little importance on the automotive applications of magnesium alloys.

2.2.3 Dislocation creep

Dislocation creep occurs at high stress levels in combination with sufficiently high temperatures. The stress level σ has to be about ($\sigma/G>10^{-4}$) (stress/shear modulus$>10^{-4}$). This type of creep consists in overcoming slip barriers by thermally

assisted activation. For yielding, dislocations have to overcome hindering obstacles (e.g., dissolved solute atoms, precipitates, and/or other dislocations) [03Hu].

The microstructure developed in creep arises from the simultaneous work hardening and recovery. Dislocation density increases with strain and dislocation networks get finer. Dislocations reduce strain energy by mutual annihilation and rearrange to form low-angle boundaries increasing the network spacing. However, sub-grains do not always form during creep and in some metallic material the steady-state substructure is a uniform distribution of dislocations. Straining then proceeds at a rate at which this refining action just balances the growth of the network by recovery [84Hon].

The most commonly described mechanism of overcoming these obstacles is dislocation climb. A theory for the climb of dislocations is described by Weertman. Dislocations in the deforming metal are constantly produced by Frank-Reed sources, which repel each other at lower temperatures. By the application of elevated temperatures, dislocations can climb and annihilate, giving way for the production of further dislocations [84Hon].

In general, the dislocation creep can be described by the power law or Norton law:

$$\dot{\varepsilon}_s = A\ \sigma^n\ \exp\left(-\frac{Q}{RT}\right) \qquad \text{(Eq. 2)}$$

where $\dot{\varepsilon}_s$ is the minimal creep rate, σ is the applied stress, n is the stress exponent, Q is the apparent energy for creep, T is the absolute temperature, R is the gas constant and A is a material constant [84Hon, 93Eva].

A change of the activation energy is observed in particular with increasing temperature, e.g. in aluminium between 100 and 200°C and in zinc between 150°C and 250°C. This change is generally attributed to the activation of cross slip at higher temperatures (generally above $0.5T_m$, where atom diffusion can occur). A model for this activation is the recovery/escape due to the thermal influence of dislocations piled up at obstacles, such as Lomer-Cottrell sessile dislocations or at incipient cell walls [84Hon].

2.2.4 Grain boundary sliding

Grain boundary sliding occurs when two adjacent grains in a polycrystalline matrix are displaced with respect to each other. Sliding occurs when extrinsic dislocations

move along the grain boundaries to give a relative displacement of adjacent grains. However, unlike intragranular dislocations processes such as slip where the grains change shape as a result of the deformation, grain boundary sliding leads to no change in grain shape so that an additional accommodation process is needed, in the form of some limited slip within the grains, in order to maintain coherency at the boundaries [96Lan]. In case the accommodations is not possible, grain boundary sliding can lead to the development of internal cavities and ultimately to the failure of the material.

The wavy grain boundaries, which are frequently observed during high temperature creep, are a result of inhomogeneous grain boundary deformation and grain boundary migration [88Die]. Grain boundaries are not perfectly straight and after a small amount of sliding at the boundary interface, movement is arrested by protuberances. As a result, the rate of slip along a grain boundary is not constant with time, because the dislocations form first into piled-up groups, and these become later relaxed. Local relaxation is a process in which the dislocations in the pile-up climb towards the boundary. In consequence, the activation energy for grain boundary slip may be identified with that for steady-state creep [99Sma].

2.3 Creep in pure magnesium

A review of creep mechanisms in polycrystalline pure magnesium has been performed by Vagarali et al. [81Vag]. The main mechanisms at different conditions observed as well as the activation energy and the stress exponent are given in Table 3 after his work.

Tegart et al. find an activation energy in pure polycrystalline magnesium of about 117 kJ / mol and a stress exponent of about 5.5 between 177°C and 277°C, and a significant increase of the activation energy at higher temperatures. At very high temperatures, e.g. after creep at 450°C, metallographic observations indicated non-basal slip [61Teg].

In accordance to the investigation of Tegart, Vagarali et al. [81Vag] found dislocation slip on basal planes, Fig. 4 (a) and an activation energy of 135 kJ / mol between 200-327°C and stresses of about 2.5 MPa to about 30 MPa. Above 327°C-477°C the activation energy was increased and found to be a function of the stress, amounting to about 170 - 220 kJ / mol at stresses of 2.5-10 MPa. This increase in activation

energy at higher temperatures is interpreted as non-basal slip, evidenced by wavy slip traces appearing on the surface after creep, Fig. 4 (b). At high temperatures and stress below about 2.5 MPa the stress exponent is close to 1 and an activation of about 139 kJ / mol indicate diffusion creep.

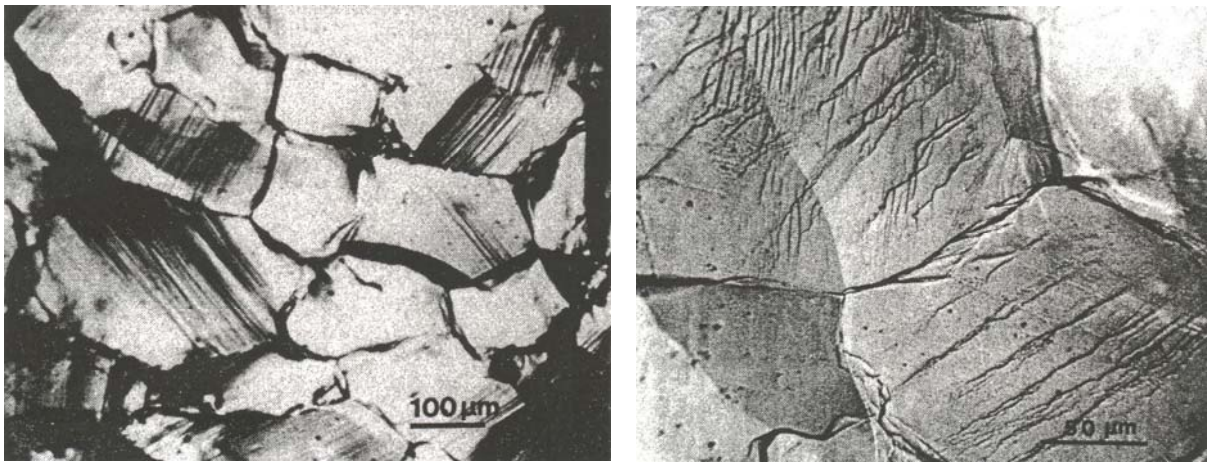

(a) evidence for basal slip (b) evidence of non-basal slip

Fig. 4 : Photomicrograph of a magnesium specimen tested to (a) a strain of 12% at 250°C and 17 MPa and (b) a strain of 10% at 500°C and 8 MPa. Micrographs taken from [81Vag].

Accordingly, Crossland and Jones found an abrupt change of activation energy and stress exponent at about 350°C polycrystalline magnesium. At low temperatures the activation energy of about 92 kJ / mol and a stress exponent of 5 was determined, while at higher temperatures the activation energy was 230 kJ / mol and the stress exponent amounted to 10 [72Cro].

A similar transition of slip on the basal plane to cross slip from basal to the prismatic plane is also observed to occur with increasing strain rate. Jones et al. found an increase of activation energy from about 105 kJ / mol and a stress exponent of 4.5 to about 360 kJ / mol and a stress exponent of 8, if the strain rate is increased above about 10^{-6} s^{-1} [63Jon].

Milička et al. [70Mil] found a similar change of the activation energy at a certain stress level. In powder metallurgically produced Mg with dispersed MgO particles an hyperbolic decrease of the activation energy was found up to about 40 MPa. At 40 MPa a drop of the activation energy from about 160 to 115 was observed. The mechanism at low stresses was interpreted as non-basal cross slip or as the nucleation of kink motion on the pyramidal slip system. At higher stresses, the non-

conservative motion of jogs on screw dislocation gliding on the basal planes is assumed as the active mechanism.

Table 3 : Creep of polycrystalline magnesium, summarized from [81Vag].

Condition	T (°C)	Q (kJ/mol)	n	Rate-controlling mechanism	Ref.
Polycrystalline Mg	177-277 > 277	~ 117 ~ 218	~ 5.5 ~ 4	Dislocation climb Cross slip from basal to prismatic planes	[61Teg]
Strain rates: $< 10^{-6}$ s^{-1} $> 10^{-6}$ s^{-1}	197-427	~ 105 up to ~360	~ 4.5 up to ~ 8	Transition from dislocation climb at low strain rates to cross-slip from basal to prismatic planes at high strain rates	[63Jon]
$\sigma < 40$ MPa Powder metallurgy $\sigma > 40$ MPa	127-527	160-220 90-115	~8	Non-basal cross slip or nucleation of kink motion on the pyramidal slip system Non -conservative motion of jogs on screw dislocation gliding on the basal planes	[70Mil]
Polycrystalline Mg	< 350 > 350	~ 92 ~ 230	~ 5 ~10	Dislocation pipe diffusion Non-basal cross slip	[72Cro]
$\sigma < 2.8$ MPa (Pure Mg) $\sigma < 1.4$ MPa	270 425			Coble grain boundary diffusion creep Nabarro-Herring lattice diffusion creep	[65Jon]
Pure Mg	150-325	~ 105		Coble grain boundary diffusion creep	[77Cro]
up to 30 MPa	200-327	~ 135	~ 5.2	Basal slip, creep controlled by dislocation climb	[81Vag]
$\sigma > 2.5$ MPa	327-477	$f(\sigma)$	~ 6	Non-basal slip, cross slip from basal to prismatic planes	
$\sigma < 2.5$ MPa	477-547	~ 139	~ 1	Lattice diffusion creep	

2.4 Creep resistance and strengthening in magnesium alloys

As described in the previous chapter, dislocation creep - as the relevant mechanism in magnesium applications - originates from the dislocation movement within grains

and from grain boundary sliding. Strain hardening decreases creep, but it is again counteracted by recovery during the secondary stage. Nevertheless, some magnesium applications stay in the primary stage, like in the case of bolted conections. Loss of bolt clamp-up load may influence the strength of the connection. Alloying elements in solid solution usually slow down the process of recovery. Additionally, solute atoms increase the creep strength by hindering the dislocation slide. Furthermore, segregation of solute atoms to dislocations can cause locking of dislocations. Segregation to grain boundaries can hinder grain boundary migration and sliding, if they are stable at high temperature [03Hu]. On the other hand, solute atoms diffuse easily at higher temperatures accompanying the movement of dislocations. This is the reason why alloys above $0.5T_m$ are not benefited from the strengthening mechanism of solid solution.

Precipitates can therefore more efficiently increase the creep resistance. In addition to precipitates existing before the thermal and mechanical load, efficient precipitates can also arise during creep at elevated temperatures. The precipitation process can lead to a large reduction in the secondary creep rate of an alloy. Newly formed precipitates nucleate frequently on dislocations responsible for creep strain and hinder the movement of these dislocations. The most effective precipitates are those that coarsen slowly, providing a very fine dispersion that resist the dislocation movement [03Hu].

2.4.1 Magnesium - calcium alloys

Calcium leads to precipitation hardening due to the formation of the stable intermetallic phase Mg_2Ca after ageing treatment [97Nie]. The optimum amount of Ca addition is below 5% in order to attain high strength combined with some ductility [94Miy].

Calcium is also used as a grain refiner [06Fin]. Combined addition of Ca and Zr is effective for ignition prevention of magnesium alloys during melting and casting [98Cha].

2.4.2 Magnesium - zinc alloys

Zinc enhances strength of magnesium by solid solution strengthening and precipitation hardening, increasing its tensile properties. It is regarded as a far more efficient strengthener of Mg than Al at high solute concentrations, using up to 6.9 wt.

% [02Cac]. Boehlert et al. [05Boe] investigated the influence of Zn content on the strength of as cast alloys, finding an optimum strength at 4.1 wt. % in tensile and creep properties.

The microstructure and strengthening mechanisms of the hardened alloy has been investigated in various works. During aging of binary Mg–Zn alloys, Guinier-Preston (GP) zones and metastable MgZn, $MgZn_2$, Mg_2Zn_3 precipitates are observed. Wei et al. consider the rodlike β'_1 precipitates on the basal plane during age hardening as the main strengthening phases, while the onset of overaging is caused by formation of disk-shaped β'_2 precipitates [05Wei]. The β'_1 precipitates are believed to act as strong pinning points hindering (0001) glide of dislocations, whereas β'_2 provide much less of an obstruction to the movement of these dislocations [05Wei]. They find the presence of rare earth additions retarding the formation of β'_2 precipitates and thus postpone overaging [05Wei].

Mg–Zn–Zr alloys (known as ZK alloys) are used commercially due to their relatively high strength, good plasticity and also good corrosion resistance [95Pol]. However, for casting, the amount of Zn is limited because of a high susceptibility to hot cracking during solidification, resulting from the large temperature range of solidification and the corresponding high shrinkage of the melt.

In order to improve castability, rare earth elements were considered as further alloying elements because, contrary to Zn, these elements form eutectic systems with a small temperature range of solidification. Zn forms intermetallic phases with the RE elements and/or Mg as plates on basal planes of α-Mg matrix [97Nie].

A drawback of magnesium-zinc alloys is their insusceptibility to grain refining by superheating or inoculation [02Lee]; additionally, the grain refinement by zirconium is problematic [66Eml]. It has been reported that in magnesium alloys containing both zinc and zirconium there is a tendency for the formation of an intermetallic compound between these two elements during prolonged heat treatment at elevated temperatures [04Bet, 66Eml]. Li et al. found Zn_2Zr_3 in the grain boundaries of a Mg–5Zn–0.6Zr alloy [07Li]. Therefore, the Zn content in solid solution available to participate in the formation of Zr-Zn is reduced.

A significant improvement in castability and grain refinement can also be achieved by the addition of calcium, as realized in the Mg-Ca-Zn alloys.

2.4.3 Magnesium - calcium - zinc alloys

The magnesium rich part of the ternary phase diagram of the Mg-Ca-Zn system has been extensively studied and reported in the past by different authors [00Lys]. Recently, the magnesium rich corner was also calculated by [04Zil] for 465°C, showing a maximum solubility of 4wt% of Zn and 1wt% of calcium in magnesium. The main equilibrium phases in the magnesium rich corner are Mg, Mg_2Ca, $Ca_2Mg_6Zn_3$ (τ1-phase), as well as the binary Mg_XZn_Y phases.

Several investigations show that the ternary phase $Ca_2Mg_6Zn_3$ (τ1-phase) is preferably found, while the formation of Mg_2Ca is often not evidenced even if thermodynamically expected [97Nie, 00Hor, 01Lar, 02Bam, 02Fin, 04Jar, 04Zil, 06Bam, 09Zho]. The appearance of the Mg_2Ca is found only in alloys with high amount of Ca [01Lar] and if the alloy is not too quickly solidified as in [09Zho].

Other studies report on the precipitation behaviour and hardness of this system. For low levels of alloying, Nie et al. has found precipitation hardening in Mg1Ca1Zn alloy, showing a hardness of 63HV after optimized aging. The hardening is mainly attributed to the τ1-phase $Ca_2Mg_6Zn_3$ [97Nie]. This is also concluded by Bamberger et al, who investigated the hardness and the precipitation behaviour in four different Mg-Ca-Zn alloys. The alloy with the maximum amount of Ca and Zn, Mg1.2Ca1.2Zn showed hardness after aging of about 70 HV [02Bam, 06Bam].

Significantly higher hardening can be achieved by higher levels of hardening elements. Rapidly solidified Mg6Zn5Ca3Ce has a high hardness of 162 HV in the T6 state as found by Zhou et al. [09Zho]. As well as at lower levels of Ca and Zn the hardening is attributed mainly to the homogeneous distribution of the τ1-phase $Ca_2Mg_6Zn_3$.

The stability of the as cast microstructure was investigated by Finkel et al. on Mg5Ca6Zn alloy, showing slight diffusion of elements from the grain interior to the grain boundaries after 40 days of exposure to 160°C. However, no significant decrease of hardness was observed in this alloy [02Fin, 03Fin]. Similar observations were made by Zilberov et al. on the as cast microstructure of Mg1.6Ca3.2Zn after 32 days, observing coarsening of the grain boundaries, but no significantly decrease of hardness up to 200°C, while hardness decreases at 225°C [04Zil, 06Lev]. Zilberov et al. also calculated the phase fractions for the before mentioned compositions at

several temperatures, showing that the τ1-phase is stable only up to about 350°C [04Zil, 06Lev].

Only little literature is available on creep properties of the Mg-Ca-Zn system. Horie et al. have characterized the creep resistance of Mg2wt%Zn1wt%Ca in comparison to Mg2wt%Zn and Mg1wt%Zn. The alloy containing both zinc and calcium showed highly improved creep resistance as compared to the binary alloys, amounting to less than 0.1% creep after 300 h at 150°C up to about 100MPa [00Hor].

The creep resistance of Mg1Ca1Zn0.6Zr gravity cast alloy in the T6 condition was investigated by Gao et al. [05Gao] and showed good creep resistance up to about 150°C. Creep strain smaller than 0.1% after 100 h up to 90 MPa was achieved at this temperature. Additionally, a further improvement of tensile and creep strength was achieved at both room temperature and 150°C by the addition of 1% of Nd to the system. The improved mechanical properties are attributed to precipitation hardening. The stress exponent was 6.2, close to what is found for AZ91 (6.3). Peak aged microstructures contained a uniform, dense distribution of discs on the basal plane of the α-Mg matrix. However, a clear conclusion on the rate determining mechanism and the precipitation behaviour could not be drawn.

2.4.4 Magnesium - rare earths alloys

The solubility of the rare earths metals in solid magnesium has been systematically determined by the experimental work of Rohklin [03Rok pp. 72] and has confirmed the classification of the rare earths metals, already given elsewhere [03Gup], into two subgroups: the cerium subgroup, whose elements (La, Ce, Pr, Nd, Pm, Sm and Eu) show low solubility in magnesium, and the yttrium subgroup, whose elements (Gd, Tb, Dy, Ho, Er, Tm, Yb, Lu, Y and Sc) show greater solubility in magnesium. An increase in solubility was observed for both groups according with the increasing atomic number, excepting for Eu and Yb.

The most interesting feature concerning the alloying of magnesium with rare earth metals is that the yttrium subgroup enables solid solution hardening and precipitation (age) hardening, while the cerium subgroup allows only precipitation hardening [02Mor, 95Pol].

Improvement in strength of Mg-RE alloys increases with the solid solubility of the alloying elements in magnesium, which increases in the order La-Ce-Pr-Nd [89Uns],

and thus strengthening is weaker than in Mg-Y. The strength is increased with the amount of alloying element but decreases again at higher concentrations, which also leads to strong embrittlement at room temperature [89Uns]. In order to increase ductility in these alloys a variety of grain refining methods has been proposed, in particular zirconium, proved to be effective for this purpose.

Yan et al. [08Yan] found that an increasing neodymium content increases the creep resistance in binary alloys of Mg-x% Nd on the range of temperatures of 150-225°C and stress levels of 50 MPa to 90 MPa. This increase is attributed to a combination of precipitation and solid solution hardening. The activation energy of 152 kJ / mol and the stress exponent of 4.5 for the Mg–2 wt% Nd alloy suggests dislocation climb as creep mechanism.

Weiss et. al. [02Wei] found in their work with the Mg-1.7RE-0.3Mn alloy an activation energy of 240-250 kJ/mol at temperatures of 190°C-210°C and stresses of 50 MPa to 60 MPa, indicating that at these temperatures the creep mechanism involved cross slip of dislocation from basal to prismatic planes.

Creep behaviour is significantly dependent on the aging treatment, showing minimum creep at an aging temperature of 200°C, resulting in submicroscopic precipitations within the grain, while microscopically visible precipitations at higher temperature generated a drop in creep resistance [89Uns].

The precipitation processes in Mg-RE systems are not completely understood. In the Mg-Nd system, four stages of precipitation have been detected. It involves the formation of G.P. zones, β'', β'and β phases [03Pin]. Most hardening is associated with the formation of the coherent β´´ phase. Loss of coherency of this phase occurs close to 250°C and is associated with a marked increase in creep rate. The β´ phase is nucleated on dislocation lines when the alloys are in the temperature range 200-300°C [03Pin]. Precipitation process in binary Mg-Ce or Mg-MM alloys is similar to the sequence observed in Mg-Nd alloys, with some controversies [03Pin]. It is possible that Mg-RE (Ce) alloys have a similar ageing sequence, which leads to the formation of an equilibrium precipitate that is either $Mg_{12}Ce$ or $Mg_{41}Ce_5$.

Another positive contribution to creep resistance is also attributed to isolated particles of eutectic, which are left behind in the grain boundaries after solution heat treatment [85 Uns, 04Smo]. In Ce containing alloys, the grain boundary eutectic persists during

heat treatment up to the eutectic temperature due to the low solubility of Ce in magnesium [04Smo].

2.4.4.1 Magnesium - rare earths (cerium subgroup) - zinc alloys

The good creep resistance of magnesium-rare earth alloys can be enhanced by the combination of RE elements with Zn. An alloy outperforming AE42 in terms of creep resistance is Mg-2.5RE-0.35Zn-0.3Mn (MEZ – Magnesium - Rare Earths - Zinc), developed by Magnesium Elektron and presented in 1997. Moreno et al. characterized the creep of the alloy in the as die cast condition at 150 and 175°C and stress levels of 50-100 MPa, showing significantly decreased creep rates at 150°C and 175°C with respect to AE42 [03Mor]. The stress exponent was similar to AE42 (in the range of 6-7) for low stresses, indicating that dislocation climb is the rate determining mechanism. At higher stress levels, transition of the stress exponent to 37-44 was observed, which is attributed to onset of mechanical damage (power law breakdown). In contrary to AE42, no change of the grain boundaries was observed after creep, indicating higher thermal stability of the alloy.

Bettles et al. found in sand cast MEZ with a relatively high grain size of about 290 µm an activation energy of 147 kJ / mol at 150 and 177°C and a stress range of 35-46 MPa [00Bet].

The role of zinc within Mg-RE systems with respect to strengthening and its influence on creep has been subject to several investigations. Gill et al. [04Gil] investigated the precipitation behaviour of Mg-Nd-Gd-Zn-Zr with varying Zn and Gd content during aging at 200°C. It was shown that Zn and Gd enhance the aging response. Also Nie et al. found an enhancement of peak hardness only at Zn levels of 1% and above in Mg-6Gd-0.6 Zr alloys [05Nie]. On the other hand, the addition of 0.5% Zn to Mg-3%Nd resulted in an increase of peak hardness during aging of the alloy, while the addition of 1.35% showed less peak hardening.

Additional information on the mechanism of Zn in Mg-RE alloys is given by microstructural investigations. Micro alloying addition of Zn causes a significant change in the precipitation sequence and constituent phases of both Nd and Ce [03Pek]. For the MEZ alloy, it has been proposed to involve formation of G.P. zones, γ'' (metastable phase with hexagonal microstructure, precipitates as plates on the basal plane of α-Mg) and γ (equilibrium phase with fcc structure, form rods).

The beneficial effect of micro alloying of Zn on age hardening response was explained for Mg–RE and Mg–Ca alloys by the formation of very thin plate-like precipitates on the basal planes of Mg. These very thin precipitates are believed to be caused by the large strain fields produced by the oversized atoms with respect to Mg. To reduce the strain field, Zn probably segregates on the same basal plane, resulting in internally ordered Guinier–Preston zones [97Nie, 03Pin, 03Wil, 05Nie].

Even some further improvement of creep resistance was reported by slightly different alloy compositions. Villa Fanjul et al. have replaced the mischmetal of MEZ by pure Nd, resulting in a comparable creep rate to A380 at 200°C [03Vil]. Also Bell et al. have reported to reduce the creep rates by a factor of 24 at temperatures above 240°C as compared to the alloy proposed by Fanjul et al. [04Bel]. This was achieved by increasing slightly the Nd and Zn level, by replacing of Mn by Zr and by adding 0.3%Gd.

A similar alloy with the composition Mg-1.2Gd-2.7Nd-0.5Zr-0.4Zn was commercialized as Elektron 21 for application in aerospace and specialty in the T6 temper [07Kie, 07Kie02]. Kielbus found stacking faults in the alloy, indicating that similar mechanisms operate as with Zn in Mg-Y systems.

The effect of further alloying elements on the Mg-RE was already investigated some decades ago. Mellor and Ridley reported on the effect of Al, Li, Zr, Mn, Si, Ag, Cd on the creep resistance of Mg-Ce and Mg-MM alloys, finding only Zr, Si, and Mn to reduce creep at 15 MPa and 250°C [53Mel].

2.4.4.2 Magnesium - rare earths (yttrium subgroup) - zinc alloys

The highest performance of magnesium alloys in terms of creep at elevated temperatures and commercially available are the Mg-Y alloys. The yttrium is an effective precipitation hardener and solid solution hardener, much more effective than aluminium or manganese [04Smo]. However, a high content of Y is needed to obtain sufficient strength, which also increases alloy cost. This leads to partial substitution of Y by further RE elements.

Mg-Y-RE (Nd) alloys, such as 5.1% Y–1.75% Nd–1.5% RE–0.5% Zr and 4% Y–2.25% Nd–1% RE–0.5% Zr [05Zal] were introduced commercially: The alloys WE54 and especially WE43 are used in aeronautical application up to 250°C [07Smo] and maintain useful properties at temperatures as high as 300°C [00Kin]. The yield

strength at room temperature of WE is given by King et al. of 205 MPa, while the maximum stress for 0.2% total strain after 100 h at 200°C also amounts to 167 MPa. However, these good mechanical properties are achieved only in the T6 treatment (solid solution heat treatment, forced-air quenching and artificial aging) [89Uns], increasing the costs of the material significantly. The high cost of these alloys is accepted only in higher performance applications (like aerospace, F1 engine and gearbox, helicopter transmission).

The mechanisms of creep in these alloys have been subject to many investigations. In these alloy precipitates β'', β', and β of high thermal stability are formed during aging. Like most of the rare earth elements, these precipitations are believed to lie parallel to the first and second order prismatic planes [05Zal].

Accordingly, Smola states that creep is mainly reduced by precipitation of thin plates on the prismatic planes, which are least effective on the basal plain, but constitute strong obstacles to cross slip of basal dislocations and to non basal slip [04Smo]. The experimental alloy Mg-3Y-2Nd-1Zn-1Mn showed also a stress exponent of 5.9 at 300°C and 30 – 80 MPa stress range. Creep is controlled by cross slip or the climb of basal dislocations and non-basal slip.

Wang et al. found in WE43 in T6 condition a transition of creep mechanism at about 200°C. At lower temperatures and higher stresses an activation energy of 118.7 kJ / mol and a stress exponent of about 10 was found [01Wan]. The comparison with further literature data on Mg-Y alloys suggest that the stress exponent for lower stresses up to about 200 MPa is 4-5 corresponding to dislocation climb. Above 200°C the activation energy of 232.9 kJ / mol is interpreted as dynamic coarsening of precipitates [01Wan] but also corresponds to the activation energy observed in binary alloys of Mg-Y at higher temperatures and can correspond to the activation of non basal slip or cross slip to the prismatic plane.

The creep at high temperatures of binary Mg-xY alloys was investigated by [01Suz]. The creep behaviour with x=0.1, 1.2 and 2.4 mol% between 277°C and 377°C was characterized. The stress exponent was found to be 5-6 and the activation energy was 230 to 290 kJ / mol, comparable to the creep in WE found by Wang et al [01Wan]. This high activation energy correlates to the activation of non basal slip and it’s found in many hcp alloys at such high temperatures [03Suz].

Mordike [02Mor] has summarized several investigations, which have determined the active mechanism of creep in Mg-Y alloys, finding that the activation energy decreases with increasing Y content. For a particular alloy, Mg5.9Y3Nd the activation energy of 60-68 kJ / mol was determined for temperatures below 300°C, suggesting dislocation climb with vacancy diffusion, being the active mechanism. At higher temperatures, an activation energy of 100-226 kJ/mol was determined, which was interpreted by the author as dislocation climb.

Other factors affecting the creep resistance in Mg-Y-RE alloys are proposed. It is discussed that creep is reduced by the decrease of stacking fault energy resulting from the Mg-RE solid solution [04Smo]. Moreover, the occurrence of jerky flow in tensile sample at elevated temperatures shows that, for some strain rates, solute drag may make a contribution to the creep resistance [02Mor].

Further developments, aiming at increased strength in the alloy have been reported, but did not result in higher creep resistance. Neubert has replaced Nb by Tb in the WE43 alloy. However, this resulted in slightly decreased minimum creep rates and the corrosion resistance was even lower than in WE43 alloy [07Neu].

The effect of Zn in Mg-Y alloys has been studied extensively, aiming at increasing the creep resistance in die cast alloys [89Uns]. Zn reduces the solubility of Y in Mg and thus precipitation hardening is achieved at lower amounts of Y [02Mor]. The strengthening effect of small additions of Zn (0.02 mol %) is considered important to dilute Mg-Y alloys [00Suz, 02Mar, 04Suz].

Suzuki et al. [00Suz] show an improvement of minimum creep rate comparing Mg-1mol%Y binary alloy with ternary Mg-1mol%Y-x%Zn with x=0.02 and 0.04 at 277-377°C and stress levels of 10 and 50 MPa. The stress exponent is not significantly changed, being in the order of 5-6. Microscopical investigations have shown increasing planar defects on the basal plane with increasing Zn content. It is concluded, that Zn suppresses the non basal slip that operates at such high temperature due to deformation of these planar defects on the basal plane. Therefore, the reduction of creep by Zn is attributed to the decreased stacking fault energy. Segregation of Zn and Y at the stacking faults is observed, which can lead to strong interaction with dislocations [04Suz]. Also, splitting of basal dislocations into partials has been observed in Mg-0.9 at.%Y-0.04 at.%Zn [03Suz]. Correspondingly, Smola states that the addition of Zn to Mg-3Y-2Nd-1.45Mn alloy lowers the stacking

fault energy and leads to the formation of thin plates on the basal plane, stable up to 300°C, resulting in decreased creep [07Smo]. The alloy Mg4Y1Zn1Mn presented partial dislocations and a fringe contrast of stacking faults, in contrast with the Mg4Y1Sc1Mn. The creep rate of the latter alloy is significantly larger than the former one.

An increase of creep resistance by the addition of Zn was also found in experimental quaternary alloys in Mg-Y-Zn-Zr system. An optimum amount is found at about 2% Zn, resulting in better steady state creep rates than for the Mg-Y-Zr alloys without zinc. The best creep resistance in Mg-Y-Zr alloys was obtained with 2% Zn and 2% Nd addition in the as-cast condition [02Mor]. However, a low stability in Mg-Y-Zn alloys was found above temperatures of 250°C in investigations of Mordike et al., which attributed the low stability to the formation of MgYZn precipitates, which are unstable at higher temperatures [02Mor].

2.5 Casting of magnesium alloys

2.5.1 Conventional casting methods

Besides the gravity casting methods, such as permanent mould casting, sand casting, and investment casting, high pressure die casting method (HPDC) has been successfully applied in magnesium alloys [99Ave]. Most magnesium alloys components are produced by HPDC [95Pol]. Pressure die casting is a process where molten metal is injected through a narrow gate into a permanent metal mould under high pressure. The advantages of HPDC are high productivity and the possibility of producing thin-walled and near-neat shape components. The high cooling rates on the mould lead to fine grained microstructure, with good mechanical properties [03Sie].

Pressure die casting can be divided into hot chamber technique, where the casting case has an integrated casting chamber that always stay within the melt, Fig. 5 (a), and cold chamber technique, where the metal is molten in an external furnace and filled into the casting unit, Fig. 5 (b) [03Sie]. Due to the high velocities developed during injection and the resulting turbulent flow of the melt, pressure die cast materials still exhibit a certain amount of porosity.

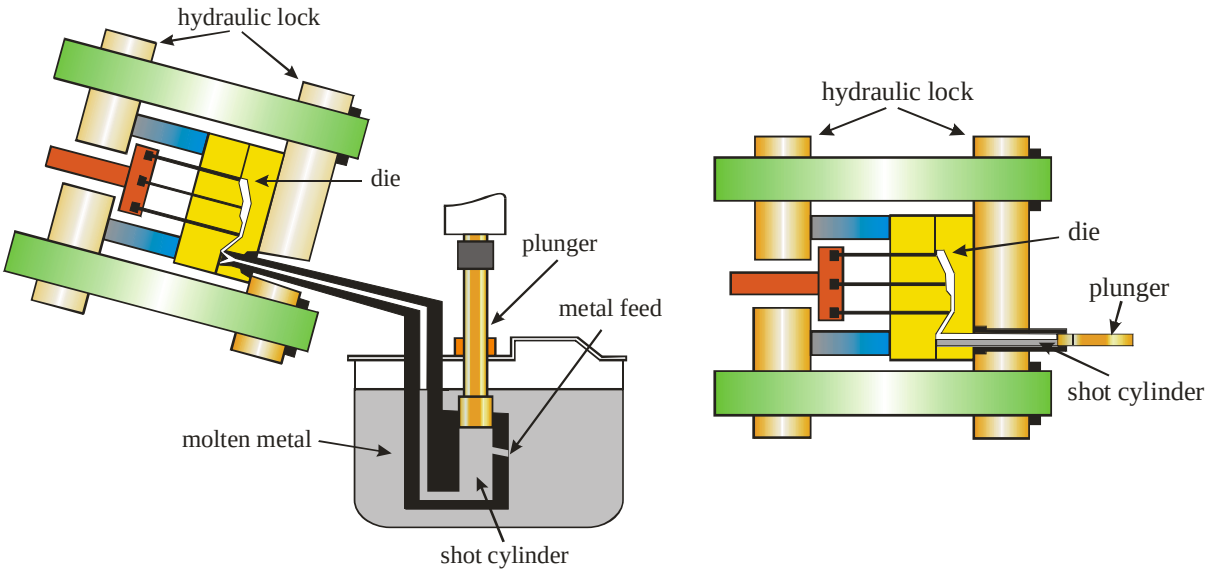

(a) Hot chamber die casting (b) Cold chamber die casting

Fig. 5 : Schematic view of the high pressure die casting process, after [03Sie].

Squeeze casting is a special process aiming at the suppression of pores by lowering the casting speed while maintaining a high pressure of compression after injection of the melt as in pressure die casting, Fig. 6. This is realized by vertical injection of the melt into the die [95Pol]. One of the most important advantages of this process is that alloys which are difficult to cast can be processed by squeeze casting, like creep resistant alloys or thixotropic melts [03Kai].

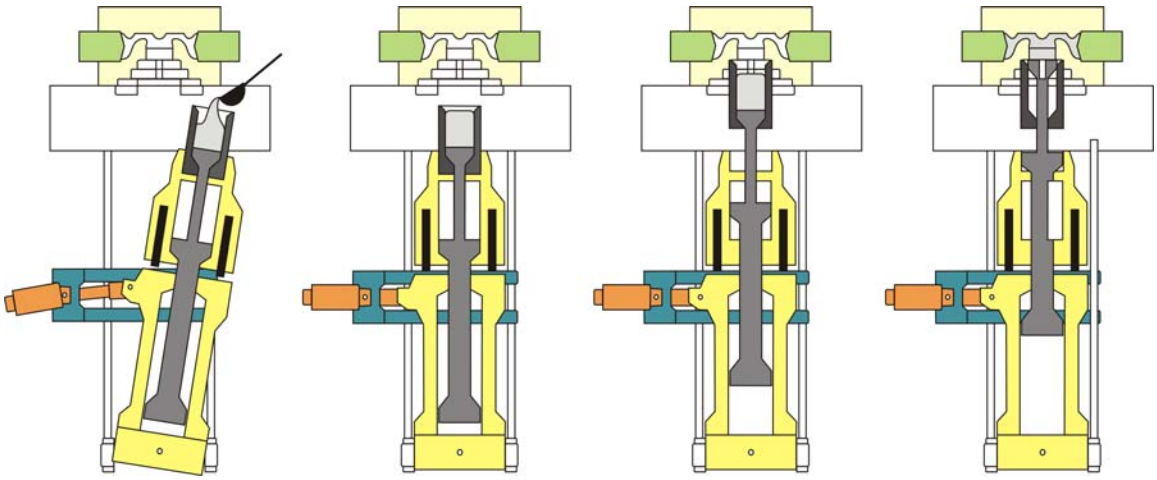

Fig. 6 : Schematic view of a vertical squeeze casting machine (after [03Kai]) showing the four steps of casting: 1. filling of metal, 2. rotation into position, 3. moving lower casting cylinder to the mould, 4. injection of metal into the mould.

2.5.2 Semi-solid processing

Semi-solid processing is based on the observation by Spencer et al. in the early 1970s that a partially melted metal or alloy, i.e. at temperature between liquidus and

solidus, has very low viscosity when subjected to sufficient shear forces [72Spe]. Even at volume fractions of solid as high as 0.60 sufficient low viscosity could be reached for casting [76Fle], thus lowering the casting temperature and the associated shrinkage [93Bro]. Additionally, the attack of the tooling is decreased by the reduced temperature, and turbulences are minimized by the lower viscosity of the semi-solid mass in comparison to pure melt, providing laminar flow with a stable flow front, which in turn reduces porosity and entrained oxides [03Jor]. Semi-Solid Processing is competitive when the parts have an intricate design, often combining thin and thick sections, reducing or even eliminating machining and having the need for a high integrity, e.g. for mechanical or pressure tightness purposes [00Gar].

The decreasing viscosity with increasing shearing is in part attributed to the transformation of dendrite structure to a globular shape structure of the solid particles within the melt. The mechanism of this transformation is not yet fully clarified. Several mechanisms, as breaking of dendrite branches, re-solution, etc. are proposed and e.g. discussed in detail by Flemings [91Fle]. In addition to this irreversible transformation, a second, reversible mechanism is assumed: The agglomeration of solid particles within the liquid upon resting of the semi-solid is responsible for an increase of the viscosity, while breaking up of these agglomerates during shearing leads to the decrease of viscosity [02Che, 02Fan, 02Fan2, 02Fan3]. This thixotropic behaviour has given the name for several different processes based on semi-solid processing.

The casting processes developed and commercialized to take advantage of the behaviour of semisolid slurries can be mainly divided into two different basic routes [05Cze]:

- The rheo-route
- The thixo-route

In the rheo-route the material is completely melted and subsequently partially solidified before its injection into the mould whereas in the thixo-route the solid material is reheated to semisolid temperatures and injected into the mould [05Cze].

In the Rheo Diecasting (RDC) process the feedstock material is completely melted, solidified during stirring and subsequently injected into the mould. The RDC equipment consists of two units: a twin-screw device to produce the thixotropic mass through solidification under high shear rate and high turbulence, and a standard cold

chamber HPDC machine used to achieve the final component shape [05Fan]. The process is schematically illustrated in Fig. 7.

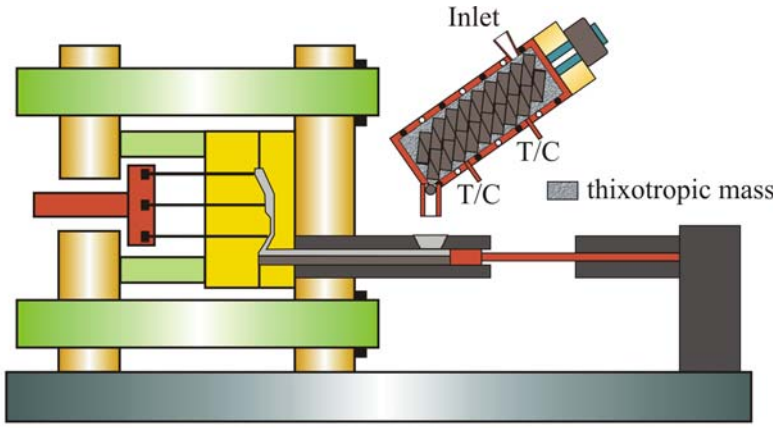

Fig. 7 : Twin screw rheo diecasting process as depicted by [05Fan].

The New Rheocasting (NRC) process was recently designed to provide a cost-effective casting process for high quality castings, also starting from a liquid melt [01Kau, 03Kau]. The process chain is schematically depicted in Fig. 8. In contrast to the rheocasting the melt is not stirred mechanically, but cooled relatively fast in order to obtain a high number of nucleation sites. Under controlled cooling, the homogeneously distributed nuclei lead to the growth of globular grains, forming a skeleton of solid primary phase. Subsequently, the slug is placed into the sleeve of a squeeze casting machine and cast to shape [03Kau].

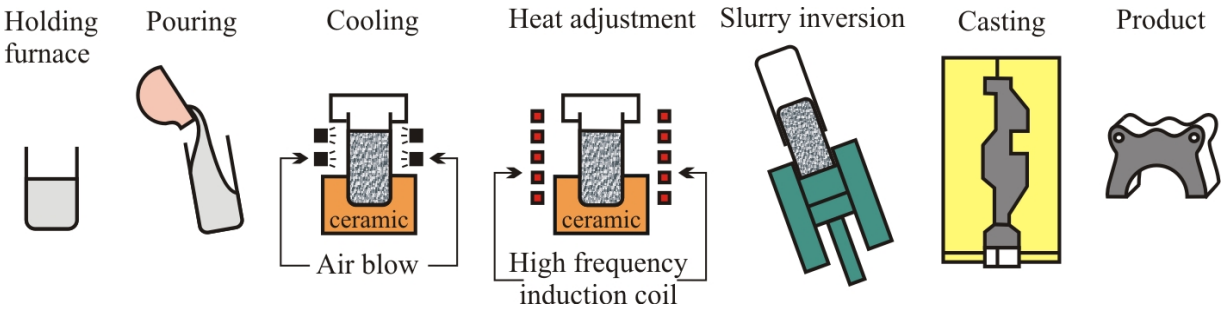

Fig. 8 : Schematical depiction of the new rheocasting process chain [03Kau].

Another new process starting with completely melted material is the Sub-Liquidus Casting (SLC) Process [03Jor]. Here, a strongly grain refined liquid metal is cooled slightly below the liquidus temperature in order to achieve a globular grain growth. Subsequently, the melt is filled into a vertical shot sleeve, where it is cooled to a temperature corresponding to about 0.4 to 0.6 solid fraction. However, this process is efficient only for alloys including a strong grain refiner. Additionally, the control of the

cooling is difficult and less homogeneous than in the previously described methods. This problem is solved, in part, by a gate plate at the entrance to the shot sleeve, which allows only material to flow into the shot sleeve, having the appropriate temperature and microstructure [03Jor].

The thixomolding process is a foundry-free process also known as semisolid metal injection moulding [00Wal]. In this process, the feed is not liquid, nor a solid billet, but rather metallic pellets that are fed into a heated barrel in which a rotating screw advances and shears the alloy to produce a thixotropic slurry, which is subsequently injected into the die cavity [03Jor, 00Wal]. A typical machine is depicted in Fig. 9:

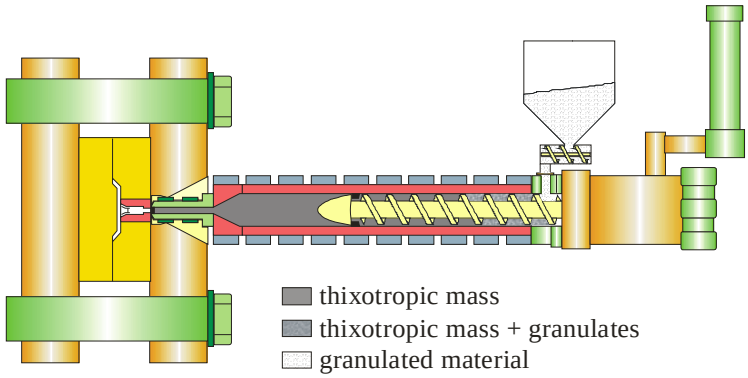

Fig. 9 : Thixomoulding process before injection of the slurry [03Jor].

Thixocasting is the generalized name used for the thixo-route if the process is performed in a closed die, Fig. 10. If the mould is open during the operation, it is called thixoforging [05Cze]. Thixocasting is considered a two steps process because the feedstock material needs to be prepared with thixotropic characteristics before its casting [04Kle]. Upon reheating, the microstructure of the billet is transformed into suitable semisolid slurry, with a defined volume of fine and globular solid particles uniformly distributed in the liquid matrix.

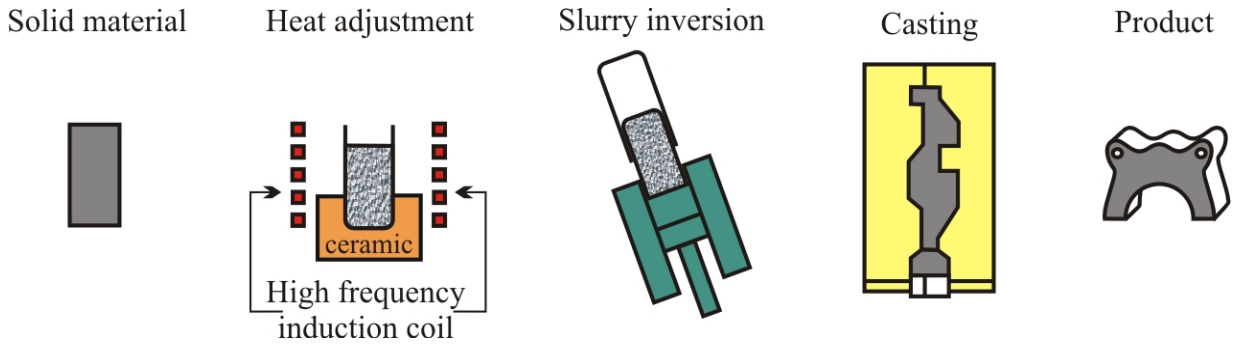

Fig. 10 : Sequence of the thixocasting process [05Cze].

2.5.3 Feedstock material in the thixocasting process

The three major classical methods used to produce feedstock material with a near-equiaxed microstructure suitable for subsequent thixocasting are [00Tzi, 00Tzi2]:

- Magneto-hydrodynamic casting (MHD)
- Stress induced melt activated (SIMA) process
- Spray casting

Magneto-hydrodynamic casting is the most commercialized among the three methods and it is described in a serie of patents. It involves the simultaneous cooling and shearing of a solidifying liquid alloy in a conventional continuous diecasting caster with the application of a rotating electromagnetic field [00Tzi]. The liquid metal is stirred by the electromagnetic field and cooled below the liquidus temperature by the cooling system of the caster, such that solidus nucleates at the caster walls forming dendrites, which are disintegrated by the stirred liquid [00Tzi].

In the SIMA method the alloy is heavily deformed (hot extruded to introduce a directional microstructure and afterwards cold deformed to introduce a critical level of stored energy in the alloy) and upon subsequent reheating in the semi-solid state the deformed microstructure transforms into globular grains. The transformation of the deformed dendritic microstructure into equiaxed grains is explained by the grain deformation-recrystallization model proposed by Doherty et al. [84Doh]: cold working increases the dislocation density and during reheating the microstructure is subjected to recovery and recrystallization. These new strain-free grains are characterized by high-angle grain boundaries. However, this method is limited to the size of the ingots and the process steps are numerous [00Tzi].

In spray casting the metal is melted in an induction furnace and flows through a nozzle, forming a stream of liquid metal, which is dispersed into small droplets by high pressure inert gas (usually nitrogen or argon). These droplets are solidified with a high cooling rate. While the largest droplets remain fully liquid, the smallest solidify, and droplets of intermediate sizes become semisolid. The droplets are collected on a substrate moving underneath, consolidated and further cooled on the substrate, forming a globular microstructure [00Tzi].

Other alternative and less popular processes are passive mechanical stirring and grain refinement [01Jor]. During mechanical stirring, the metal is stirred by

mechanical mixers fracturing dendrites as they are formed during solidification, resulting in equiaxed or rosette shaped microstructure. This basic concept is developed after Spencer's experiments in the 1970's but has two major drawbacks: debris is mixed into the slurry and molten metals are aggressive to the materials used in the construction of mechanical mixers [01Jor]. Grain refinement requires the use of grain refiners to achieve a fine grain microstructure that coarsens into globular grains when heated in the semisolid temperature [01Jor].

Aguilar et al. [04Agu] also describe a new rapid slug cooling technology (RSCT) involving the nucleation of grains as in the rheocasting technology. In this process, the alloy is quenched in a specially designed cooling device. Due to micro segregations within the globular grains, melting starts from the outer boundaries towards the centre during reheating into the semisolid state. Thus, it is possible to produce semisolid slurries with a well defined fraction of solid even for alloys with very low content of eutectics.

Additionally, Kleiner et al. showed that extruded AZ80 alloy spheroidizes during reheating in the semisolid range [04Kle]. The mechanisms are explained similar as in the SIMA process. The use of extruded magnesium alloys as feedstock material for thixocasting has been also successfully applied by Wagener et al. [00Wag]. This method provides a more simple technique necessitating no movement of the slurry and no complete melting of the alloy and controlled cooling devices.

3 AIMS AND OBJECTIVES

The main aim of this work is to find a relationship between the microstructure and the creep properties of two low-cost zinc-containing magnesium alloys processed by thixocasting. The thixocasting process is proposed as an alternative to conventional casting to improve microstructural features. Additionally, an alternative to high cost methods of producing precursor materials for semi-solid processing is established. The creep properties of the resulting materials in the as-cast state should be equal or better than benchmark alloy AE42.

The objectives of the present work are mainly:

1. To determine the feasibility of using extruded material as precursor material for semi-solid processing
2. To identify the process key parameters that mainly determine the thixocast microstructure of the zinc-containing magnesium alloys
3. To understand the influence of the thixocast microstructure on the creep properties of the zinc-containing magnesium alloys
4. To achieve a lower creep rate at 175°C than the state of the art AE42 alloy with comparable or higher yield strength in the as-cast state
5. To identify the underlying mechanisms of creep of the zinc-containing magnesium alloys processed by thixocasting

4 EXPERIMENTAL METHODS

4.1 Feedstock material and its processing

4.1.1 Extruded feedstock material

The feedstock materials used in the present work were the magnesium-zinc alloys MEZ (reference alloy, patented by Magnesium Elektron Ltd. in 2001, British Patent specification GB 607588) and the ZECa (experimental alloy). The materials were received as extruded bars of 75 mm diameter and 600 mm length. Both alloys were prepared and supplied by Magnesium Elektron Ltd. The MEZ alloy is a high content rare-earth alloy according to MEZ specifications while the ZECa alloy is an experimental alloy that compensates the reduction of rare earths with calcium and zinc. The rare earth additions were done using MM (Misch Metal), which is an alloy containing Ce (approximately 45 to 52 %), La (20 to 27 %), Nd (15 to 18), Pr (3 to 5) and traces (1 to 3) of other elements like Sm, Tb, and Y as well as Ca, Si and Fe [11Wik].

4.1.2 Partial remelting of the extruded alloys

The microstructural evolution of the feedstock material during its partial remelting (reheating) was analyzed in order to investigate the microstructural changes occurring during heating of the extruded material before its processing into the semi-solid state. In this way, the evolution of the grains starting from the extruded state was thoroughly studied in order to verify that spherodized grains, necessary to reach a semi-solid state, can be obtained.

The range of reheating temperatures related to the semi-solid state was selected after DTA results, starting with temperatures before phase melting peaks, and finishing before complete melting of the materials. For the MEZ alloy the selected temperatures were 400 to 640°C, while for the ZECa alloy, the selected temperatures were 350 to 620°C. In both cases, steps of 50°C up to 600°C were done to evaluate the microstructure after reheating.

For these experiments, the extruded material was cut into cubic coupons of approximately 10 mm x 10 mm x 10 mm. Coupons were heated inside of an electrical convection oven and held there five minutes after stabilization of the desired temperature and subsequently quenched in water at room temperature

(approximately 25°C). This exposure time was chosen with respect to a typical time used for the heating and handling of the metal when transferring it to the squeeze casting equipment. At temperatures of 600°C and more, the coupons were wrapped with steel sheets to avoid oxidation and eventually burning of the materials.

The time required to reach every test temperature (from 3 up to 7 minutes) was previously determined using dummy coupons and thermocouples type K, which were inserted in the middle of the samples.

4.1.3 Semi-solid casting of the extruded alloys

The thixocast plates were produced by LKR (Leichtmetallkompetenzzentrum) in Ranshofen, Austria, using a vertical Squeeze-Casting machine (UBE HVSC 350). The process was already illustrated in Fig. 6. The extruded billets were heated up in an open steel crucible by means of an induction coil. The temperature was monitored by using a thermometer in contact with the slurry. The material was first heated up to 25°C above the chosen cast temperature and then allowed to cool down slowly after switching off the induction coil. The semi-solid slurry was carried and poured manually into the inclined shot sleeve of the casting machine, where the pressure reached up to 86 MPa and the piston speed was 1 m/s in average. The mould cavity was preheated to 260°C. The semi-solid processing temperatures were chosen as 615°C for the ZECa alloy and 640°C for the MEZ alloy to assure semi-solid state with a solid fraction of 40 to 60%. The proposed solid fraction is used in aluminium casting alloys because it is possible to handle the semi-solid specimen like solid.

The final products were stepped plates with dimensions of 110 mm x 250 mm and thicknesses of 2, 6, 10 and 14 mm. The geometry and dimensions are shown in Fig. 11. The base of the casting samples was not considered for the present work.

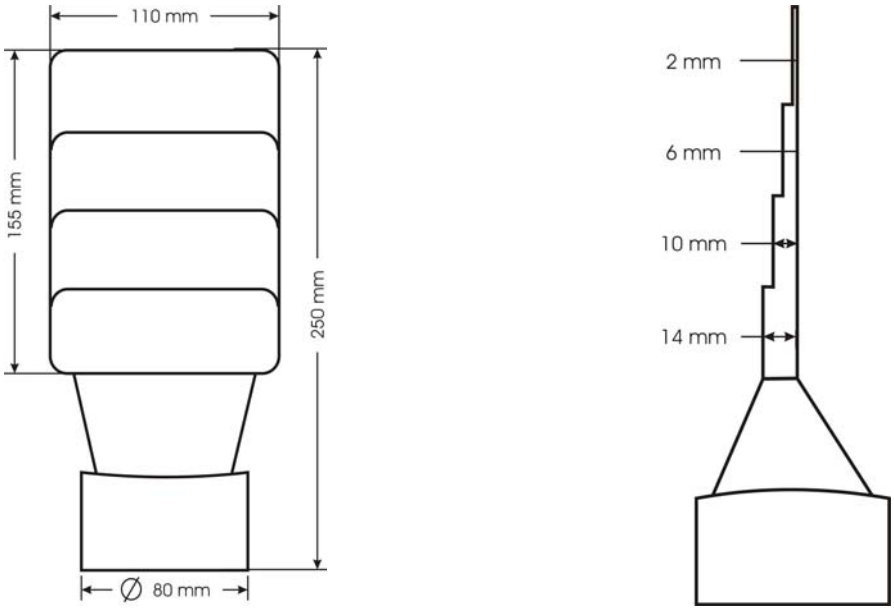

Fig. 11 : Geometry and dimensions of castings made by thixocasting of magnesium alloys

4.1.4 Aging of the thixocast alloys

Heat treatments were carried out to investigate the influence of temperature without stress on the microstructure of the as-cast alloys. They served as a reference for the creep studies. For the heat treatments, the 10 and 14 mm steps of the thixocast plates were reduced by grinding down with SiC paper both sides of the plates to 5 and 7 mm respectively in order to isolate the bulk microstructure. The ground plates were cut into coupons of 15 mm x 20 mm approximately. Electric furnaces were heated to the test temperatures and soaked for 12 hours before introducing the samples. Aging in air of the alloys without prior solution heat treatment (T5 temper designation) was made at temperatures of 135°C, 150°C, 175°C and 200°C. The temperature inside the furnaces was maintained within ±3°C. The coupons were exposed to temperature up to 200 h and at different intermediate times (20 h, 50 h, 100 h) a coupon was taken out of the furnace and cooled by quenching in water at room temperature to freeze the microstructure developed at that condition. The coupons obtained from a single step were all used for one temperature in order to assure a similar bulk microstructure every selected time. With the purpose of determining microstructural changes, the coupons were characterized subsequently by scanning electron microscopy and hardness measurement.

In order to better detect the fine precipitation after aging in the micrographs taken by SEM, the digital picture editor Adobe Photoshop® was used to dramatize contrast.

4.2 Characterization techniques

4.2.1 Differential thermal analysis

The Differential Thermal Analysis (DTA) technique was applied to determine the semi-solid range of the studied alloys. Coupons of ca. 0.5 mm^3 were carefully prepared from the extruded precursor material and analysed with a Mettler Toledo model TGA/SDTA 851e. The coupons were inserted in stainless steel crucibles of 5 mm diameter and closed with a cap of the same material. Pure aluminum was employed to calibrate the DTA and as reference material. To avoid oxidation and burning of the magnesium samples, pure argon gas at a rate of 50 ml/min. circulated in the system during the experiments. The temperature was varied from 25°C to 700°C with a heating/cooling rate of 10°C/min.

4.2.2 X-ray diffraction

The phases of the alloys in the extruded and the thixocast condition were identified using the technique of X-ray diffraction aided by JCPDS diffraction standards (Joint Committee on Powder Diffraction Standards). For this purpose, a Siemens D5000 diffractometer equipped with a secondary monochromator was employed. A current of 40 mA at a voltage of 40 kV was used during the measurements. The samples were scanned over a range of 30° to 90° at a step size of 0.05° and 10 sec/step. The Powder Diffraction Files (PDF) used in the present work were:

- PDF#12-0266, $Ca_2M_g6Zn_3$
- PDF#13-0450, $CaMg_2$
- PDF#17-0401, $Mg_{12}Nd$
- PDF#35-0821, Mg

It should be emphasized that phases present in small quantities (below 5%) cannot be detected by this technique.

4.2.3 Metallographic sample preparation

In order to characterize the microstructural features of the alloys in their different states (extruded, partial remelting, thixocast, heat treated, and after mechanical and creep tests), it was necessary to prepare them using metallographic techniques adapted for magnesium alloys. The samples were firstly cut and embedded in epoxy resin to facilitate their preparation. The specimens were then ground with 500, 800,

1200 and 2500 SiC grit paper using water as cooling fluid and ethylic alcohol as cleaning agent between grinding steps. The samples were polished with OPS™ neutral suspension (0.05 μm SiO_2) and distilled soapy water for a few minutes (up to 3 minutes) to avoid oxidation. The samples were then washed with distilled water followed by ethylic alcohol and dried with warm flowing air.

After the metallographic preparation, the samples were etched chemically for the purpose of contrasting grain boundaries and phases and determining grain size and orientation by means of optical microscopy. The etching solution was prepared after Kree [04Kre] with 110 ml ethylic alcohol, 40 ml distilled water, 2 ml acetic acid and 2 gr. picric acid at room temperature. The polished samples were immersed in the etching solution for a few seconds until the surface changed its colour. The samples were then washed immediately with ethylic alcohol and dried with hot air.

The microstructure developed at the different steps of representative casting material is presented as micrographs, in order observe the complete thickness of the step casting sample. Fig. 12 shows schematically where the micrographs come from.

Fig. 12: Sketch of the casting indicating the area (shady) selected for the micrographs.

4.2.4 Optical microscopy

The microstructure of the samples after chemical etching was determined using a Leica upright optical microscope type DM LM equipped with polarisation filters and a Nikon digital camera type DM1200. The largest magnification available in the equipment was 1000x. The microscope was coupled with the image analysis software (Aquinto AG), which allowed the determination of average grains sizes

according to the linear interception standard method described in ASTM E112-02 [02AST].

4.2.5 Scanning electron microscopy (SEM) coupled with EDX

A Zeiss Scanning Electron Microscope (SEM) model DSM 962 was used to resolve the microstructure of the alloys at higher magnifications and to obtain chemical information of the phases developed in the materials. The specimens were metallographically prepared as described above for optical microscopy. In the case of mounted specimens, it was necessary to use silver painting to assure electrical contact between the polished metallic surfaces and the microscope chamber to avoid charging of the samples. Chemical etching was not necessary, because this technique, in combination with the signal mode Backscattered Electron (BSE), allows phases contrast according to their atomic weight. Fracture analysis was made using the signal mode Secondary Electron (SE), which allow topographic imaging. The chemical characterization of the phases as well as its quantification (semi-quantitative analysis) was made by means of the analytical technique of Energy Dispersive X-ray Spectroscopy (EDX) and with the help of the microanalysis system WINEDS, Version 3.0. An accelerating voltage of 15 keV was used during signal acquisition.

4.2.6 Transmission electron microscopy (TEM)

Transmission electron microscopy (TEM) was used at Risø DTU National Laboratory for Sustainable Energy (Roskilde, Denmark) to observe at micro-scale precipitates and substructures developed after casting and after creep tests in the reference alloy (MEZ). The deformed specimens were ground mechanically to about 70 μm and then thinned via electropolishing in a twin jet system using a solution of 5% $HClO_4$ and 95% ethanol at about -30°C and with a voltage of 40 V. After electropolishing, the specimens were cleaned with ethanol several times and then dried. The observations were performed on a JEOL 2000 transmission electron microscope coupled with an energy dispersive X-ray analysis (EDX) system operating at 200 kV. All TEM images were taken under two-beam diffraction conditions using different diffractions vectors and bright field mode.

4.3 Mechanical tests of the thixocast alloys

4.3.1 Hardness tests

Hardness measurements were conducted to characterize the microstructural changes after temperature exposure of the material due to matrix hardening or softening. For the hardness measurement the samples were embedded in resin and grinded 1200 grid SiC paper to ensure planarity of the surface. Indents and evaluation of the Vickers hardness test were conducted with an Emco-Test hardness tester. The Vickers hardness measurements were conducted according to DIN EN ISO 6507-1 [05DIN] with a force of 98.1 N (HV 10) and an indentation time of 10 s.

4.3.2 Tensile and compression tests

Uniaxial tensile and compression tests were performed at room temperature using a constant strain rate of 10^{-3} s^{-1}. For this purpose, an 1195 Serie Instron machine was used. The elongation was measured by optical means, using a laser beam which measured the distance between two marks on the gauge length. The tensile specimens were machined from the 10 mm and 14 mm steps of the thixocast alloys in the as-cast state according to the standard DIN 50 125 [00DIN] with a gauge length of 60 mm, 6 mm diameter and screw heads. At least three specimens were tested for every alloy to obtain the value of 0.2% proof stress, tensile strength and elongation. Cylindrical compression specimens of ratio 1.5:1 (15mm:10mm) were machined from the same steps.

4.3.3 Tensile creep

Round creep specimens were machined from the 10 and 14 mm steps of the alloys in the as-cast state. Creep tests were conducted at constant stress on specimens with a gauge diameter of 5 mm and a gauge length of 30 mm. The specifications of the specimens are according to the standard DIN 50 125 [00DIN] and are shown in Fig. 13.

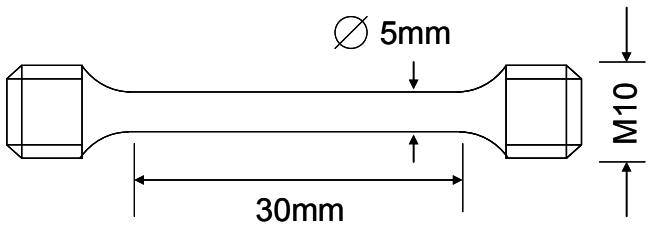

Fig. 13 : Geometry of samples used for creep experiments.

For the creep tests, creep machines of ATS (Applied Test Systems Inc.) equipped with electric furnaces were used, Fig. 14. The machines were connected to a main computer, equipped with the WIN CCS 2 software, which acquired data at 1 minute intervals. The furnaces were heated at a rate of 100°C/h, followed by a soaking time of 30 minutes to homogenize the temperature of the chamber. Once the set-point was reached, the stress was applied within approximately one minute. The temperature inside the chamber was maintained constant within ±1°C. The studied parameters were 135, 150, 175 and 200°C and stresses of 50, 60, 70, 80, 90 and 100 MPa. The specimens crept in average during 200 hours, if failure did not occur before this time span. Creep strain was measured by two extensometers which were attached close to the gauge section of the specimens.

Once the creep data were acquired with the WIN CCS 2 software, the data analysis software Origin® was used to draw the creep curves and to determine the slope of the secondary region of the curves, i.e. the secondary creep rate. The secondary or minimum creep rates were needed for the calculation of the creep parameters.

(a) (b)

Fig. 14 : Experimental setup for the conduction of the creep experiments of thixocast magnesium alloys.

5 MICROSTRUCTURAL CHARACTERIZATION

5.1 MEZ-System

5.1.1 Characterization of the extruded feedstock material

5.1.1.1 Hardness and chemical composition

The measured hardness of the as-received MEZ material is 52.1 ±1.1 HV10.

The chemical composition as reported by the supplier is given in Table 4.

Table 4 : Composition of the MEZ extruded bars (in wt. %) as reported by the supplier (MEL), magnesium based.

Al	Cu	Fe	Mn	Ni	Si	Zn	Zr	RE
<0.01	<0.01	0.003	0.13	0.001	<0.01	0.4	0.12	2.6

5.1.1.2 Microstructure

The microstructure of the as-received extruded MEZ material is presented in Fig. 15, transversal and parallel to the extrusion direction. The grain size is quite heterogeneous, as can be seen in Fig. 15 (a), with an average grain size of approx. 10 µm ± 7 µm in the transversal direction. The extrusion direction shows a bimodal grain size distribution with elongated and equiaxed grains as well as the presence of intermetallic phases aligned in stringers, Fig. 15(b).

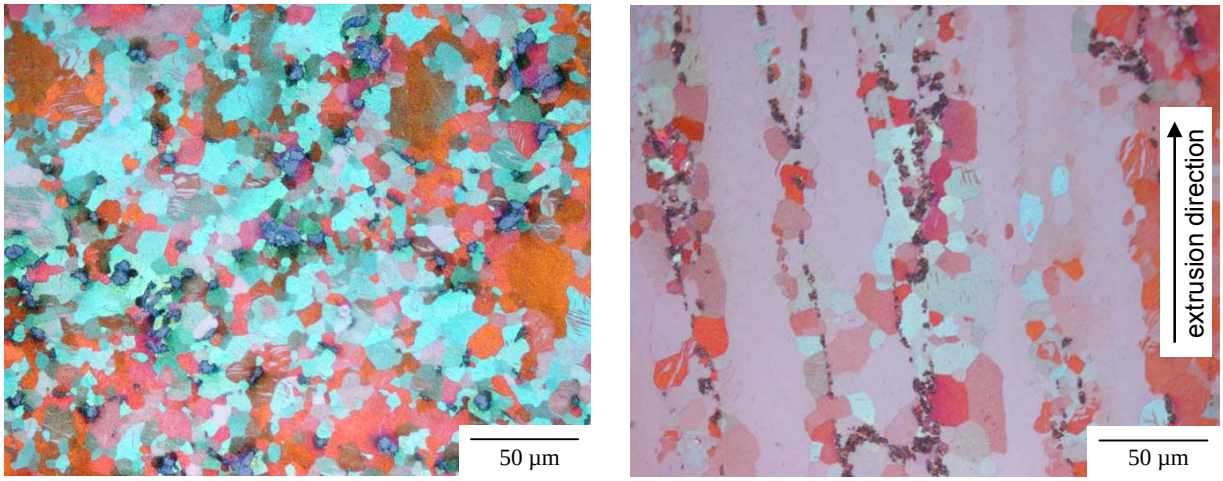

(a) Transversal view, extrusion direction (b) Longitudinal view, extrusion direction

Fig. 15 : Extruded feedstock material MEZ as received, optical microscopy.

5.1.1.3 Phase identification

The X-ray diffraction pattern of the extruded MEZ alloy shows only two dominant phases in the extruded condition, i.e. the α-Mg and the $Mg_{12}RE$, see Fig. 16.

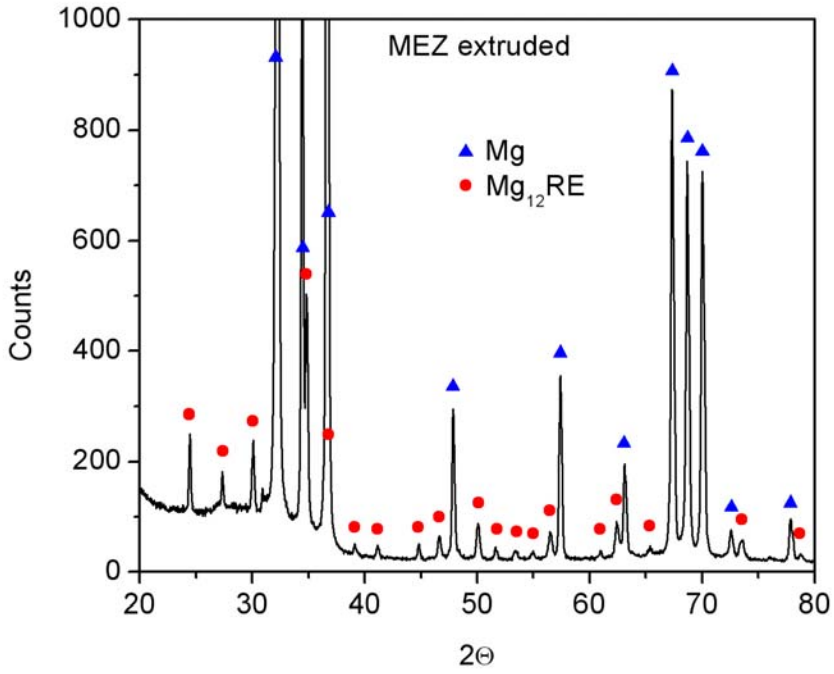

Fig. 16 : X-ray pattern of the MEZ alloy in its extruded condition.

As already observed by X-ray diffraction, the SEM pictures (Fig. 17) confirm that two phases are mainly present in the MEZ alloy in its extruded condition (α-Mg and $Mg_{12}RE$ particles). Particles of Mn_2Zr, which appear sparingly and combined with the $Mg_{12}RE$ phase, are also present, as indicated in Fig. 17 (a). The $Mg_{12}RE$ phase is aligned parallel to the extrusion direction and appears as strings of fractured particles. Very small amounts of Mn_2Zr particles are also detected in the matrix, as well as micro particles of $Mg_{12}RE$.

The phases detected in the extruded MEZ alloy, as well as their semi-quantitative analysis after SEM-EDX, are summarized in Table 5. The $Mg_{12}RE$ phase is considered as solid solution because some zinc is present in the chemical composition, meaning that zinc atoms are substituting magnesium atoms in the crystal structure.

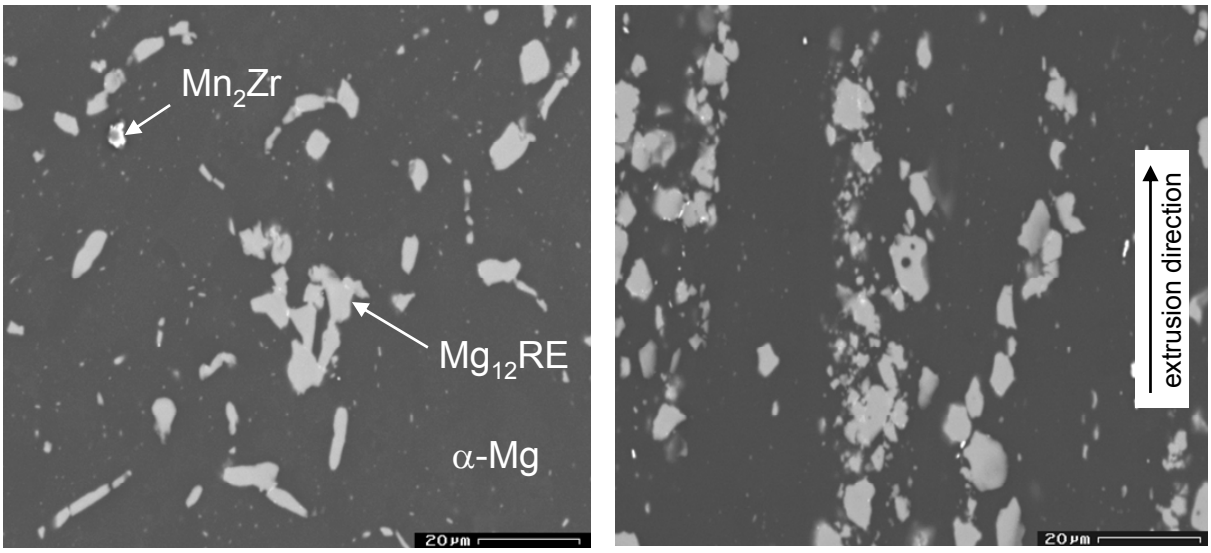

(a) Transversal view, extrusion direction (b) Longitudinal view, extrusion direction

Fig. 17 : Extruded MEZ alloy, SEM-BSE.

Table 5 : Phases identified by SEM-EDX in the extruded MEZ alloy and their composition (wt. %).

%Mg	%Zn	%Mn	%Zr	%La	%Ce	%Nd	Interpreted phase
55-60	3.7-6			11.5-16	19-23	3-4	$(MgZn)_{12}RE$
8-14		47-48	31-40				Mn_2Zr
100							α-Mg

5.1.2 Characterization of the extruded material during its partial remelting

Reheating of the feedstock material was performed in order to verify that spherodized grains, necessary to reach a semi-solid state, can be obtained after partial melting of the extruded material. The range of reheating temperatures related to the semi-solid state was selected after DTA results. All specimens were hold five minutes at the testing temperature, if not otherwise stated.

5.1.2.1 DTA analysis

The identification of the phase changes and respective temperatures taking place during heating in the semi-solid range was carried out by Differential Thermal Analysis (DTA) measurements.

The DTA curve of the MEZ extruded material is displayed in Fig. 18: Two peaks corresponding to the melting of the alloy can be observed in the heating curve. The eutectic temperature of the Mg-Ce system is reported as 592°C [92Nay], following the transformation L → α–Mg+$Mg_{12}RE$. Therefore, the partial melting peak with an onset of 587°C can be attributed to this transformation. The second large peak can be attributed to the melting of the magnesium α-grains at 645°C.

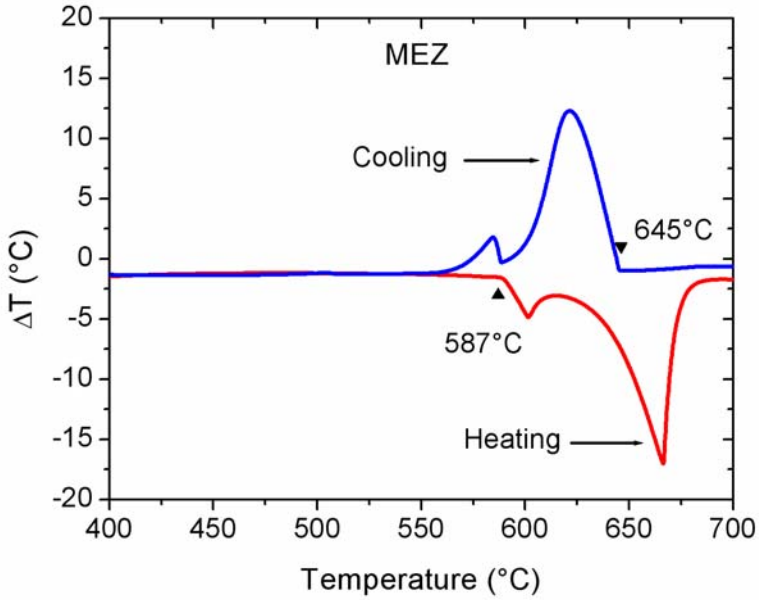

Fig. 18 : Experimental DTA curves for heating and cooling at 10°C/min of the extruded MEZ alloy.

For the cooling, slightly lower temperatures of transformation are observed due to the undercooling of the melt. This hysteresis has to be considered also in the practical process, where 10°C / min. of heating and cooling can appear. The MEZ alloy has, therefore, a relatively narrow melting and solidification temperature, which ranges from about 587-645°C, resulting in about 60°C of semi-solid range.

The range of reheating temperatures was selected after DTA results, starting with temperatures before phase melting peaks, and finishing before complete melting.

5.1.2.2 Microstructural evolution

After determining the semi-solid temperature (already reported as 587 to 645°C), the reheating temperatures for the MEZ alloy were selected from 450 to 600°C in intervals of 50°C and intervals of 20°C at 600°C and above to observe recrystallization, dissolutions and phase transformations.

Fig. 19 and Fig. 20 show the developed microstructure of the extruded material as a function of the temperature applied. No significant microstructural change was observed after heating to 450°C for 5 min., (Fig. 19 (a + b)) as compared to the as extruded MEZ material (Fig. 15 (b) and Fig. 17 (a)). The phase distributions, as well as the grain size, are comparable. However, as can be observed by comparing the next micrographs of Fig. 19, grain coarsening occurs when the material is heated to 500°C, Fig. 19 (d). The distribution and morphology of the secondary $Mg_{12}RE$ phase is not affected as can be seen in the SEM micrograph, Fig. 19(c). The higher temperature of 550°C does not result in further change as compared to 500°C, Fig. 19 (e + f).

A strong change of microstructure occurs between 550° and 600°C, Fig. 20 (a + b), corresponding to the partial melting temperature, starting at 587°C (see Fig. 18). The main part of secondary phase has already formed eutectic melt when heated to 600°C. Correspondingly, a typical eutectic microstructure is observed at the grain boundaries and also inside the grains. Additionally, the grain growth is several times larger than at lower temperatures, resulting in grain sizes of the order of 50 µm. The area of eutectic melting increases continuously with further increasing temperature, as seen by optical and scanning electron microscopy, Fig. 20(c) to (f).

At higher temperatures of exposure (640°C), the formation of smaller or secondary grains is observed, which may be formed during quenching of the melt. Additionally, the formation of spherodized grain boundaries at the α-grains is also observed. The amount of the spherodized grain boundaries is increased, and the amount of the secondary grains is decreased when the holding time is longer at higher temperatures (Fig. 21).

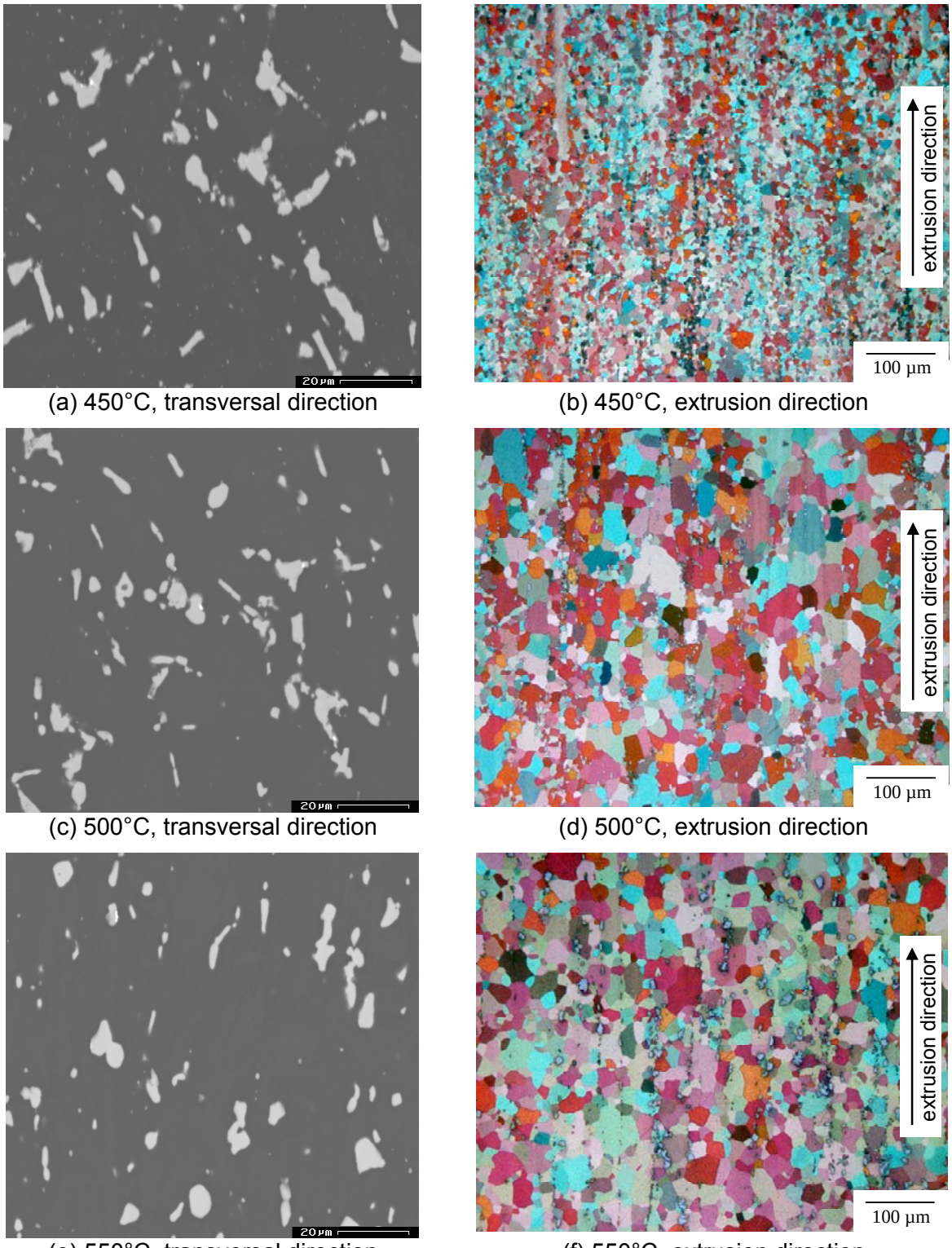

(a) 450°C, transversal direction

(b) 450°C, extrusion direction

(c) 500°C, transversal direction

(d) 500°C, extrusion direction

(e) 550°C, transversal direction

(f) 550°C, extrusion direction

Fig. 19 : Microstructure of the extruded MEZ alloy after reheating at 450°C, 500°C and 550°C as analyzed by SEM (left) and optical microscopy (right).

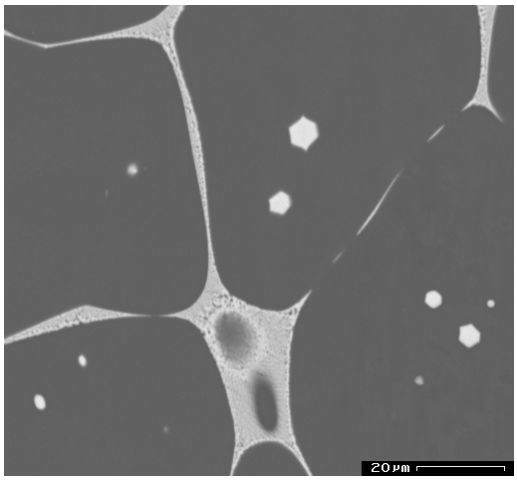

(a) 600°C, transversal direction

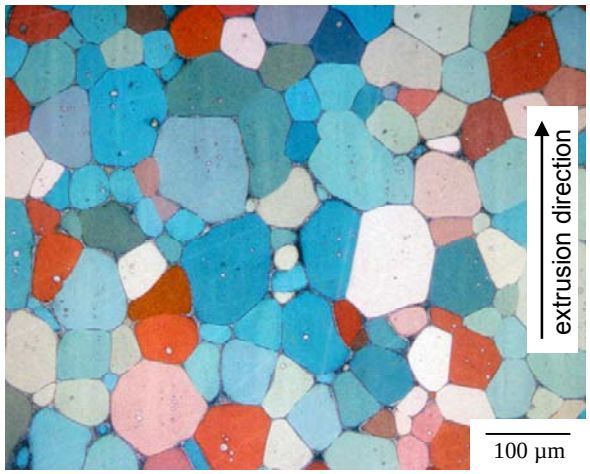

(b) 600°C, extrusion direction

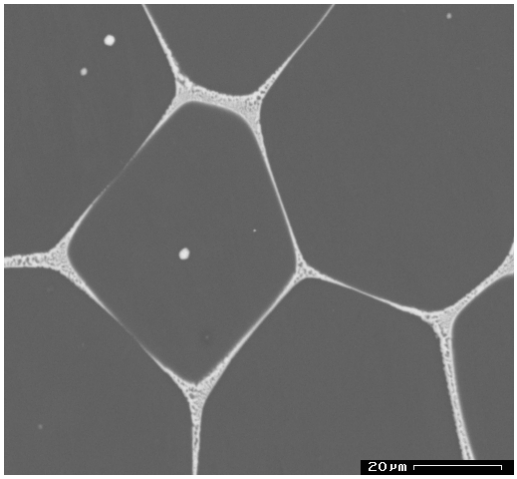

(c) 620°C, transversal direction

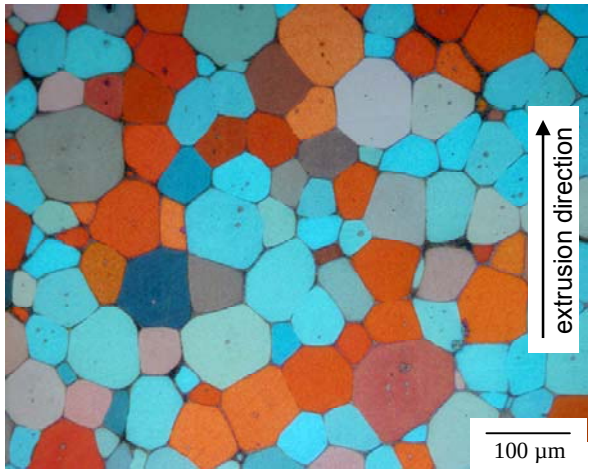

(d) 620°C, extrusion direction

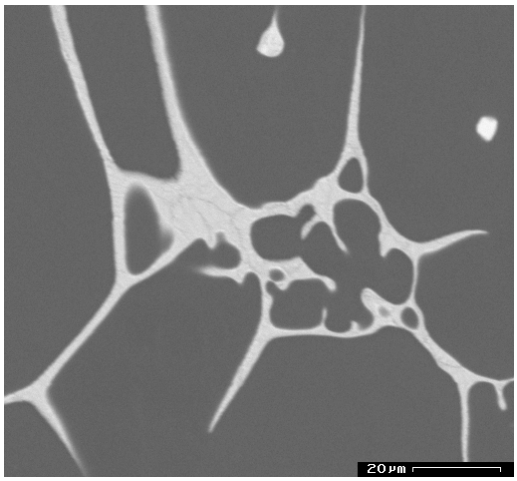

(e) 640°C, transversal direction

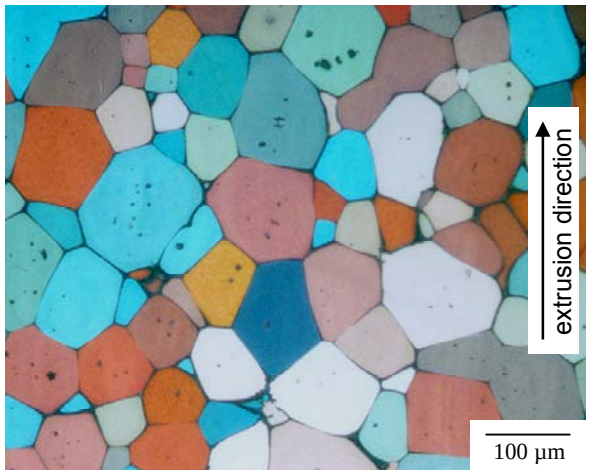

(f) 640°C, extrusion direction

Fig. 20 : Microstructure of the extruded MEZ after reheating at 600°C, 620°C and 640°C as analyzed by SEM (left) and optical microscopy (right).

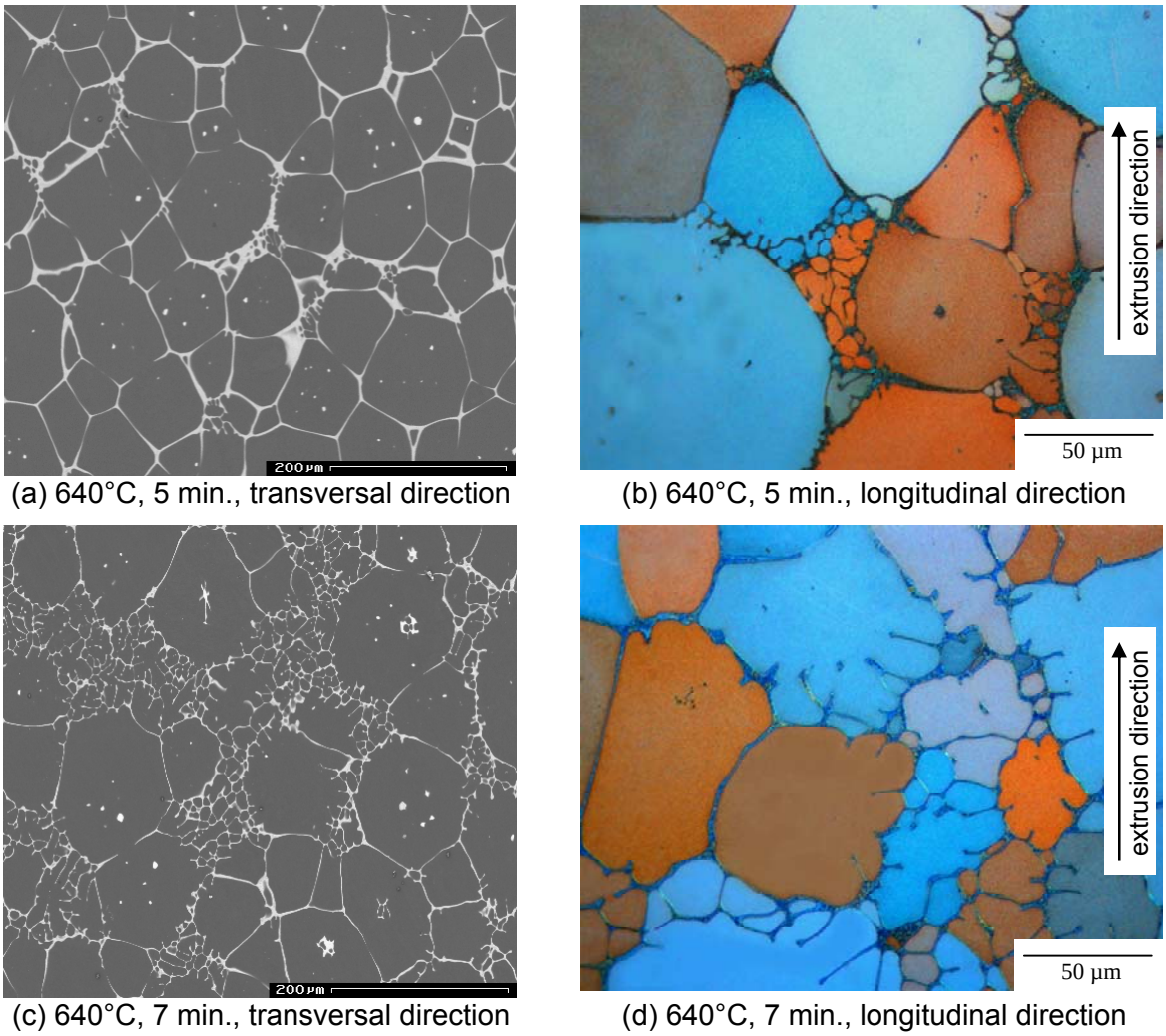

(a) 640°C, 5 min., transversal direction

(b) 640°C, 5 min., longitudinal direction

(c) 640°C, 7 min., transversal direction

(d) 640°C, 7 min., longitudinal direction

Fig. 21 : Microstructure of the extruded MEZ after reheating at different times at 640°C as analyzed by by SEM (left) and optical microscopy (right).

5.1.2.3 Grain size evolution

Fig. 22 shows the grain growth as determined metallographically. It can be seen that due to recrystallization already before the first melting temperature of 587°C detected in Fig. 18 grain growth takes place. The effect of grain growth is significantly increased when the secondary phase is melted at 600°C and still increasing with higher temperature indicating that Ostwald ripening adds to the effect of recrystallization. In summary, the MEZ alloy shows a grain growth behaviour divided into two ranges from 400°C to 587°C, where slow grain growth prevails and above 587°C, where strong grain growth occurs.

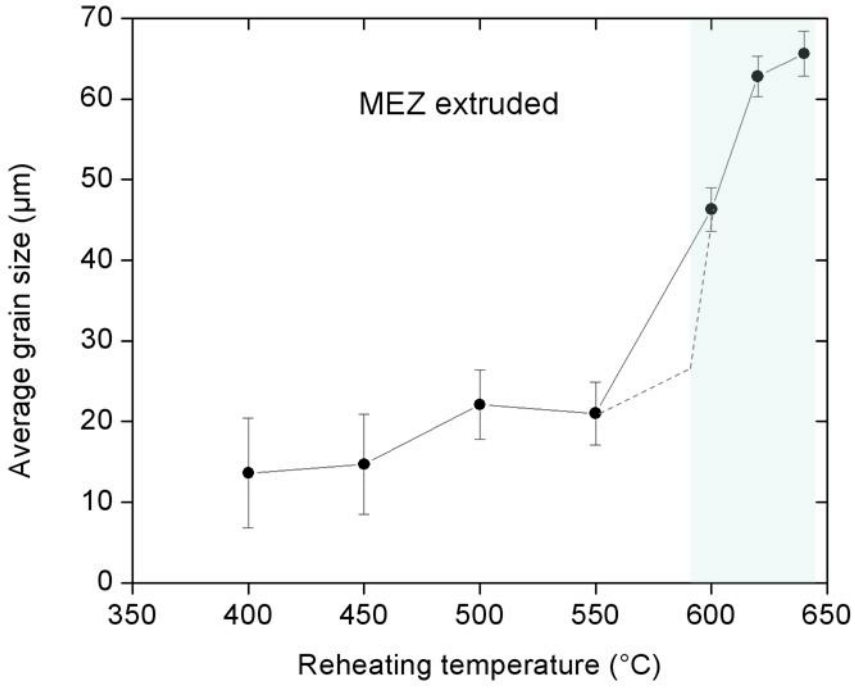

Fig. 22 : Evolution of the grain size of α-Mg in the extruded MEZ material after reheating during five minutes at different temperatures.The shadow area represents the melting peak of the eutectic and the dotted lines the expected course of the grain growth.

5.1.3 Characterization of the thixocast material

5.1.3.1 Chemical composition

The chemical composition of the MEZ alloy after thixocasting was determined by means of the Inductively Coupled Plasma technique (ICP). The results of the analysis are shown in Table 6.

Table 6 : Chemical composition of the processed MEZ material (in wt. %) measured by ICP, magnesium based.

Al	Fe	Mn	Ni	Si	Zn	Zr	Ce	La	Nd	Pr
<0.01	0.001	0.2	0.002	<0.01	0.5	0.1	1.7	0.7	0.5	0.2

5.1.3.2 Microstructure at lower magnification

Fig. 23 and Fig. 24 show overviews of the complete microstructure of the thixocasting MEZ material at different thicknesses. Two representative casting samples were chosen to show the variability of the resulting microstructure. In general, globular-

and rosette-like mixed morphology is observed through the whole thickness of the plate. Additionally, the typical microstructural features such as spherodized grain boundaries and secondary α-grains can be seen as were already observed in the reheating experiments, section 5.1.2.2. Correspondingly, the mould has been completely filled and only small amount of pores is present.

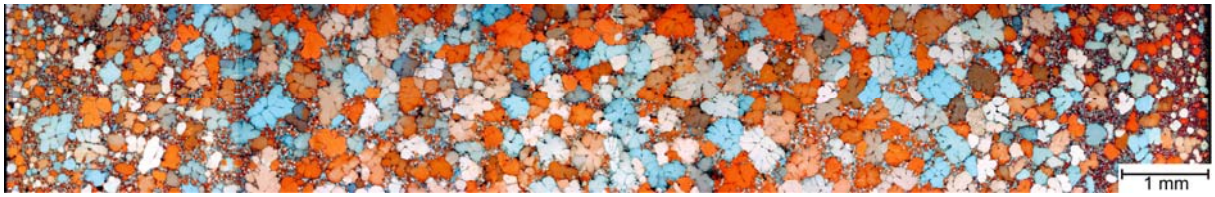

(a) Casting A, 14 mm thickness

(b) Casting B, 14 mm thickness

(c) Casting A, 10 mm thickness

(d) Casting B, 10 mm thickness

Fig. 23 : Complete cross section of two representative casting samples of MEZ, 14 and 10 mm steps (rims are at both extremes, to the left and to the right).

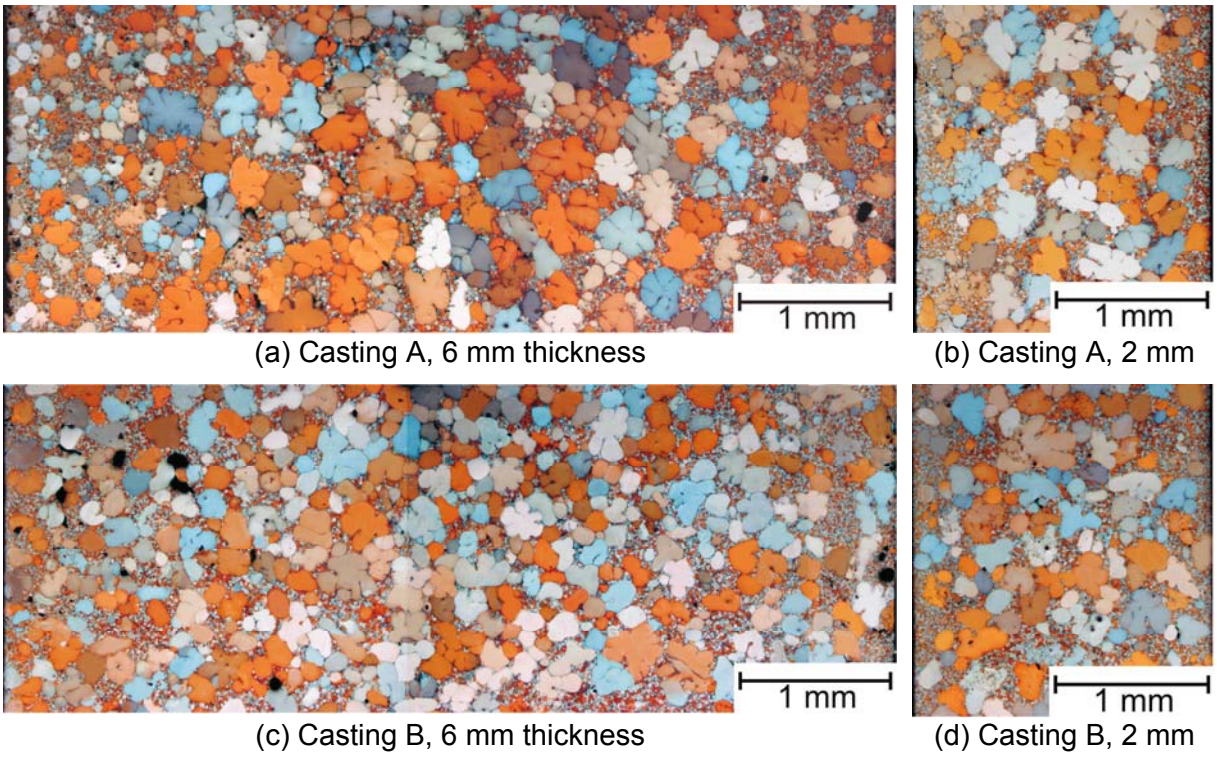

(a) Casting A, 6 mm thickness (b) Casting A, 2 mm

(c) Casting B, 6 mm thickness (d) Casting B, 2 mm

Fig. 24 : Complete cross section of two representative casting samples of MEZ, 6 and 2 mm step (rims are at both extremes of every micrograph, to the left and to the right).

As can be seen on the 14 and 10 mm steps, Fig. 23, the largest grains, of the order of 150-300 µm, can be found in the core of the casting steps. The rims show smaller and more globular grains, of the order of 100 µm and less, as well as a higher amount of finer grains.

The same trend of microstructural variation with respect to the relative position to the rim of the sample can also be found in the steps from 6 down to 2 mm, Fig. 24. When comparing the different steps of the castings, the grain size does not show a tendence of grain refinement as the steps become thinner. The grain size at the rim and at the center is therefore comparable between the different steps.

5.1.3.3 Microstructure

Fig. 25 shows a closer look of the spherodized grain boundaries and areas of small grain formation. The globular- and rosette-like form of primary α-grains is observed at detail in Fig. 25 (a) and (c). A mixture of secondary α-grains and eutectic is formed at the grain boundaries, as observed in Fig. 25 (b) and (d). Large and small grains are preferably completely wetted by the eutectic phases. If compared to the partial melting experiments at 620°C, Fig. 20, it can be stated that the amount of small grains is higher in the casting, corresponding to the higher experimental temperature

of 640°C, Fig. 21. Additionally, the grain size of primary α-grains is higher than in the partial melting experiment, amounting to typically 200 µm. The small grains are typically of globular shape with about 10-15 µm in size and often also exhibit spherodized grain boundaries. The eutectic in large volumes of secondary phase is rather inhomogeneous, while at regions with α-grains located close to each other typical features of a partially divorced eutectic may be present, see Fig. 25(d).

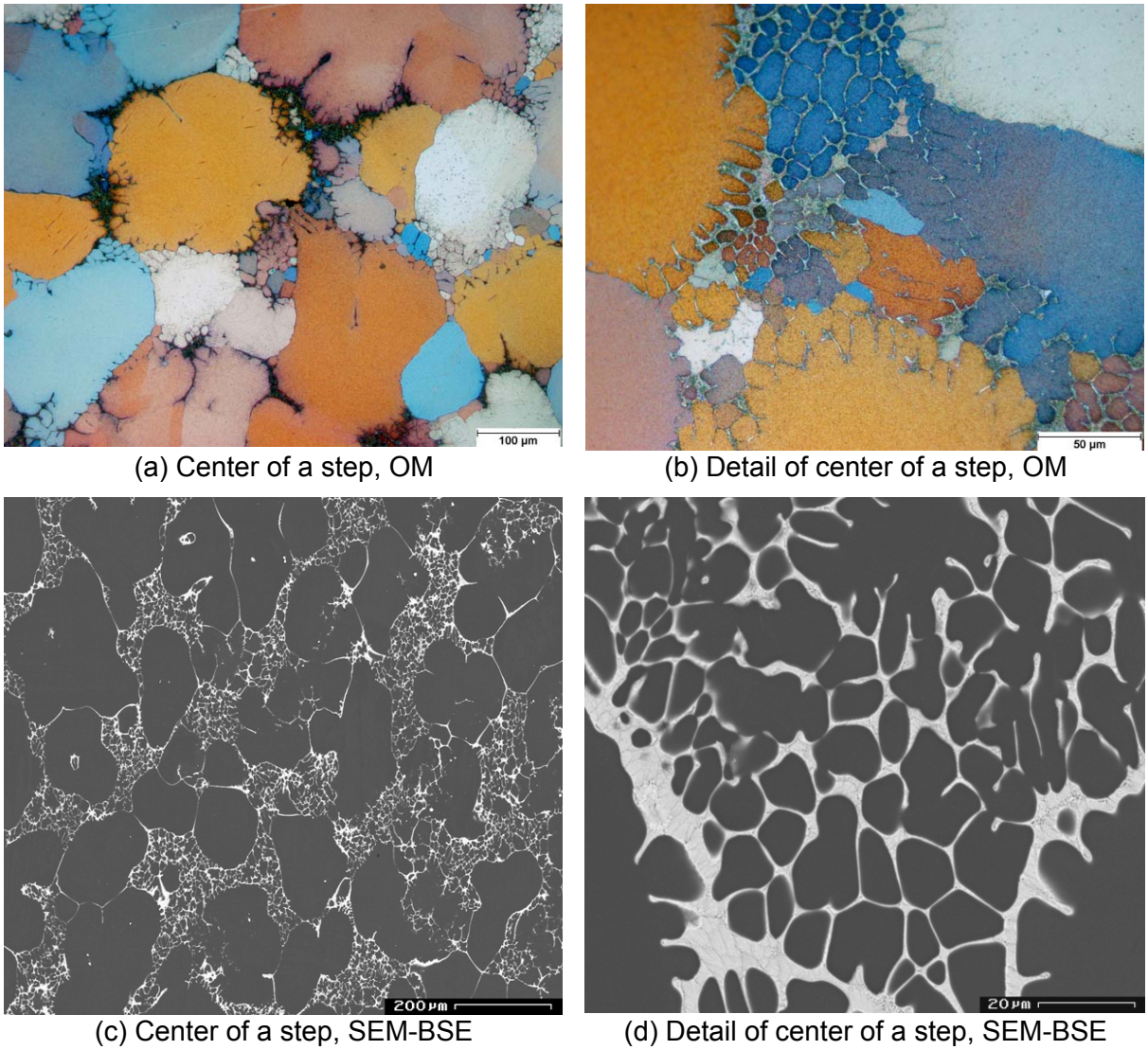

(a) Center of a step, OM

(b) Detail of center of a step, OM

(c) Center of a step, SEM-BSE

(d) Detail of center of a step, SEM-BSE

Fig. 25 : Typical microstructure of the thixocast MEZ in the middle of a step.

At the rim and at the outer regions of the casting, the eutectic phase is homogenously distributed in the microstructure and the α-grains tend to be more globular, Fig. 26 (a + b), with some exceptions, like in Fig. 26 (c + d). Mn_2Zr phases can be evidenced in this section of the thixocast material, Fig. 26(b). These phases appear bright in the BSE mode of the SEM because of the contrast based on the atomic number (phases with higher atomic number appear brighter than the rest).

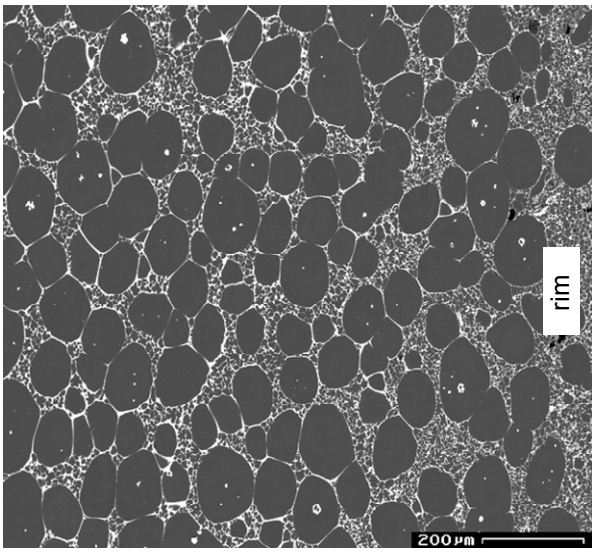

(a) Detail of the rim, SEM-BSE

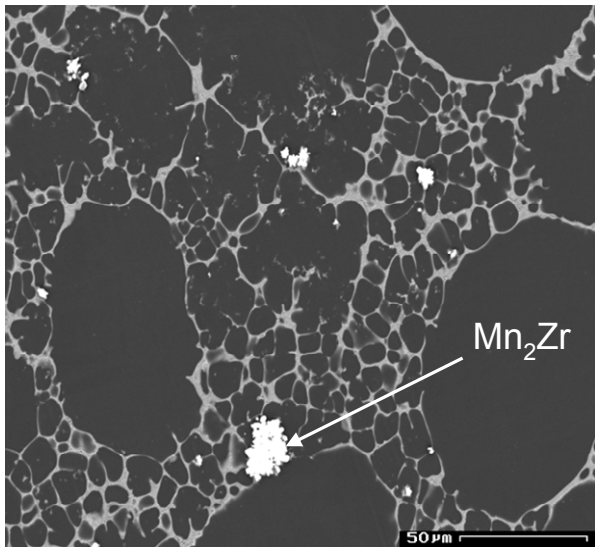

(b) Detail of the rim, SEM-BSE

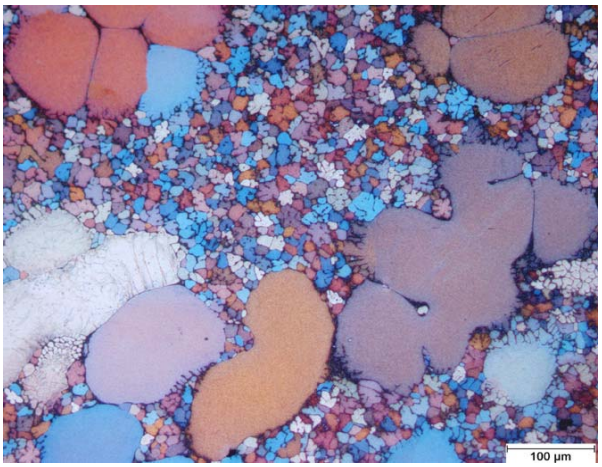

(c) Detail of the rim, OM

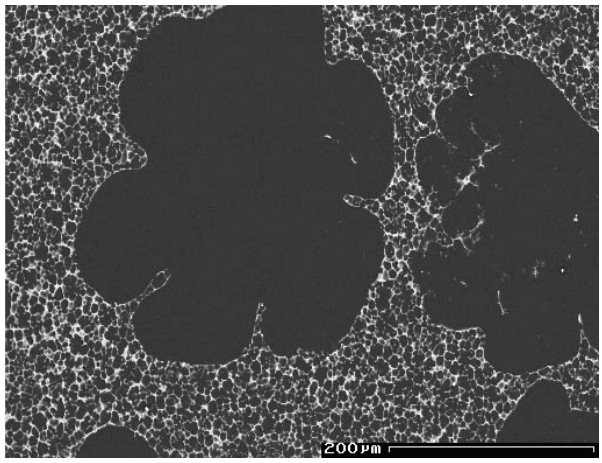

(d) Detail of the rim, SEM-BSE

Fig. 26 : Typical microstructure of the thixocast MEZ close to the rim of a step.

Transmission electron microscope picture in Fig. 27 (a) show typically alignments of plates of about 100 nm dimension. These plates tend to be arranged in the same direction within one grain. The orientation of the plates is independent of the orientation of the alignments, although the alignments are arranged typically in a common direction, exhibiting a wavy shape. Additionally, some alignments are found in a perpendicular direction, forming in some cases networks, like in Fig. 27 (b).

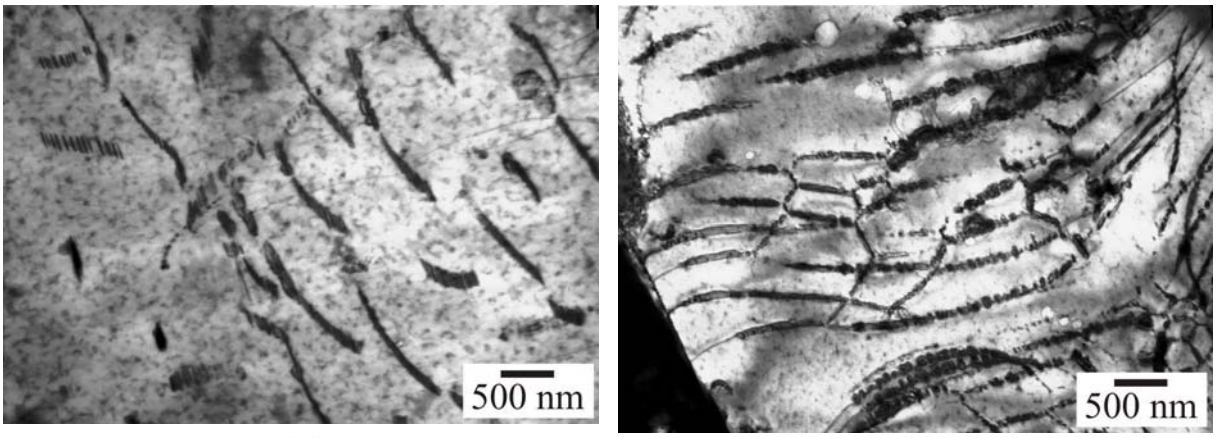

(a) (b)

Fig. 27 : Transmission electron microscopy of the thixocast MEZ alloy.

5.1.3.4 Phase identification

Fig. 28 shows the X-ray diffraction pattern of the thixocast MEZ alloy. The only phases detected by this technique are Mg and $Mg_{12}RE$, as in the extruded material.

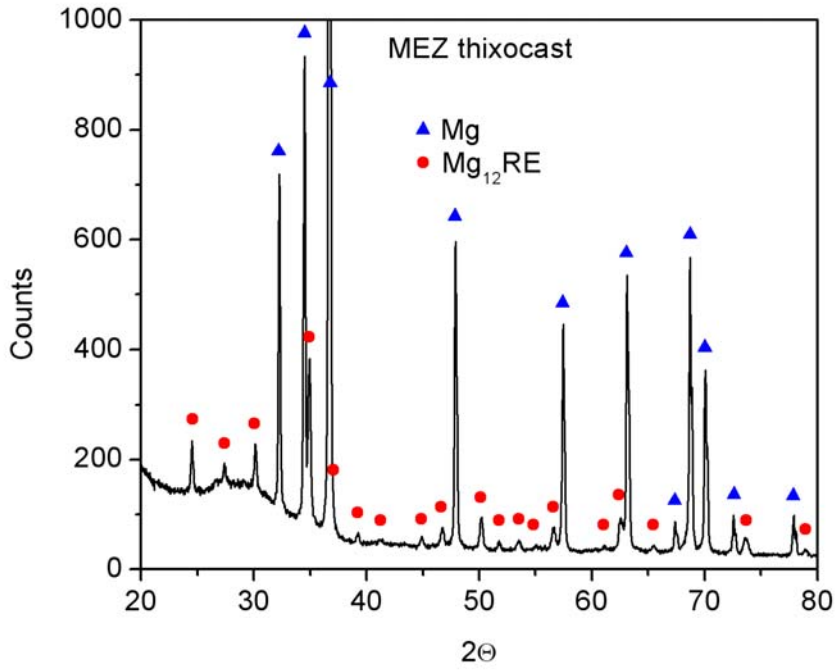

Fig. 28 : X-ray pattern of the MEZ alloy in its thixocast condition.

The phases identified by X-ray diffraction were corroborated by SEM-BSE and are indicated in Fig. 29 making the distinction between the primary solidified α-Mg and the secondary solidified α-Mg.

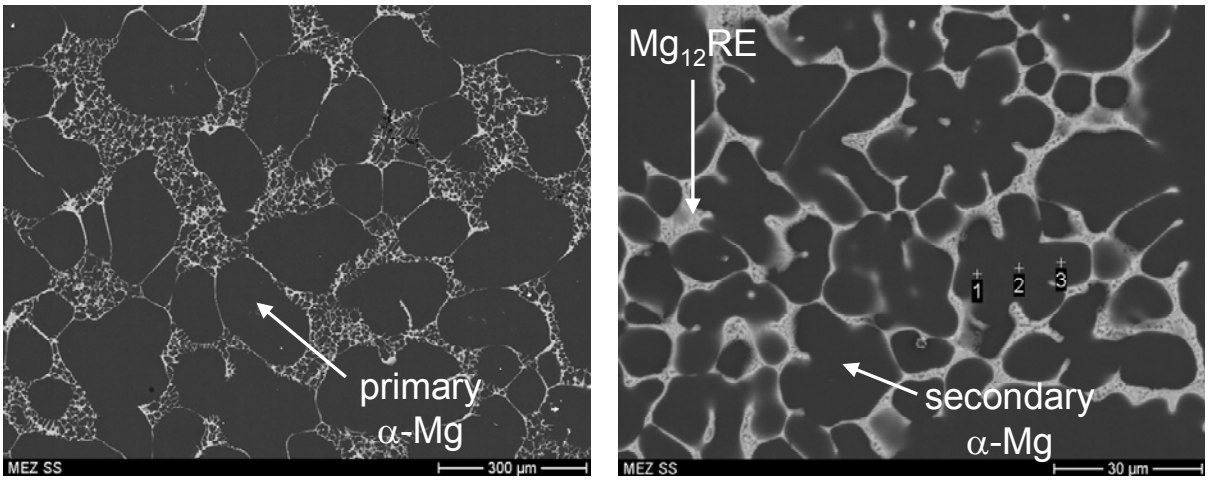

(a) Thixocast MEZ, SEM-BSE (b) Thixocast MEZ, SEM-BSE. Detail

Fig. 29 : Typical microstructure of the thixocast MEZ. Phases identified by SEM-BSE are indicated. Right micrograph is a detail of left micrograph.

Table 7 gives information about the chemical composition of the phases using SEM-EDX. The presence of the Mn_2Zr phases was already indicated in Fig. 26(b). The spectrum of this phase is presented in Fig. 30.

Table 7 : Phases identified in the thixocast MEZ alloy and their composition.

%Mg	%Zn	%Mn	%Zr	%La	%Ce	%Nd	Interpreted phase
67-78	0-4.75			6.7-16.9	9.9-17.8	0-4.2	$(MgZn)_{12}RE$
0.8-7.6		41.5-49.9	47.8-50.8				Mn_2Zr
99.5-100					0-0.5		α-Mg

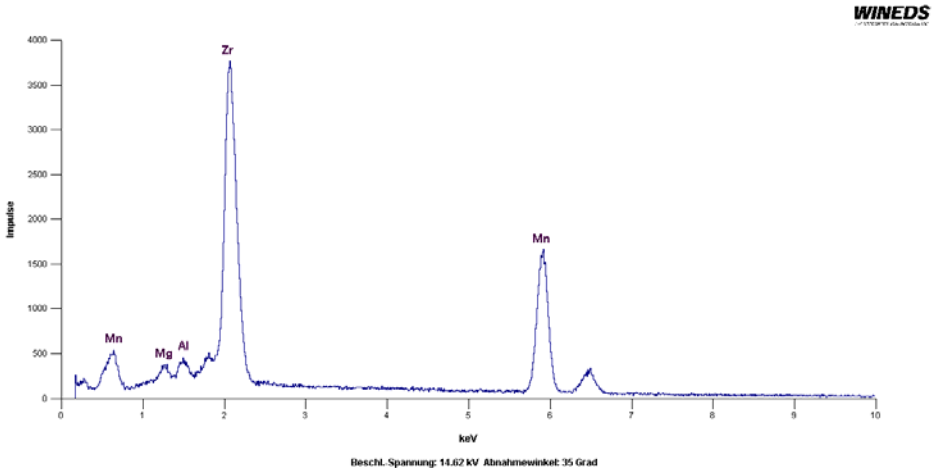

Fig. 30 : Spectrum of the Mn_2Zr phase detected in the thixocast MEZ using SEM-EDX.

The solute concentration within the primary α-Mg particles after SEM-EDX analysis is quite homogeneous. The matrix consists mainly of Mg in solid solution. Ce and La are detected only close to the eutectic boundaries, amounting there up to 1.5 wt. %. The solubility of Ce in Mg (0.52 wt. % at 592°C) [92Nay] is lower than this value, which agrees with a non equilibrium solidification.

5.2 ZECa-System

5.2.1 Characterization of the extruded feedstock material

5.2.1.1 Hardness and chemical composition

The measured hardness of the as-received ZECa material is 54.4 ±5.5 HV10.

The composition of the ZECa alloy in its extruded condition as reported by the supplier is given in Table 8.

Table 8 : Composition of the ZECa extruded bars (in wt. %) as reported by the supplier (MEL), magnesium based.

Ca	Fe	Sr	Zn	Ce	Nd
1.9	0.004	0.08	2.8	0.14	0.18

5.2.1.2 Microstructure

The microstructure of the as-received extruded ZECa material is presented in Fig. 31, transversal and parallel to the extrusion direction. The microstructure of the ZECa alloy shows a fine and equiaxed grain structure, with an average grain size of approx. 11 µm ± 3 µm. The grain size distribution is quite homogeneous in both directions. The presence of the intermetallic phases is better observed in the extrusion direction as discontinuos stringers.

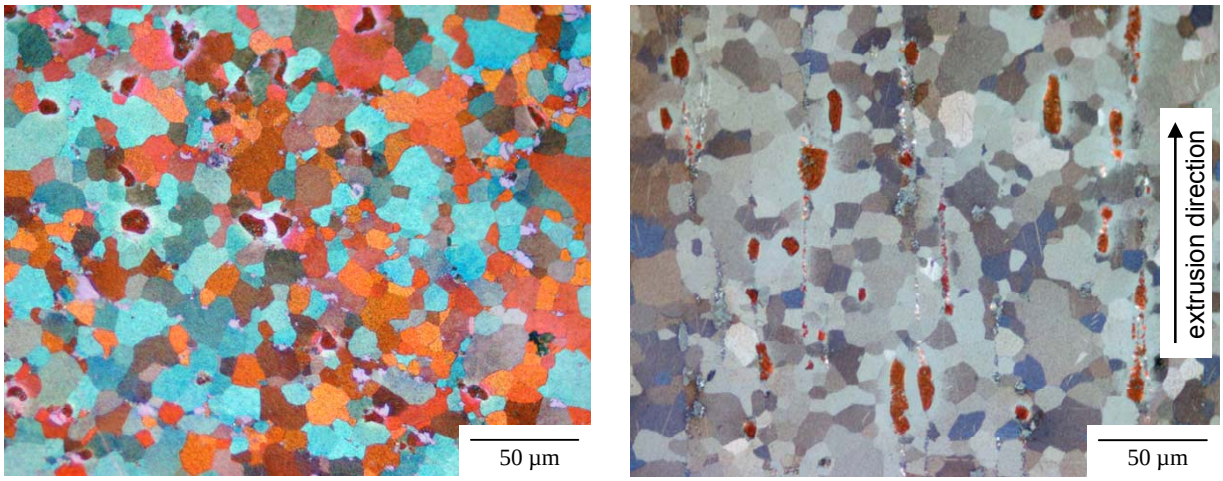

(a) Transversal view of extrusion direction (b) Extrusion direction

Fig. 31 : Microstructure of the extruded ZECa alloy, optical microscopy.

5.2.1.3 Phase identification

The diffraction pattern of the extruded ZECa alloy is presented in Fig. 32. In addition to the α-Mg phase, small but significant reflections from the $Mg_6Zn_3Ca_2$ and Mg_2Ca phases are detected.

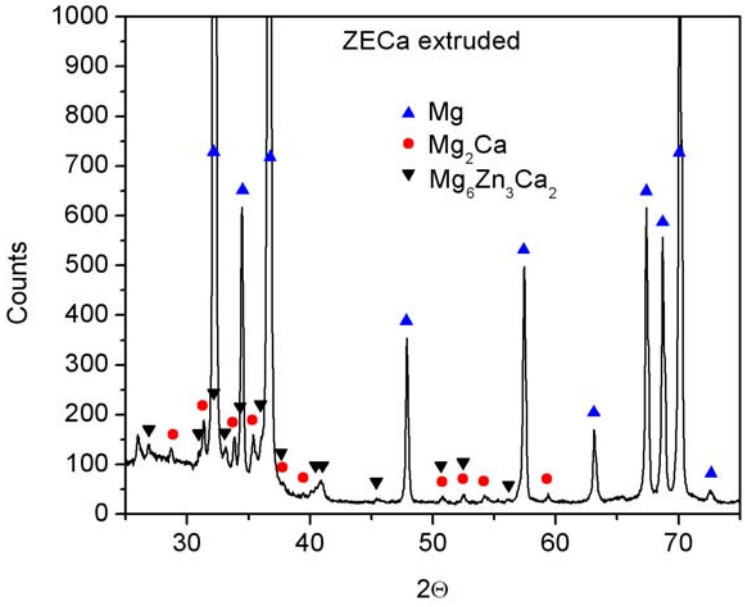

Fig. 32 : X-ray pattern of the ZECa alloy in its extruded condition.

The phases resolved by SEM-BSE in the extruded ZECa alloy are presented in detail in Fig. 33 and Fig. 34. EDX analysis shows that mainly coarse Mg_2Ca and $Mg_6Zn_3Ca_2$ eutectic particles are present, as already detected by X-ray diffraction.

Additionally, Mg-Zn containing particles (presumably Mg_7Zn_3) are found immersed in the ternary $Mg_6Zn_3Ca_2$ phase as well as Si containing particles.

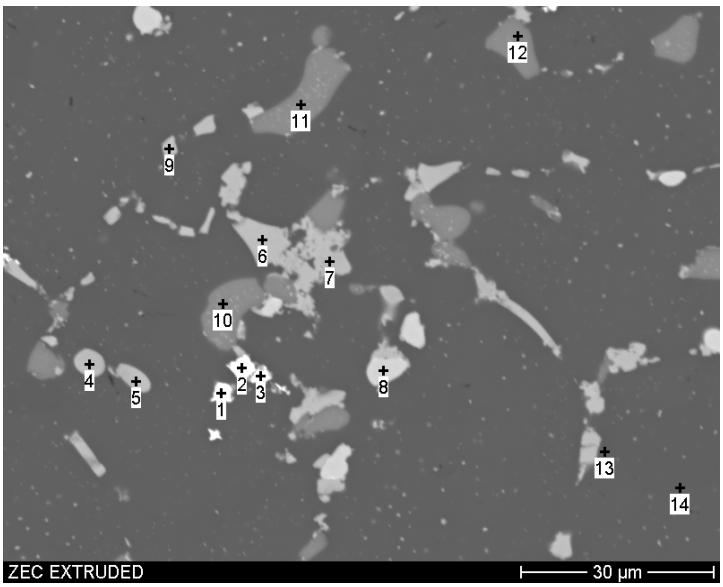

EDX phase identification according to the indicated points on the micrograph:

1-3: Si containing phase(s)

4-7,9: $Mg_6Zn_3Ca_2$

8: Mg-Zn containing phase(s), possibly Mg_7Zn_3

10-12: Mg_2Ca

13-14: α-Mg

Fig. 33 : Extruded ZECa alloy, transversal view of the extrusion direction, SEM-BSE mode.

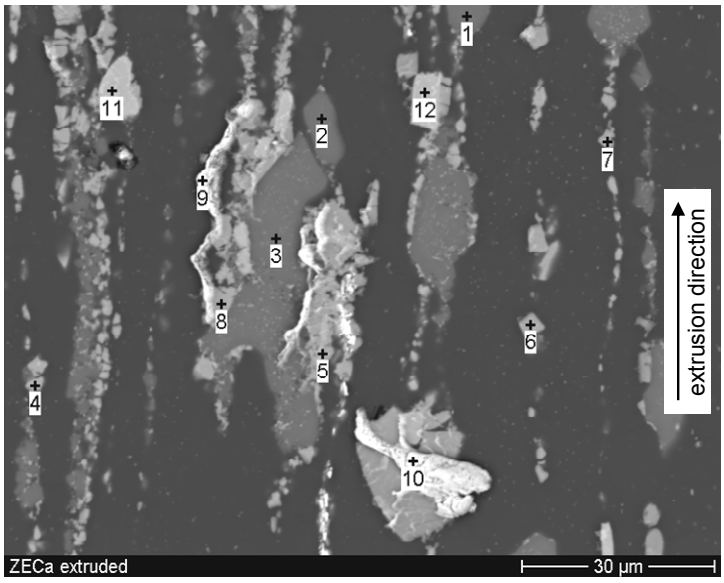

EDX phase identification according to the indicated points on the micrograph:

1-4 : Mg_2Ca

5-8, 11-12 : $Mg_6Zn_3Ca_2$

9-10 : Mg-Zn containing phase(s)

Fig. 34 : Extruded ZECa alloy, longitudinal view of the extrusion direction, SEM-BSE mode.

The intermetallic phases are found at the grain boundary of the globular-shaped α-grains, as seen in Fig. 33. In the extrusion direction, Fig. 34, they are aligned along the deformed grain boundaries. The brittle ternary phase $Mg_6Zn_3Ca_2$ is fractured and aligned in the extrusion direction, while the Mg_2Ca phase is found only elongated.

Fine intermetallic particles are found immersed in the matrix, uniformly and finely dispersed, and aligned in the extrusion direction. These very fine particles are

presumably $Mg_6Zn_3Ca_2$ enriched with rare earths, but due to the nanometric size of these particles, chemical analysis by EDX could not be correctly resolved.

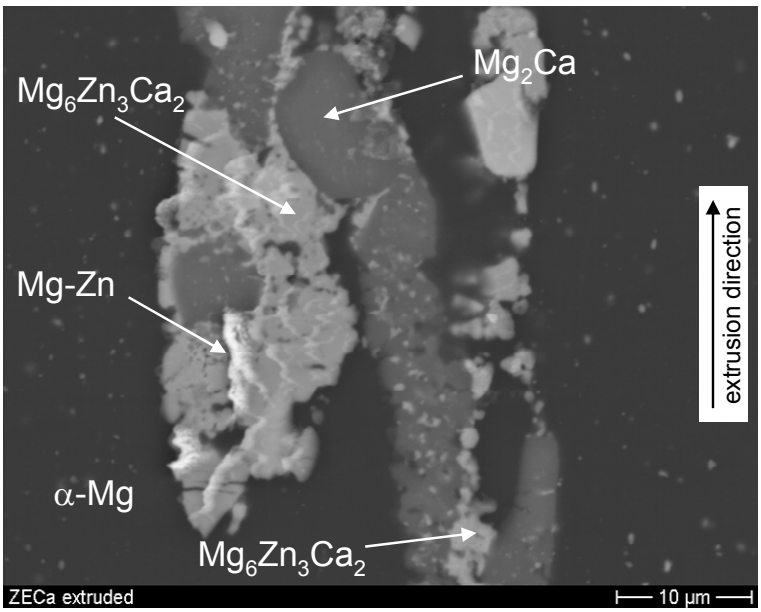

Fig. 35 : Extruded ZECa alloy, longitudinal view of the extrusion direction, SEM-BSE mode at higher magnification.

The eutectic phases formed in the extruded ZECa alloy, detailed in Fig. 35, contained other elements in their crystalline structure, as summarized in the Table 9. The detected Mg-Zn phase has been proposed as Mg_7Zn_3 considering its quantitative analysis by EDX. Si was detected in a Zn-Nd-Si type phase, which was found sparingly distributed in the microstructure.

Table 9 : Phases identified in the extruded ZECa alloy and their composition by EDX (wt. %).

%Mg	%Ca	%Zn	%Sr	%La	%Ce	%Nd	%Si	Interpreted phase
98.7-99.6	0-0.3	0-1.3						α-Mg
49-57	36.4-42	3.3-11	0-1.2					Mg_2Ca
42.7-51	12-17.9	29.6 - 34	0.6-2.6	0-3.3	0-5.3	0-3.7		$Mg_6Zn_3Ca_2$
31-48	2.5-3.2	32-49	1-3.5	3.7-5.9	4.6-9.5	0-3.8		Mg_7Zn_3
14.4-22	4.2-6	9.5-17	0-2	1.8-3.7	12-14	33.4-40	6.7-11.7	Zn-Nd-Si

5.2.2 Characterization of the extruded material during its partial remelting

5.2.2.1 DTA analysis

The identification of the phase changes and respective temperatures taking place during heating in the semi-solid range was carried out by Differential Thermal Analysis (DTA) measurements.

The DTA curves of heating and cooling of the ZECa alloy are shown in Fig. 36. Two small peaks with an onset at 419°C and 455°C can be observed upon heating, corresponding to the melting of secondary phases $Mg_6Zn_3Ca_2$ and Mg_2Ca. The large peak starting at higher temperatures can be attributed to the melting of the α-grains.

The ZECa alloy has a wide heating/solidification temperature range, varying from about 419 to 629°C (lower limit obtained from the heating curve, higher from the cooling curve), resulting in a potential semi-solid range of about 210°C.

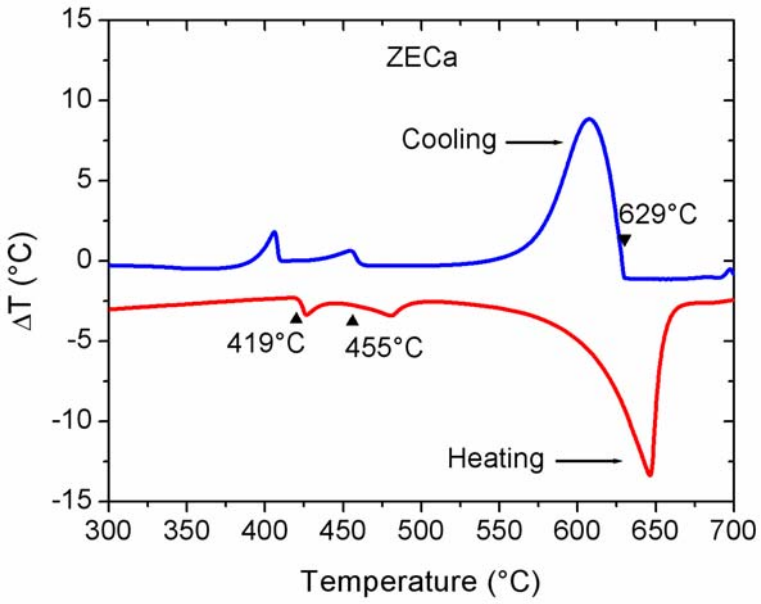

Fig. 36 : Experimental DTA curves for heating and cooling at 10°C/min of the ZECa alloy.

5.2.2.2 Microstructural evolution

After determining the semi-solid temperature (already reported as 419 to 629°C), the reheating temperatures for the ZECa alloy were selected from 400 to 600°C in intervals of 50°C and intervals of 10°C at 600°C and above to observe recrystallization, dissolutions and phase transformations.

Fig. 37 (a+ b) shows that upon heating to 400°C no significant change is observed with respect to the original as-extruded microstructure (compare with Fig. 31 (a) and Fig. 33). The secondary phases do not undergo visible changes. At 450°C, Fig. 37 (c + d), the grain size has increased and the longitudinal microstructure has evolved into polygonal grains and the secondary phases are significantly altered. Corresponding to the first peak of the DTA curve with an onset at 419°C, clear signs of partial melting and subsequent solidification into a typical eutectic microstructure is observed. From the light grey colour of this eutectic it can be deduced that an eutectic of Mg / $Mg_6Zn_3Ca_2$ has formed, while the Mg_2Ca (dark grey) has not yet melted.

Upon heating to 500°C all major secondary phases have melted, Fig. 37 (e + f). The eutectic at the grain boundaries shows that the phases $Mg_6Zn_3Ca_2$ and Mg_2Ca coexist together. The liquefied fraction of the material has increased with respect to heating to 450°C, however, grain boundaries which are not completely wetted still exists thus establishing a solid-solid connection. Additionally, liquefied volumes of the material tend to agglomerate in the core of the α-grains as seen in Fig. 37 (f). Upon heating to 550°C further grain growth is observed, while the melting of secondary phases is not very much affected, Fig. 37 (g + h).

Upon heating to 600°C and to higher temperatures, a significant spherodization of the grain boundaries is observed, as seen in Fig. 38 (a + b). This effect is so strong that small or secondary α-grains are formed in areas out of the spherodized primary α-grain boundaries, Fig. 38 (c to f). These new grains, designated as secondary α-grains, are forming in place of the locations of large meltings, which were seen up to 550°C.

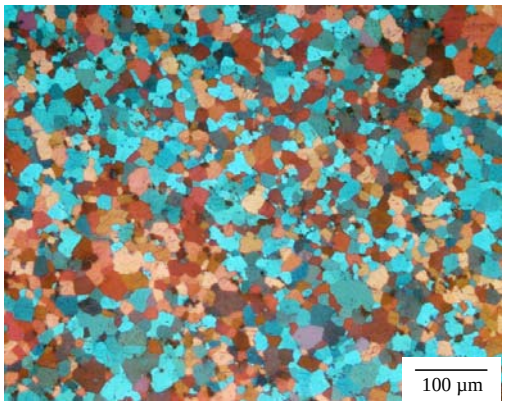

(a) 400°C, transversal direction

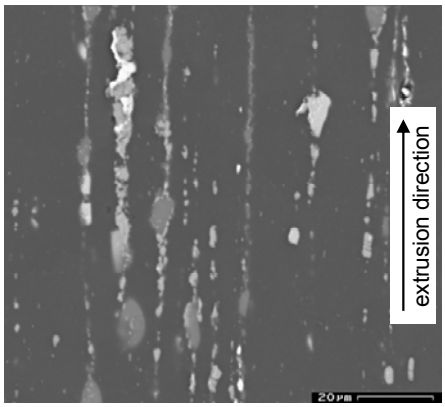

(b) 400°C, extrusion direction

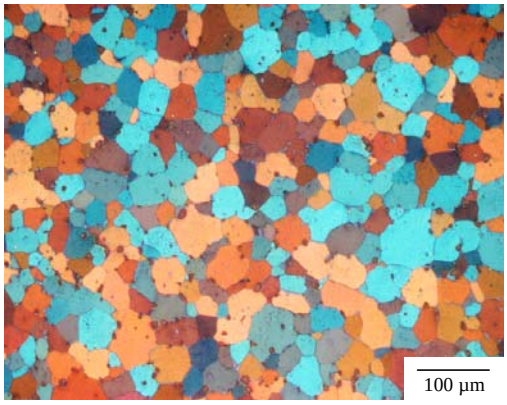

(c) 450°C, transversal direction

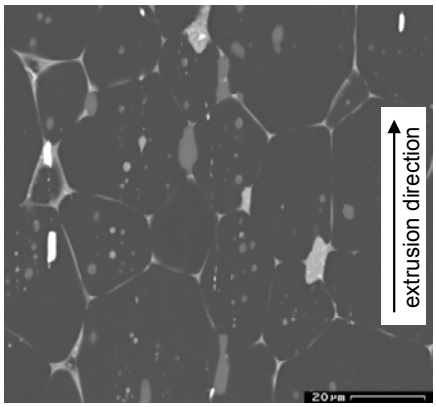

(d) 450°C, extrusion direction

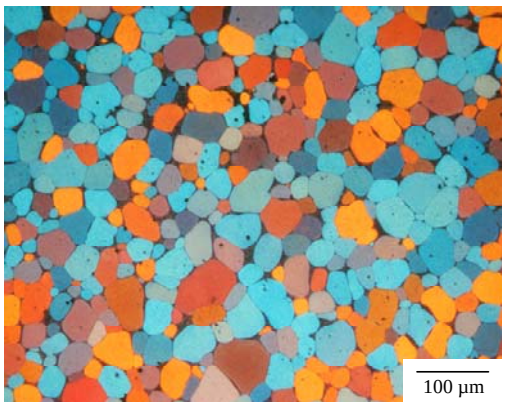

(e) 500°C, transversal direction

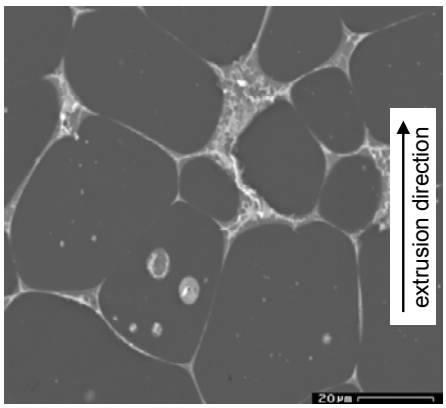

(f) 500°C, extrusion direction

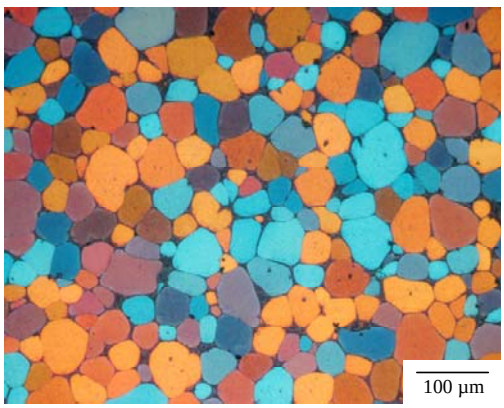

(g) 550°C, transversal direction

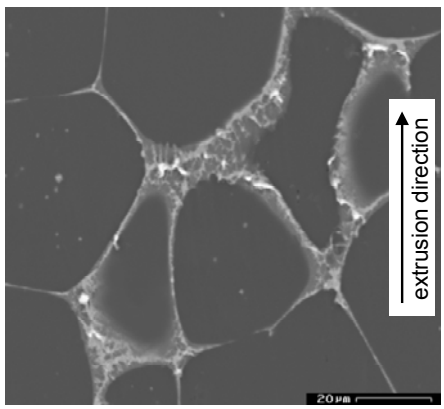

(h) 550°C, extrusion direction

Fig. 37 : Microstructure of the extruded ZECa after reheating at 400, 450, 500 and 550°C as analyzed by optical microscopy (left) and SEM-BSE mode (right).

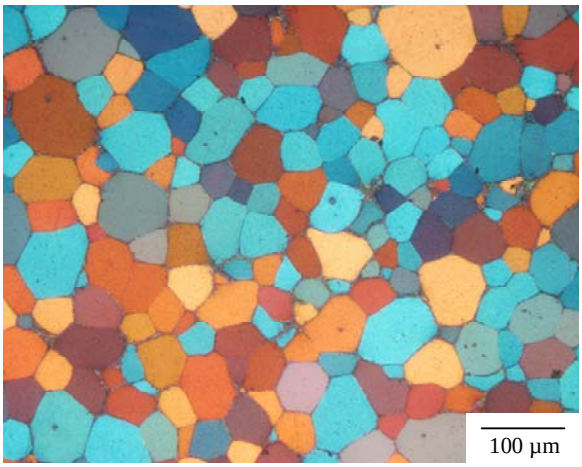

(a) 600°C, transversal direction

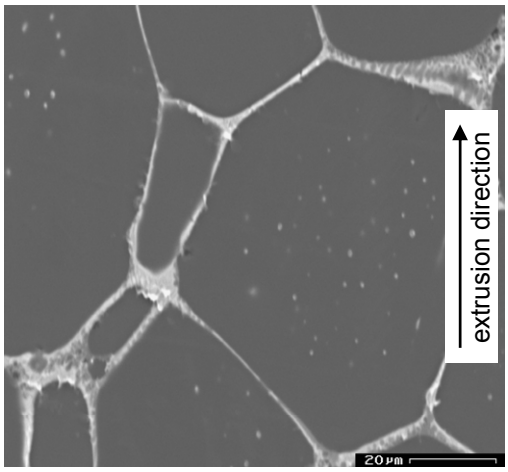

(b) 600°C, extrusion direction

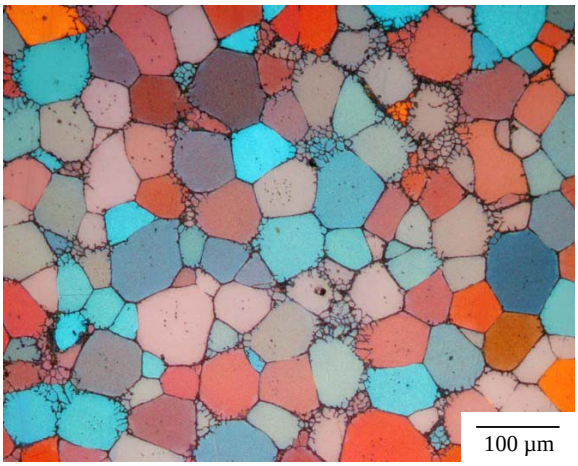

(c) 610°C, transversal direction

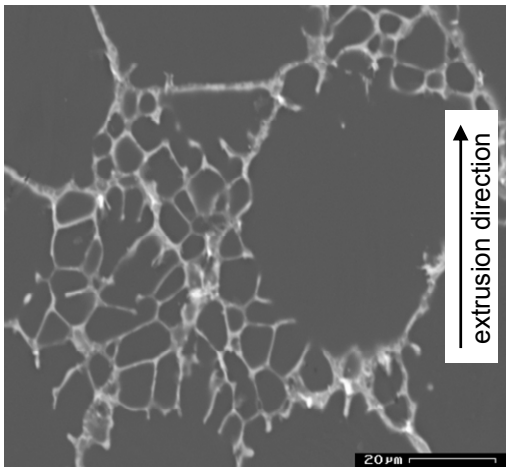

(d) 610°C, extrusion direction

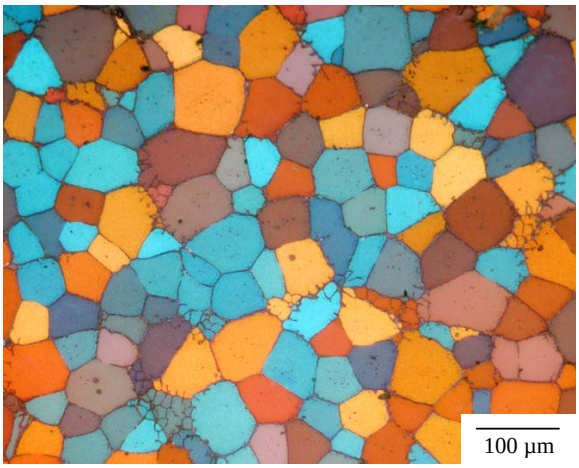

(e) 620°C, transversal direction

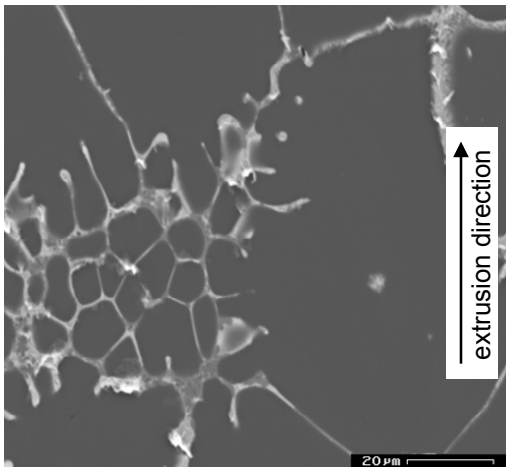

(f) 620°C, extrusion direction

Fig. 38 : Microstructure of the extruded ZECa after reheating at 600°C, 610°C and 620°C as analyzed by optical microscopy (left) and SEM-BSE mode (right).

During isothermal holding a typical coarsening process, i.e. an increase in average particle size and spheroidization behaviour of the α-grains, is observed already after 2 min. (Fig. 39 (a + b)). As the isothermal time is prolonged, the formation of secondary α-phases at the grain boundaries is significantly increased, Fig. 39 (c + d).

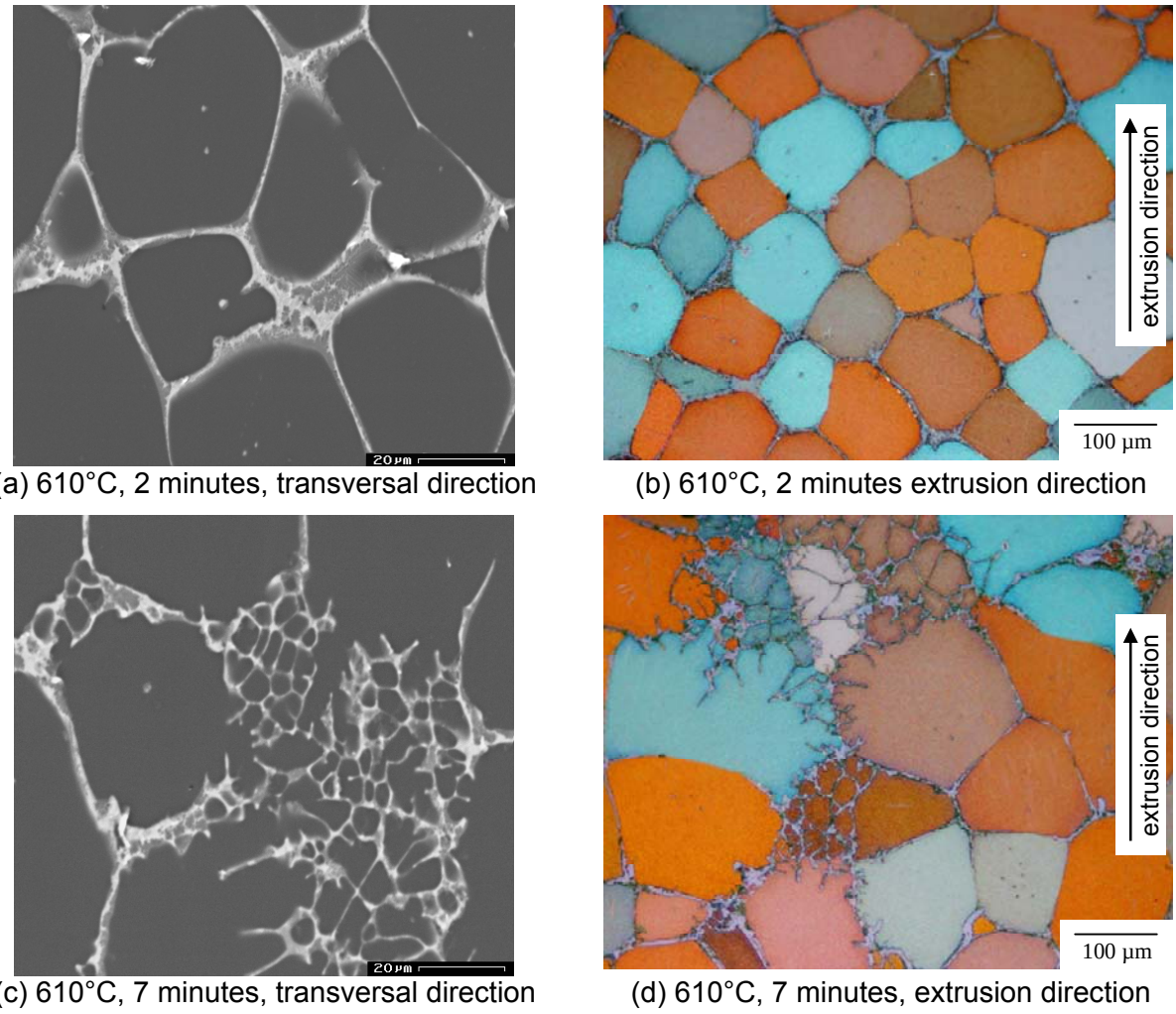

(a) 610°C, 2 minutes, transversal direction (b) 610°C, 2 minutes extrusion direction

(c) 610°C, 7 minutes, transversal direction (d) 610°C, 7 minutes, extrusion direction

Fig. 39 : Microstructure of the extruded ZECa after reheating at different times at 610°C as analyzed by by SEM (left) and optical microscopy (right).

5.2.2.3 Grain size evolution

Fig. 40 shows the grain growth as determined metallographically. In the extruded ZECa alloy, grain growth increases continuously with the temperature from 350°C to 620°C. This results in a lower grain growth of the ZECa alloy at higher temperatures. This lower grain size growth of the ZECa alloy has to be regarded on the background of the small grains forming on the grain boundaries at high temperatures resulting in a more bimodal distribution of grain sizes as well as on the early melting of the secondary phases.

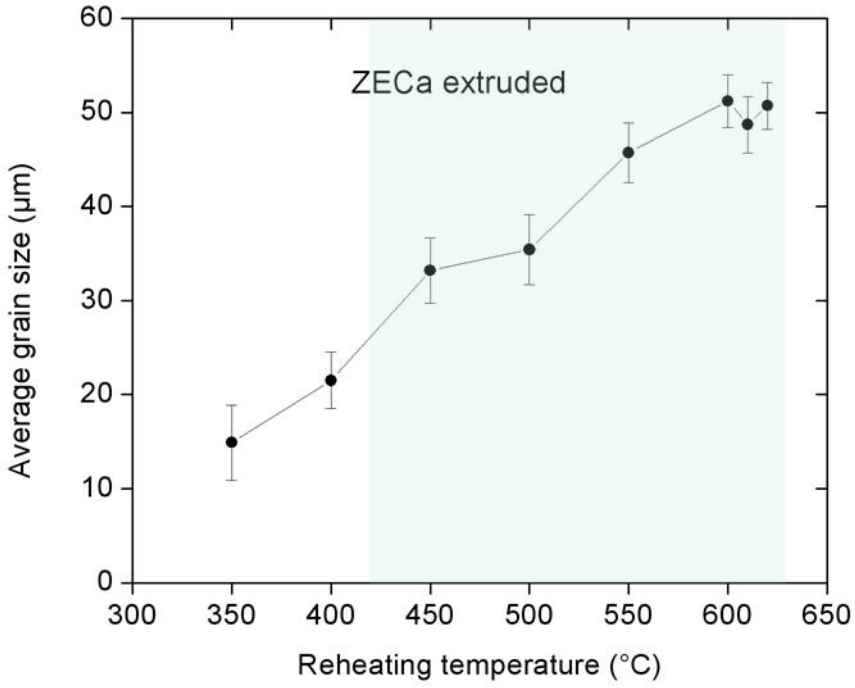

Fig. 40 : Evolution of the grain size of α-Mg in the extruded ZECa material after heating during five minutes at different temperatures. The shadow area represents the melting area of the eutectics.

5.2.3 Characterization of the thixocast material

5.2.3.1 Chemical composition

The chemical composition of the ZECa alloy after the thixocasting process was determined by means of the inductively coupled plasma technique (ICP). The results of the analysis are shown in Table 10.

Table 10 : Chemical composition of the processed ZECa material (in wt. %) measured by ICP, magnesium based.

Al	Ca	Fe	Ni	Si	Sr	Zn	Ce	La	Nd	Pr
0.06	3.5	0.009	0.002	0.03	0.1	3.6	0.2	0.1	0.2	0.2

5.2.3.2 Microstructure at lower magnification

The microstructural overview shows that the ZECa alloy has a significantly fine microstructure. Despite the lower casting temperature, the microstructure shows only minor pores.

Fig. 41 and Fig. 42 show overviews of the complete microstructure of the as-cast ZECa material at different thicknesses. Two representative casting samples were chosen to show the variability of the resulting microstructure.

As can be seen on the 14 and 10 mm steps, Fig. 41, an almost imperceptible decrease of the grain size (which is around 100 µm) is observed in homogeneous samples from the core to the rim. In heterogeneous samples, the largest grains in the core can be of the order of 150-250 µm and possess a rosette-like form.

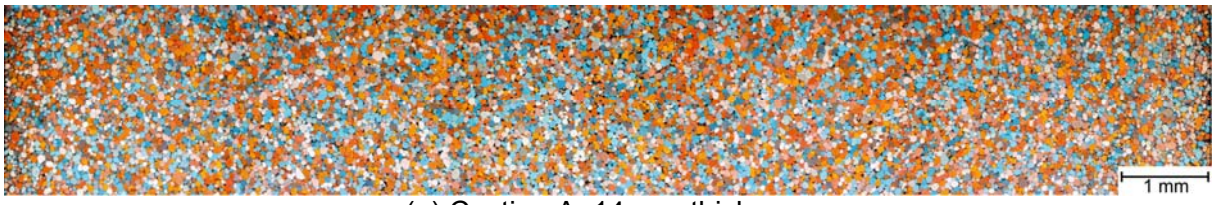

(a) Casting A, 14 mm thickness

(b) Casting B, 14 mm thickness

(c) Casting A, 10 mm thickness

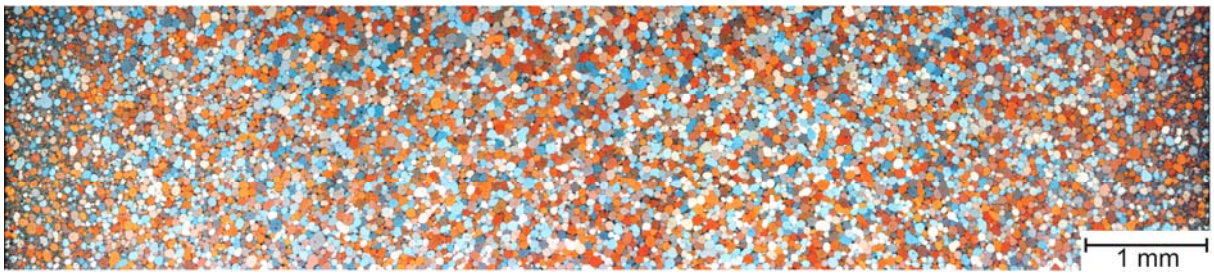

(d) Casting B, 10 mm thickness

Fig. 41 : Complete cross section of two representative casting samples of MEZ, 14 and 10 mm steps (rims are at both extremes, to the left and to the right).

The α-grains in the core of the samples show the typical spherodized grain boundaries observed when the material was reheated in its extruded condition to higher temperatures or exposed for larger times to high temperature. The eutectic

phases formed at the grain boundaries of the α-grains are fine and their amount increases at the very extreme of the rim. Small or secondary α-grains are not well detected at these magnifications.

The same observations concerning size and shape of the α-Mg grains apply for the 6 and 2 mm thickness, Fig. 42. In general, the grain size decreases slightly with the step thickness of the sample, corresponding to the increasing cooling rate of the sample while decreasing step thickness. For the 14 mm thickness, the estimated grain size is of the order of 65 µm, while for the 2 mm thickness, the grain size is of about 50 µm.

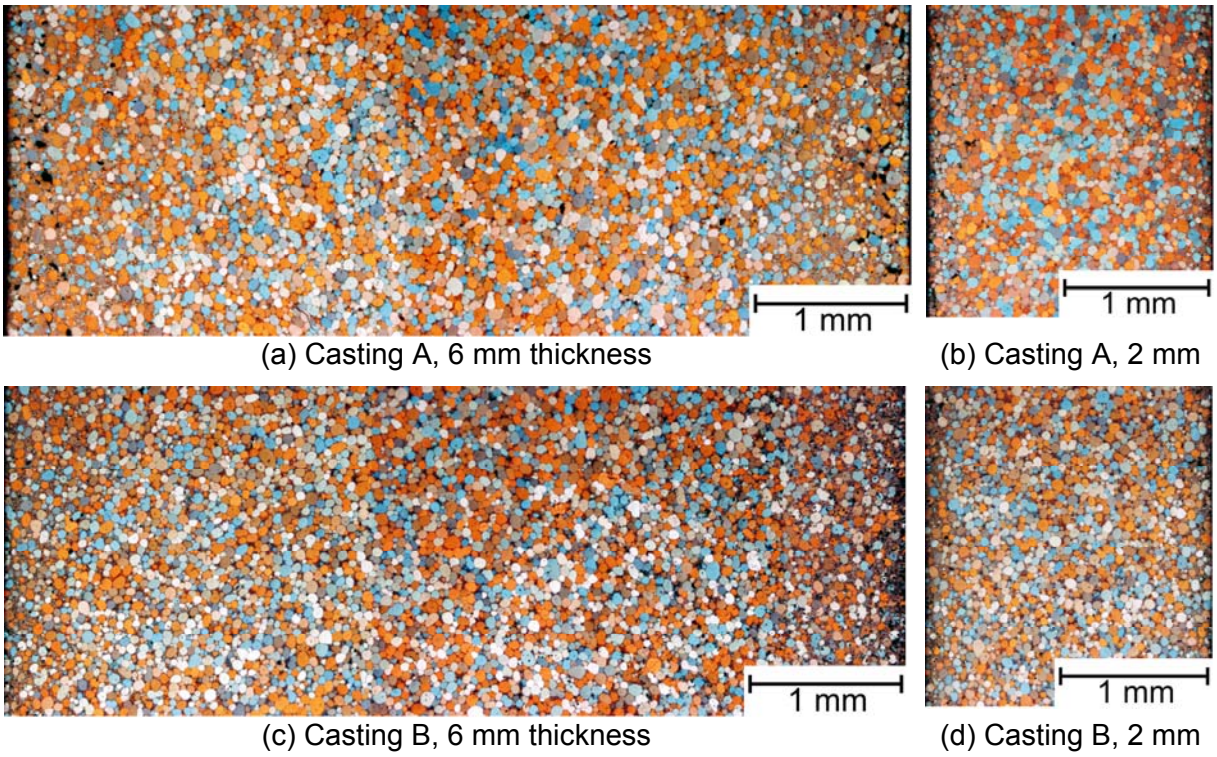

(a) Casting A, 6 mm thickness (b) Casting A, 2 mm

(c) Casting B, 6 mm thickness (d) Casting B, 2 mm

Fig. 42 : Complete cross section of two representative casting samples of ZECa, 6 mm and 2 mm step (rims are at both extremes of every micrograph, to the left and to the right).

5.2.3.3 Microstructure

A closer view of the microstructure of the thixocast ZECa alloy, Fig. 43, reveals the typical features already observed in the partial melting experiments in the previous chapter (5.2.2.2). The microstructure of the material consists of primary crystals (α-Mg phase) of typically 50-60 µm, spherodized grain boundaries and volumes of small grains of typically 10 µm formed by eutectic phases and secondary α-Mg grains, Fig. 43 (a + b). The eutectic network consists of two phases, appearing dark grey and bright in Fig. 43 (c). The presence of a very bright phase (Fig. 43 (d)) containing Fe

and/or Si together with Nd and Zn, is occasional and corresponds to agglomeration of impurities in the material after casting.

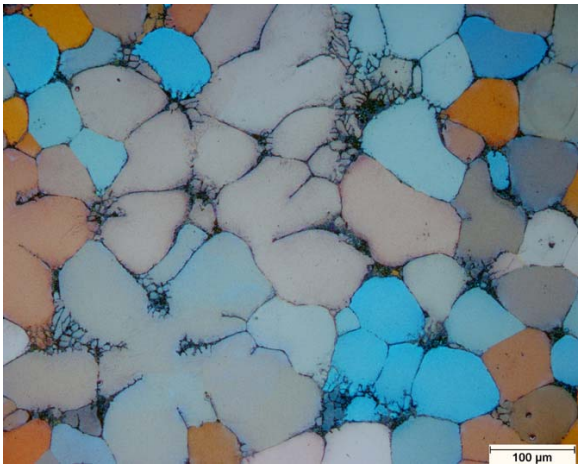

(a) Optical microscopy

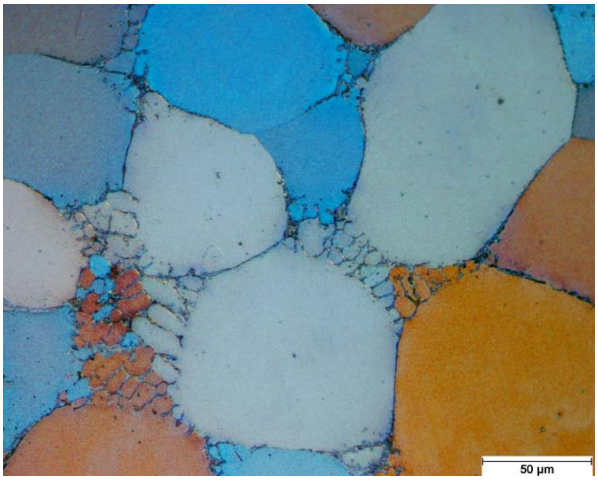

(b) Detail, optical microscopy

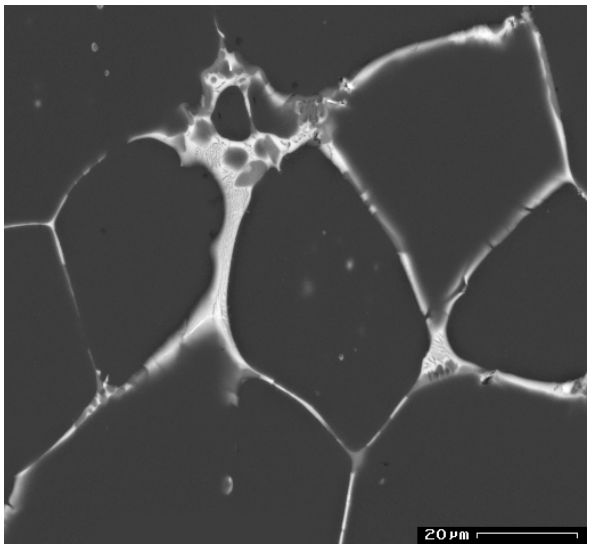

(c) SEM-BSE

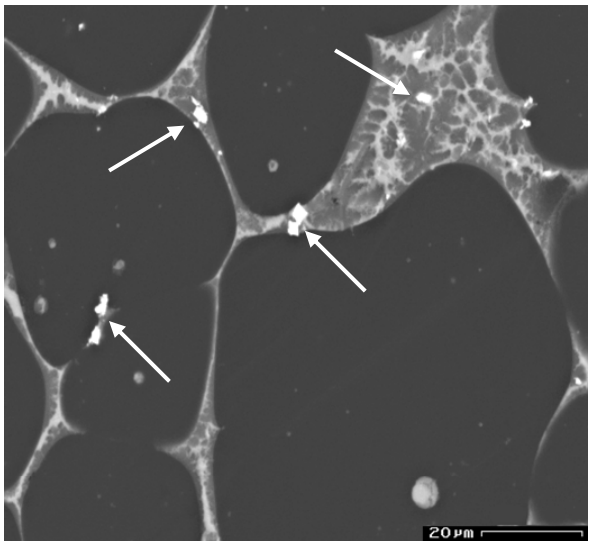

(d) Impurities of MgZnNdFeSi, SEM-BSE

Fig. 43 : Typical microstructure of the thixocast ZECa in the core of a step.

The distribution of the eutectic phases related to its position in the cast plates can be observed in Fig. 44. At the rim, the small grains formed by the eutectic phase and the secondary α-grains wet completely the primary α-Mg grains, which are globular in shape. In the core, the eutectic phases form thin boundaries around the primary α-grains, and eventually also some agglomerations. The amount of small grains is significantly higher at the rim than at the core.

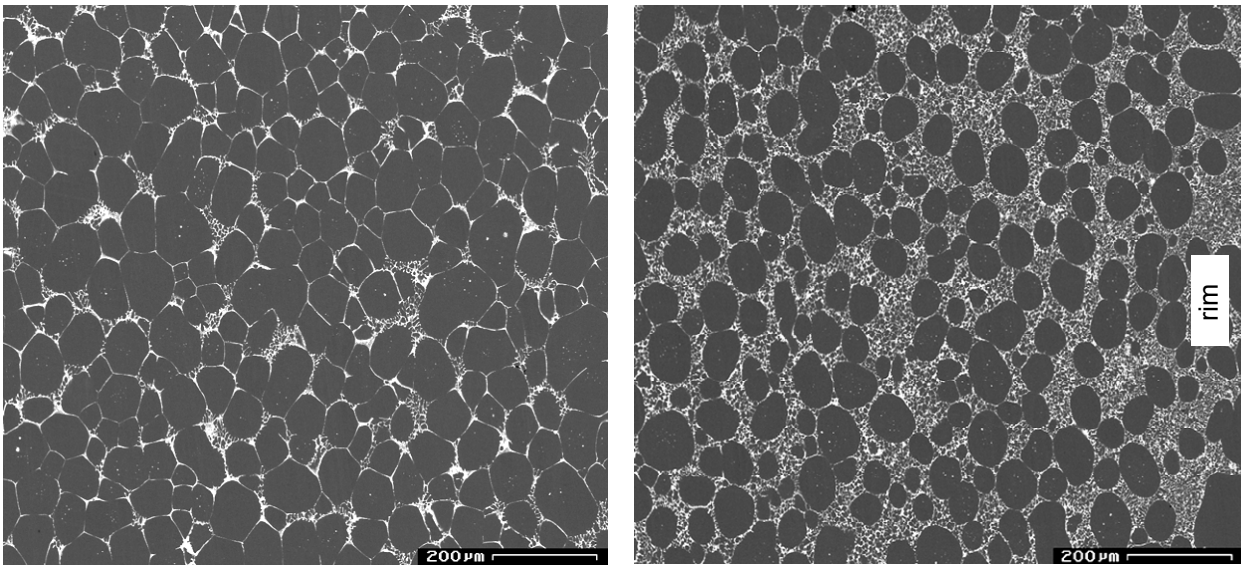

(a) Core (b) Rim

Fig. 44 : Scanning electron microscopy of a cross section of the extruded ZECa alloy after thixocasting at different locations of the stepped sample.

5.2.3.4 Phase identification

The x-ray diffraction analysis in Fig. 45 shows that, as in the extruded alloy, mainly the intermetallic phases Mg_2Ca as well as $Mg_6Zn_3Ca_2$ can be found.

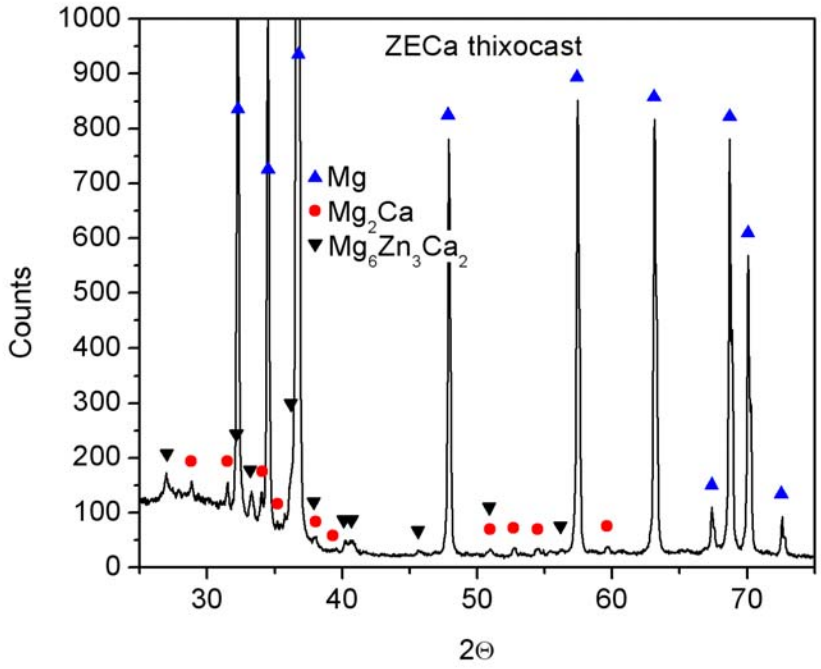

Fig. 45 : X-ray pattern of the ZECa alloy in its thixocast condition.

The phase identification is shown in the SEM micrographs of Fig. 46. The two expected eutectics can be clearly distinguished thanks to the dark-bright contrast of

the BSE mode, Fig. 46 (a + b). The ternary $Mg_6Ca_2Zn_3$ phase (appearing bright) can also be observed as partially divorced eutectic at the α-Mg grain boundaries, Fig. 46 (c + d). Only very little eutectic phase can be discerned within the grains as entrapped liquid, Fig. 46 (b).

The binary Mg-Zn phase detected in the extruded condition and proposed as Mg_7Zn_3 is not detected in the thixocast condition. Instead of the Mg_7Zn_3, another binary Mg-Zn phase, which appears together with the ternary phase, is formed in the thixocast condition but it is scarcely seen in the microstructure. It contains some Si (up to 0.3 wt. %) and may contain some other impurities like Fe (up to 0.6 wt. %). The Zn-Nd-Si detected also in the extruded condition has disappeared after semi-solid processing, but the Si has probably migrated to the already mentioned binary Mg-Zn phase.

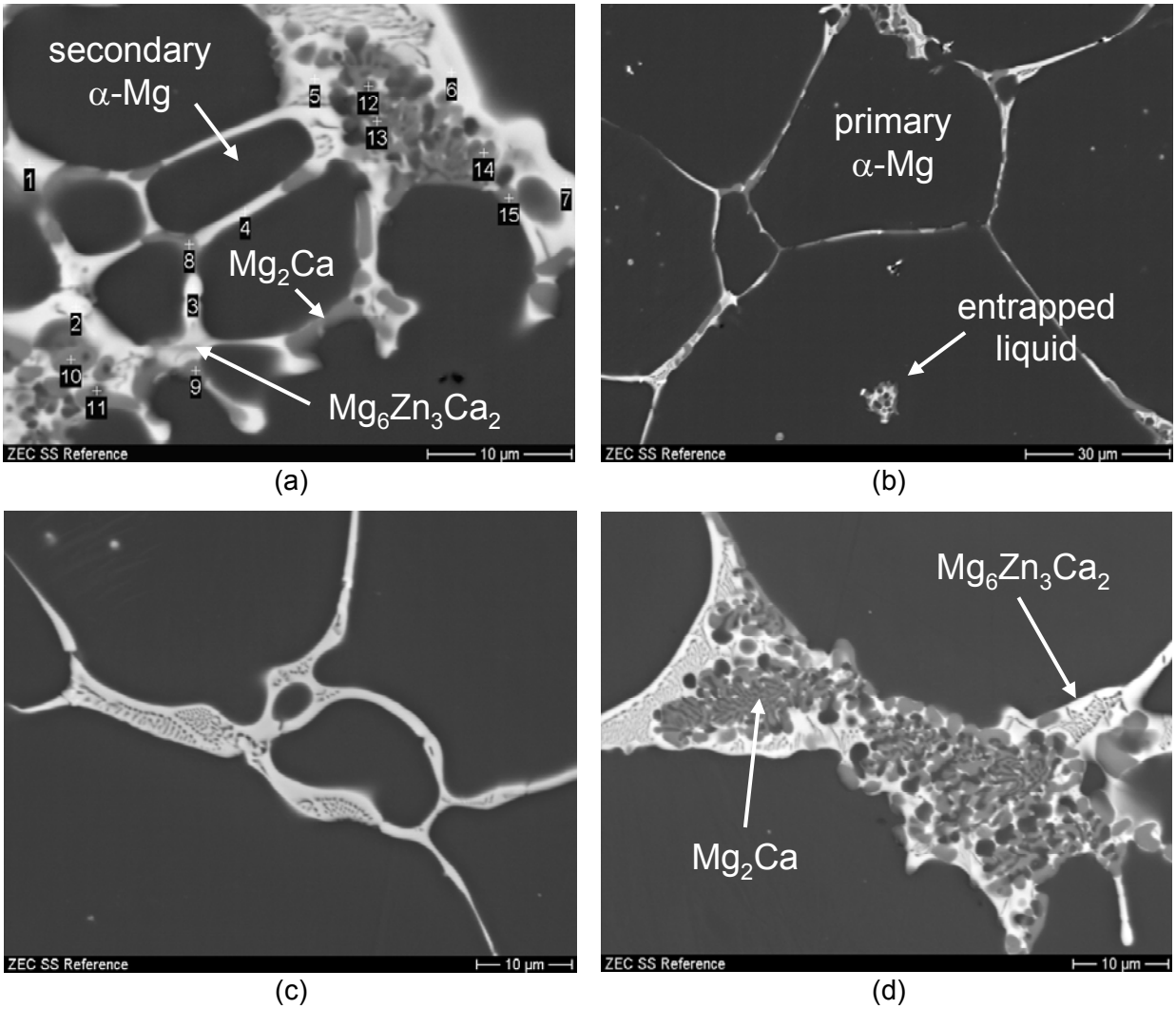

Fig. 46 : Scanning electron microscopy of cross sections of the extruded ZECa alloy after thixocasting.

The chemical compositions of the phases detected by SEM-EDX in the thixocast ZECa alloy are presented in Table 11.

Table 11 : Phases identified in the semi-solid ZECa alloy and their composition.

%Mg	%Ca	%Zn	%Si	%Sr	%La	%Ce	%Nd	Interpreted phase
51.3-70.1	18.3-28.5	5.6-18.7		0-1.2				Mg_2Ca
35.3-50.8	6.4-14.7	31.2-41		0-1.2	0-1.2	0.6-2.1	0-1.9	$Mg_6Zn_3Ca_2$
4.1-11	2.8-3.1	81.3-88	0.1-0.3				0.7	Mg_2Zn_3
97.5-99.6	0.2-0.5	1.1-1.8						α-Mg

The solute concentration within the primary α-Mg particles after SEM-EDX analysis has shown to be relatively homogeneous. While the amount of Ca is close to zero in the grain, the amount of Zn is in the range of 0.5-0.8, which agrees with the higher solubility of Zn in Mg (6.2 wt. % at 340°C) [92Cla] compared with the lower solubility of Ca in Mg (1.34 wt. % at 516°C) [92Nay].

6 MECHANICAL BEHAVIOUR OF THE THIXOCAST MATERIAL

6.1 MEZ-System

6.1.1 Mechanical properties at room temperature

6.1.1.1 Hardness tests, tension and compression tests

The hardness value of the thixocast MEZ material was measured as 50.2 ±2.0 HV10.

Representative engineering stress-strain curves for the thixocast MEZ alloy at room temperature in tension and compression are displayed in Fig. 47. The MEZ alloy shows an average elastic range up to about 75 MPa in tension. After this range, a smooth transition to the plastic mode can be observed. The same trend is observed for the compressional load. As expected in magnesium alloys, the failure in compression occurs at much higher degrees of deformation, leading to significantly higher ultimate strength in compression as compared to tension. Although the values of tensile and compressive yield strength are almost the same, the ultimate compressive strength is almost twice the value of the ultimate tensile strength. The deformation in compression is almost three times higher than in tension. The tensile curve shows two deformation stages, while the compressive curve shows three.

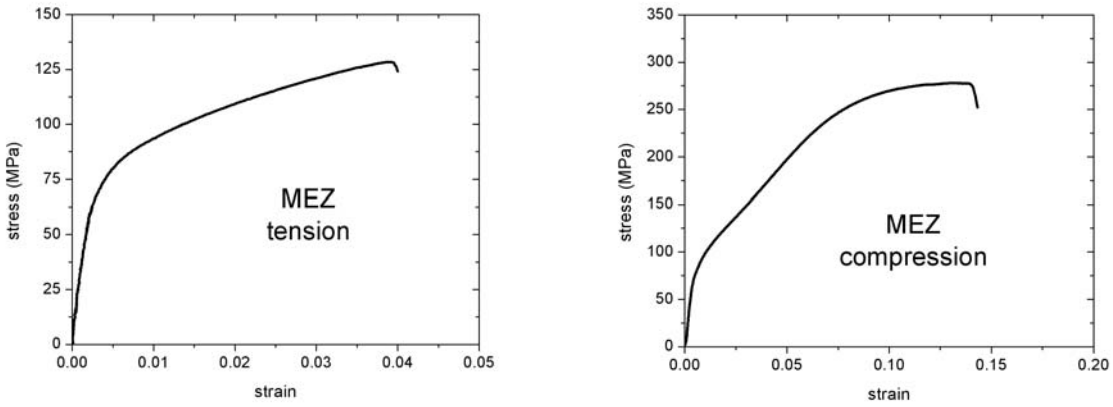

(a) (b)

Fig. 47 : Representative stress-strain curves of the thixocast MEZ alloy in tension and compression.

The flow curve of many metals in the region of uniform plastic deformation can be expressed by the power curve relation:

$\sigma = K \varepsilon^{n}$ (Eq. 3)

where σ is the true stress, K is the strength coefficient, ε is the true plastic strain and n is the strain hardening exponent. Plotting the log-log true-stress versus true-strain curves of the tension tests allows the determination of the strain hardening exponent, n, which is a measure of the increase in hardness and strength in the material caused by plastic deformation [88Die].

The tensile and compressive properties of the thixocast MEZ alloy are summarised in Table 12. The values represent the average of 6-8 tests at room temperature.

Table 12 : Tensile and compressive properties of the thixocast MEZ alloy at room temperature.

MEZ	Tension	Compression
0.2% TYS (MPa)	75.5 ± 10	
UTS (MPa)	124.7 ± 13	
% elongation	3.7 ± 1	
0.2% CYS (MPa)		75.5 ± 6.8
UCS (MPa)		244.8 ± 4.3
% compression		12.97 ± 2.1
n (strain hardening exponent)	0.21 ± 0.02	
K (strength coefficient), MPa	264 ± 24	

6.1.1.2 Microstructural analysis of deformed samples

The microstructure of the thixocast MEZ alloy after tensile deformation at room temperature shows a high amount of bands with different crystallographic orientation within the original grains, which indicate substantial twinning, Fig. 48. Different orientations of these bands within the same grain indicate that also secondary twinning has been activated.

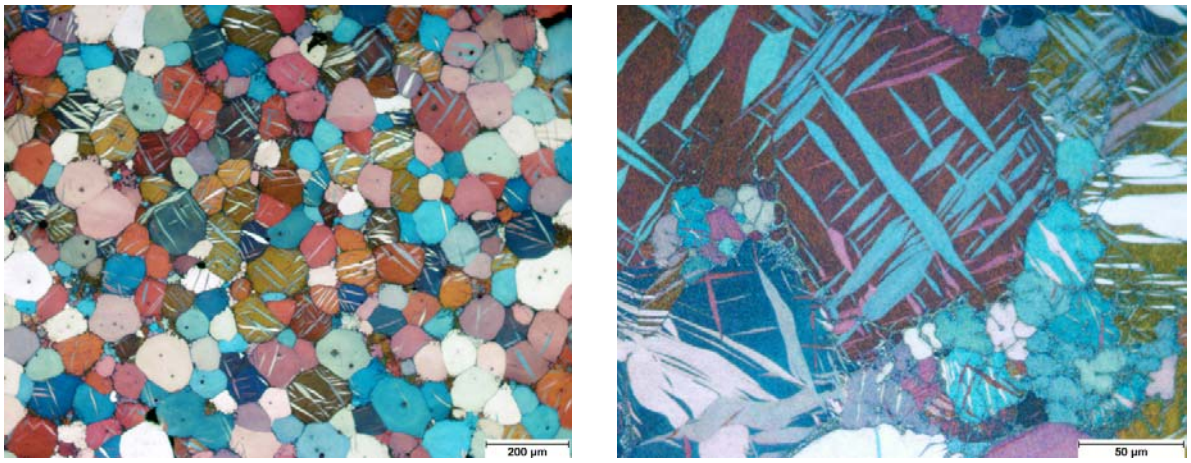

(a) (b)

Fig. 48 : Microstructure of the MEZ alloy after tension tests showing primary and secondary twinning.

The fracture surfaces of the MEZ tensile samples at room temperature shown in Fig. 49 exhibit the typical features observed when the eutectic is fractured. Additionally, small α-grains embedded in the eutectic are found, where the fracture propagates transgranular, showing large shear bands, as seen in Fig. 49 (b). The fracture type can be summarized as ductile-brittle. Partly larger cleavage plains also indicate a rather brittle behaviour as depicted in Fig. 49 (a).

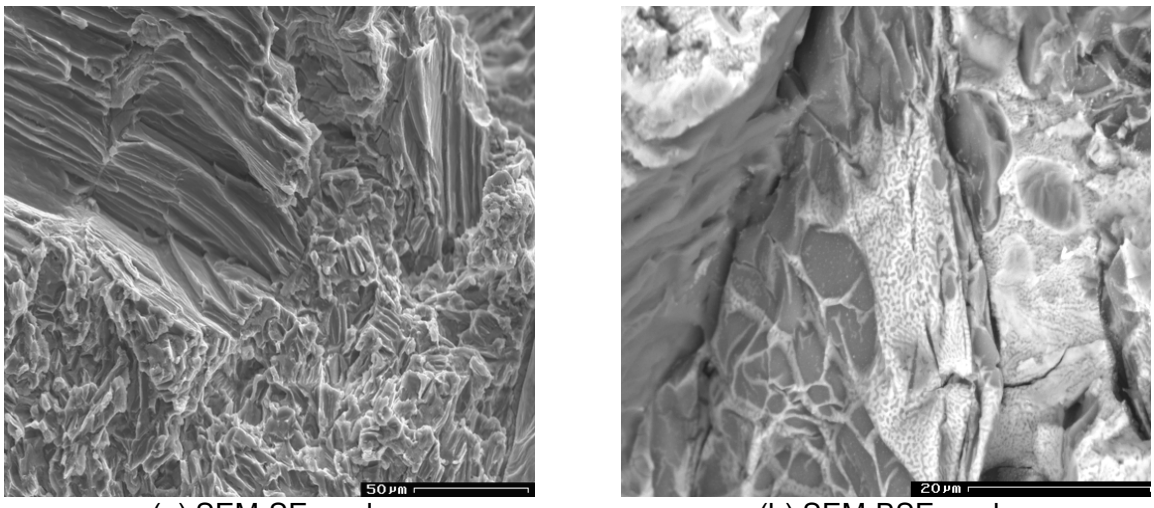

(a) SEM-SE mode (b) SEM-BSE mode

Fig. 49 : Fracture surface of the thixocast MEZ alloy tested at room temperature in tension, SEM.

Fig. 50 shows the microstructure of the MEZ alloy after compression at room temperature. In accordance to the high strain achieved in compression (~13%), the originally globular grains are elongated. Primary and secondary twinning is present; particularly in areas distant from the fractured surface, Fig. 50 (a). The formation of

shear bands, indicated by the typical wavy form, is observed additionally to the massive twinning in areas closer to the fractured surface. Moreover, substantial dynamical recrystallization is also observed covering several α-grains, Fig. 50.

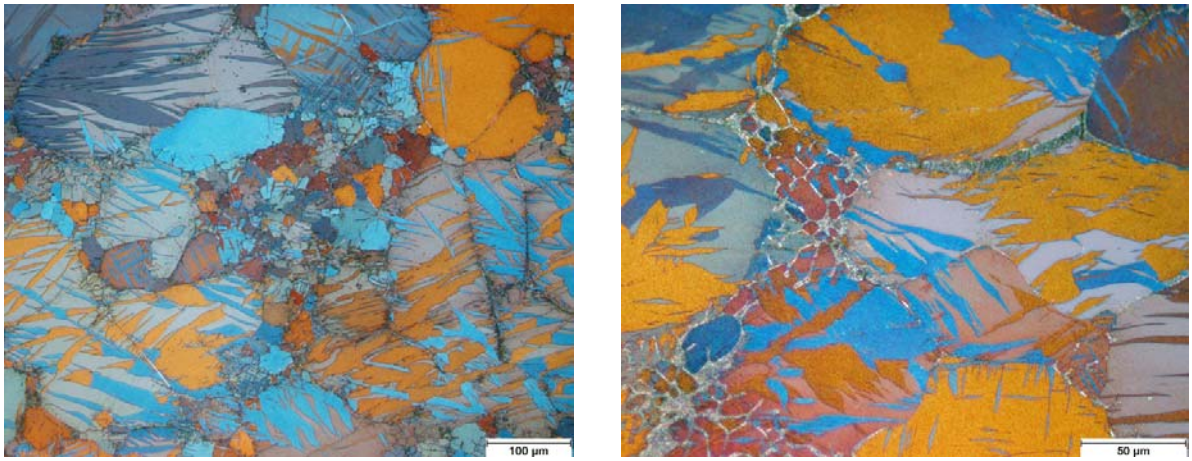

(a) away to fracture (b) close to fracture, recrystallization

Fig. 50 : Thixocast MEZ alloy after compression tests, OM.

In Fig. 51 the microstructure of the deformed material in compression tests is shown using SEM-BSE. It can be seen that the fracture is initiated at the intermetallic phase $Mg_{12}RE$ (appearing bright) and then propagates into the magnesium grains (appearing dark-grey), Fig. 51 (a). The fracture growths preferentially in directions across the seams of intermetallic phase at the grain boundaries and intragranularly, Fig. 51 (b). No crack propagation is observed along the grain boundaries.

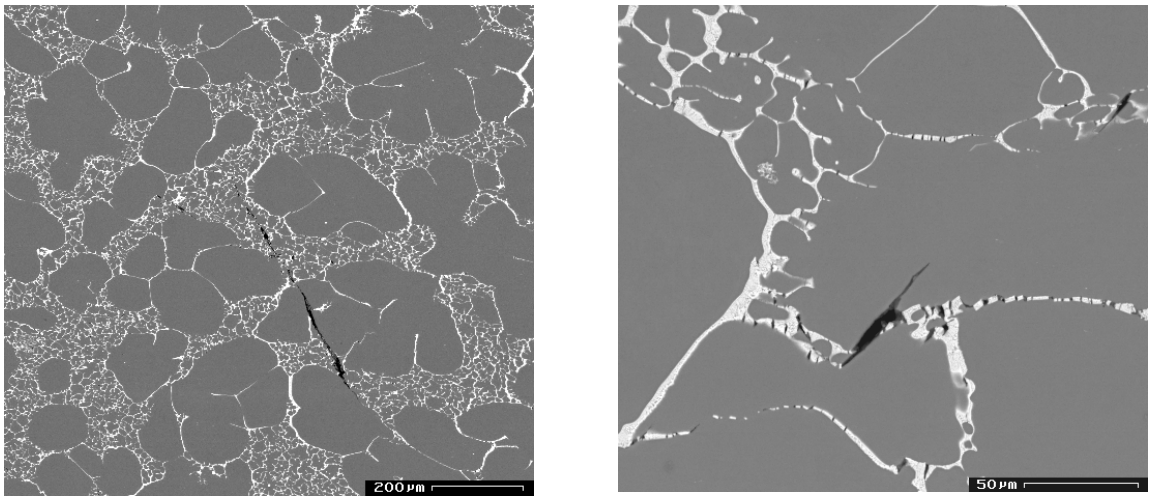

(a) (b)

Fig. 51 : SEM section of thixocast MEZ alloy after compression tests.

Fig. 52 shows the fracture surface of the MEZ alloy after compression. The fracture propagates mainly transgranular, showing only little sections of the intermetallic phase on the fracture surface, Fig. 52 (a). Shear lips can be observed throughout the α-grains, resulting from transgranular shearing in the alloy. A close-up view indicates cross slip lines, arising in a slant angle to the main shear direction, Fig. 52 (b).

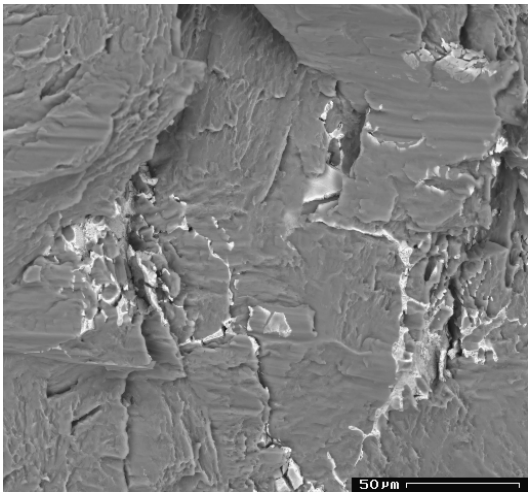

(a)

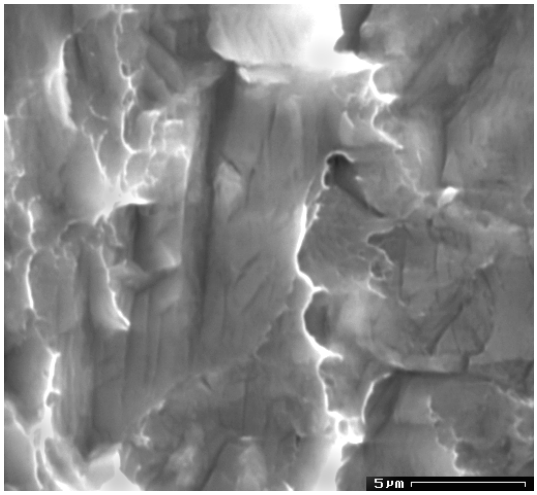

(b) Cross slip lines

Fig. 52 : Fractured surface after compression in thixocast MEZ alloy, SEM-SE.

6.1.2 Microstructural stability with temperature

6.1.2.1 Hardness evolution after aging

Fig. 53 shows the hardness response of the thixocast MEZ alloy after different annealing times and different temperatures. After 50h of thermal exposure, the hardness increases only at 150°C because of an aging response while at temperatures above 150°C the hardness drops significantly, probably as a result of overaging. Up to 150°C the hardness remains at a constant level after longer times of exposure. However, at higher temperatures a second drop in hardness can be detected at 200h. This effect is less pronounced at 175°C, where hardness varies between 44 and 46 HV10 after the first 25h.

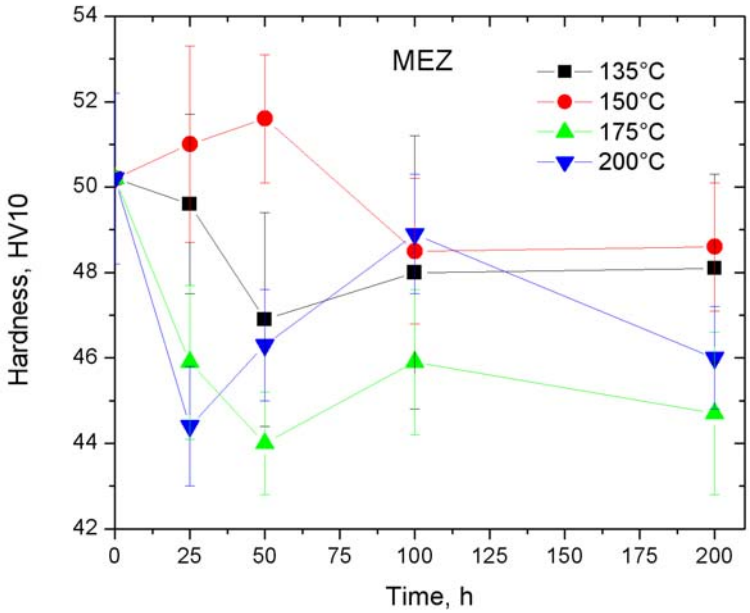

Fig. 53 : Hardness evolution of the thixocast MEZ alloy at the exposure to elevated temperatures (initial hardness was 50 HV10).

6.1.2.2 Microstructural evolution after aging

Fig. 54 shows the microstructural evolution of the MEZ alloy after 200h of exposure at different temperatures. At 135°C, the microstructure of the alloy remains unaffected; precipitation could not be resolved by SEM. At 150°C, some secondary precipitation can be detected inside the α-grains. At 175°C and above, microstructural deterioration takes place. The secondary precipitation thickens and even gets visible at sub-grain boundaries, which can be seen as small white lines within the α-grains.

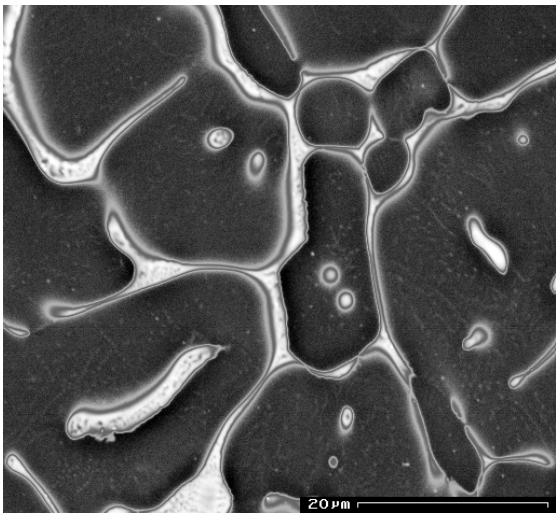

(a) 150°C during 200h

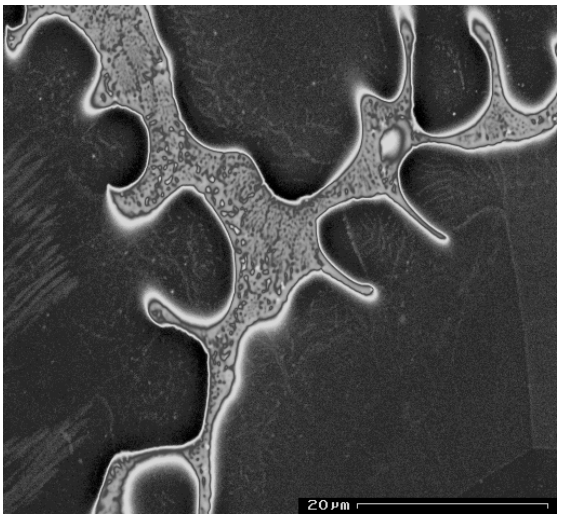

(b) 175°C during 200h

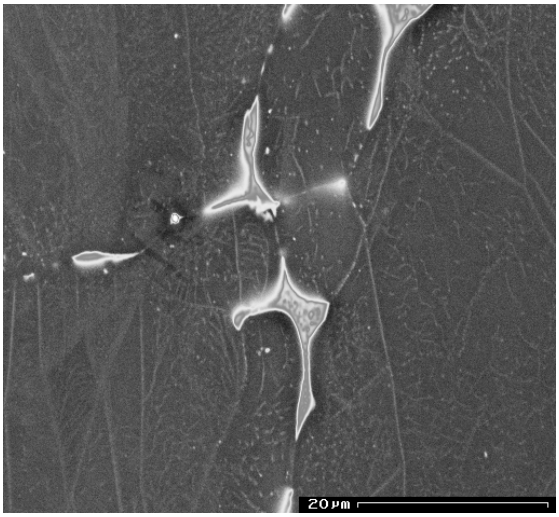

(c) 200°C during 200h

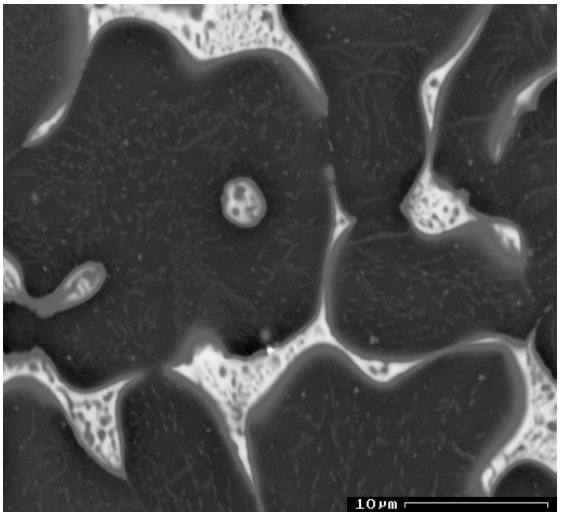

(d) 200°C during 200h

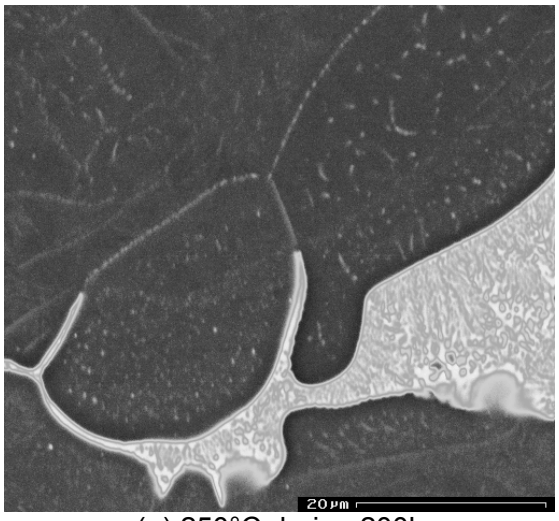

(e) 250°C during 200h

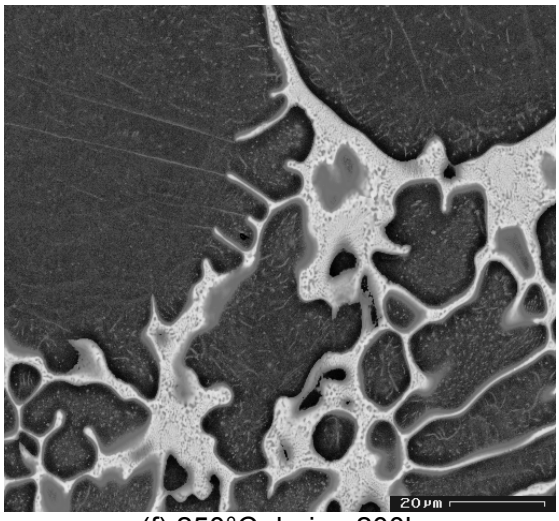

(f) 250°C during 200h

Fig. 54 : Microstructural evolution of the thixocast MEZ alloy exposed to elevated temperatures, SEM-BSE.

6.1.3 Creep behaviour

6.1.3.1 Creep curves

In Fig. 55 the creep strain versus time for the thixocast MEZ alloy at the tested temperatures is displayed. The primary creep of the alloy is very short at all tested temperatures, as can be observed on the detailed diagrams at the right side. After some minutes, the material reaches the secondary stage. At 135 and 150°C, the creep curves present small slopes and small strains up to 80 MPa; at larger stresses, the total strain is relatively large due to the initial strain after loading. The stresses of up to 100 MPa (mainly 90 MPa and 100 MPa) partially exceed the yield strength at room temperature and lead therefore to significant yielding already during the beginning of the experiments. At 175 °C the slopes of the creep curves increase, in particular at higher stresses. At 200°C, the creep exceeds significantly the 1% strain after 100h for stresses of 60 MPa or higher.

Plotting the curves as strain rate versus strain (Fig. 56) gives more information about the behaviour concerning the different stages of creep. From 135°C to 175°C there is a short primary creep followed by a long secondary creep. Due to the very low creep rate during secondary creep the data show a high scatter and no significant change of creep rate can be discerned. No tertiary creep is observed up to the temperature of 175°C, excepting for 175°C and 100 MPa, where the slight onset of the tertiary stage is detected. At 200°C the primary creep range remains short. After reaching the minimum creep rate an increase in the creep rate can be observed, meaning thermal softening of the material. This behaviour is clearly observed already at 50 MPa. At higher stresses, an additional delay in the increase of creep rates can be observed, resulting in a constant creep rate slightly higher than the minimum creep rate. However, in most cases no clear tertiary creep can be observed. Only at 90 MPa the creep rate strongly increases after reaching the minimum creep rate, indicating tertiary creep and failue rupture at 100 MPa the creep rate also slightly increases towards the end of the experiment at about 200 h.

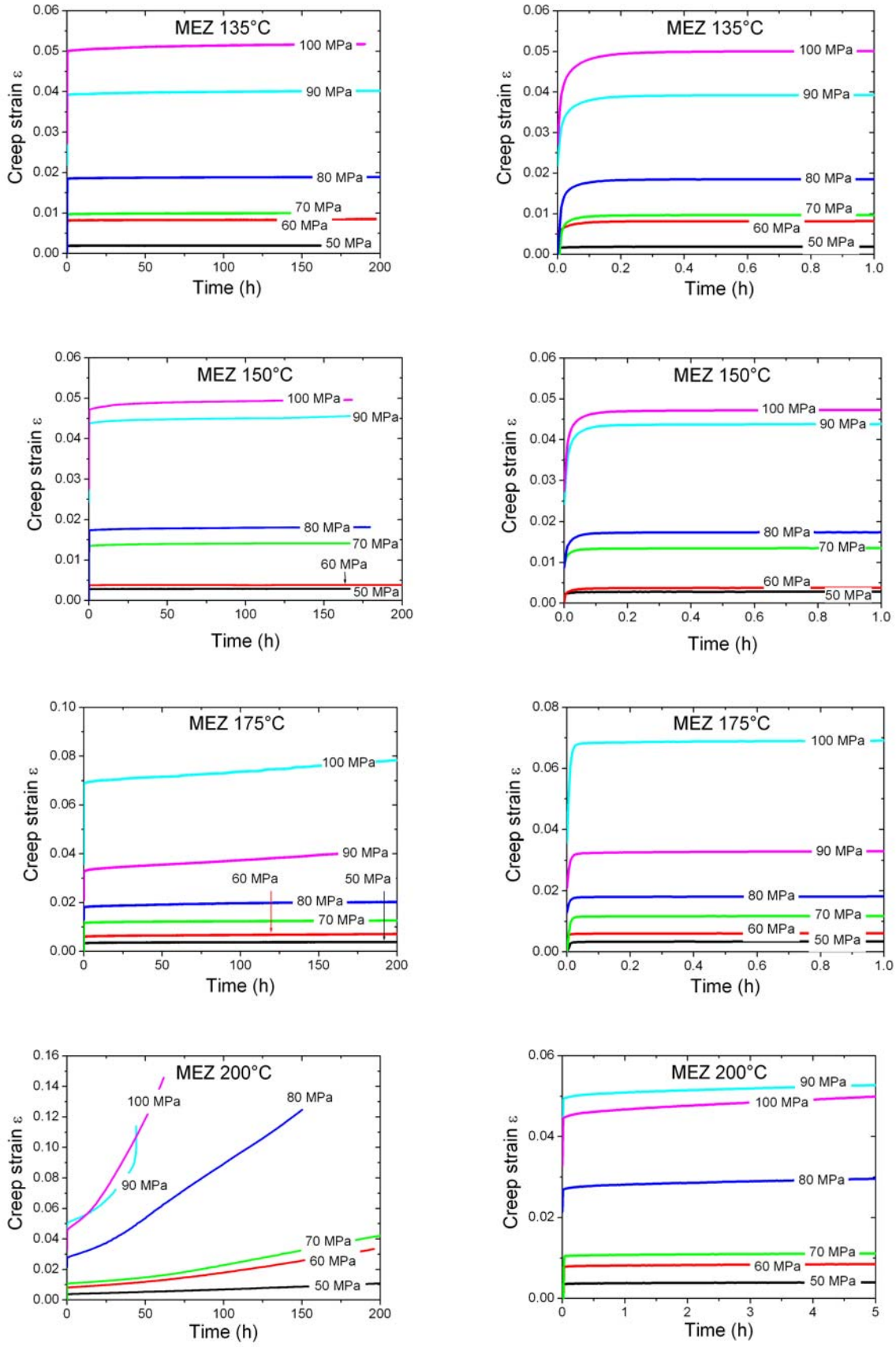

Fig. 55 : Creep strain versus time of the thixocast MEZ alloy at temperatures from 135°C to 200°C. Right diagrams present detailed area of the primary creep.

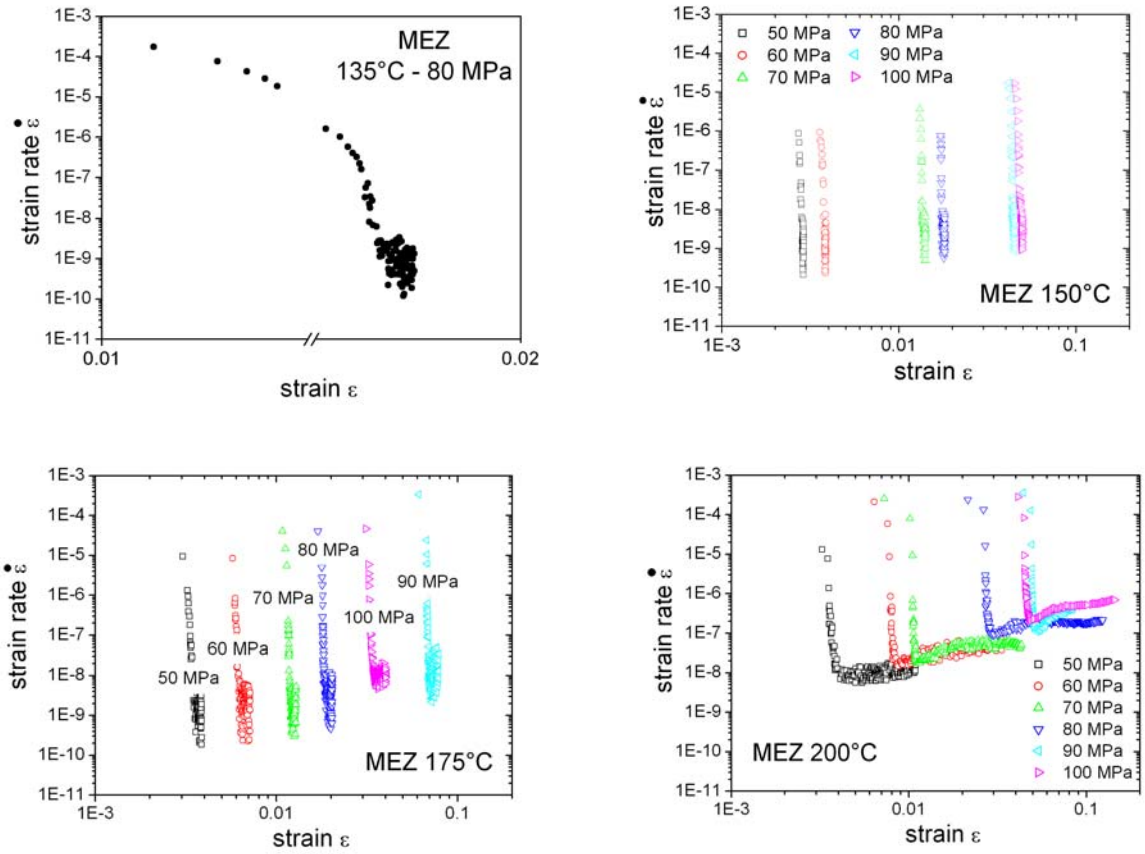

Fig. 56 : Creep strain rate versus strain of the thixocast MEZ alloy at temperatures from 135°C to 200°C.

6.1.3.2 Microstructural evolution after creep

In order to understand the mechanisms during creep the microstructure of the crept samples is investigated after the creep test of 200h as shown in Fig. 57 and Fig. 58.

At 135°C and lower stresses (50 MPa), Fig. 57(a), the microstructure only shows sporadic primary twinning, in accordance to the low initial strain and almost negligible creep strain. As the total deformation is relatively small, extensive twinning is not necessary to achieve the low deformation. At increasing stresses (80 and 100 MPa), Fig. 57 (b + c), twinning is significantly increased and secondary twinning is activated. In addition, primary twinning thickens. As compared to 135°C, at 150°C, the density of primary and secondary twinning increases in the bulk sample even at low stresses (50 MPa), Fig. 57 (d), corresponding to the larger strain rates. The shape of the twinning broadens from thin lamellae to lenticular, with serrated boundaries, as stress is increased (80 MPa), Fig. 57 (e). The eutectic phase appears fractured at 100 MPa and low angle boundaries are visible in some grains, Fig. 57 (f).

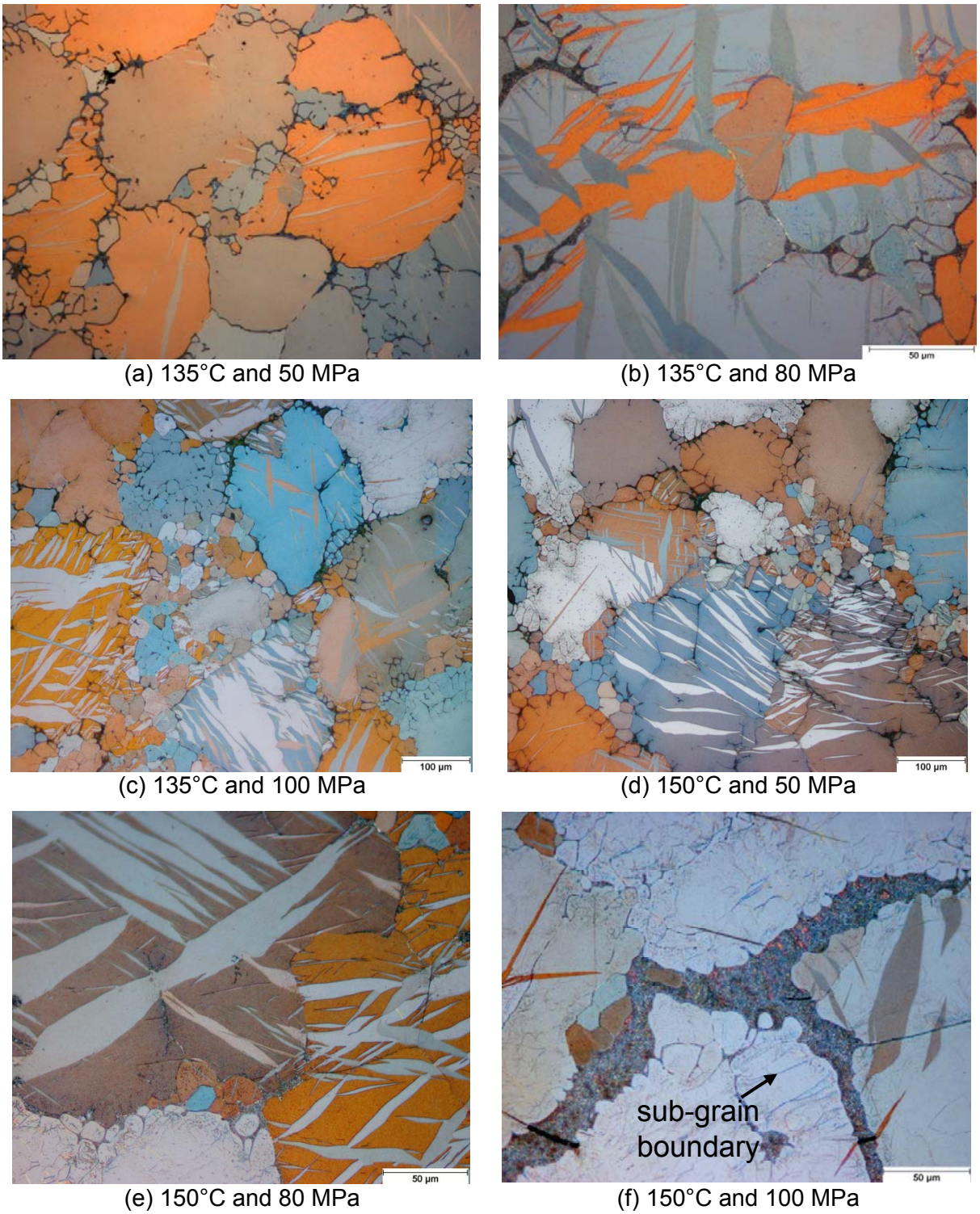

(a) 135°C and 50 MPa (b) 135°C and 80 MPa

(c) 135°C and 100 MPa (d) 150°C and 50 MPa

(e) 150°C and 80 MPa (f) 150°C and 100 MPa

Fig. 57 : Optical micrographs of the thixocast MEZ alloy after creep at temperatures from 135°C and 150°C.

At 175°C, low angle boundaries or substructures are developed within grains, Fig. 58 (a + b). Apparently, only grains with a determined crystallographic orientation are able to develop these substructures. Overaging precipitations can also be observed and this is in accordance with the thermal exposure experiments, which showed a

drop in hardness after a few hours at this temperature. Primary and secondary twinning is also present, as well as fracturated phases at high stresses, Fig. 58 (c). At 200°C, the same features already observed at 175°C are also present, Fig. 58 (d). Dynamic recrystallization is observed inside the α-grains, Fig. 58 (e + f), preferably at higher stresses, only at this temperature.

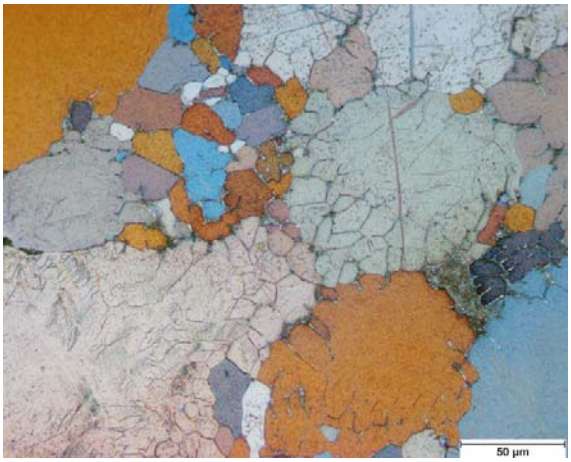

(a) 175°C and 50 MPa

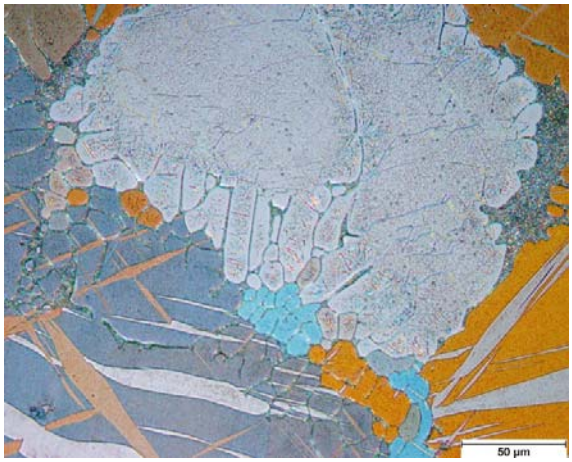

(b) 175°C and 80 MPa

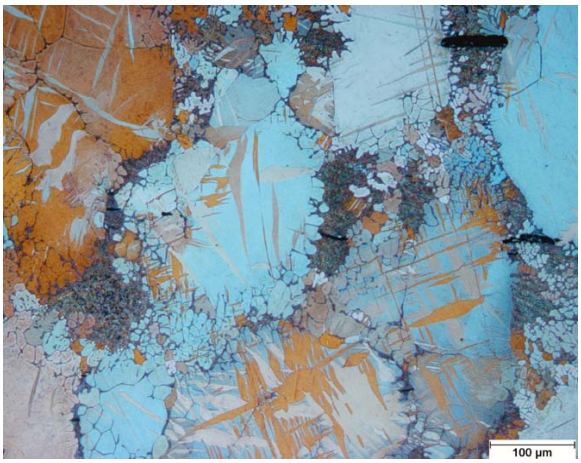

(c) 175°C and 100 MPa

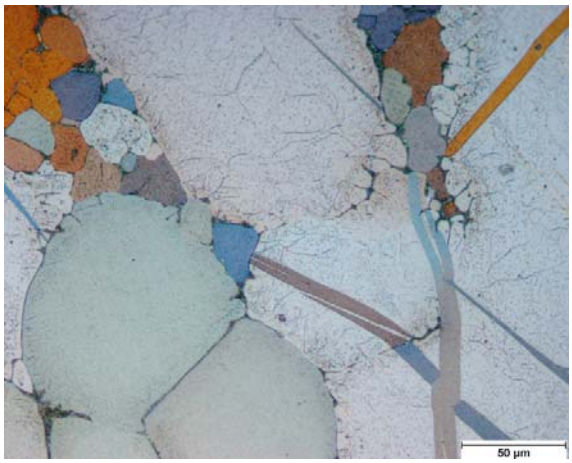

(d) 200°C and 50 MPa

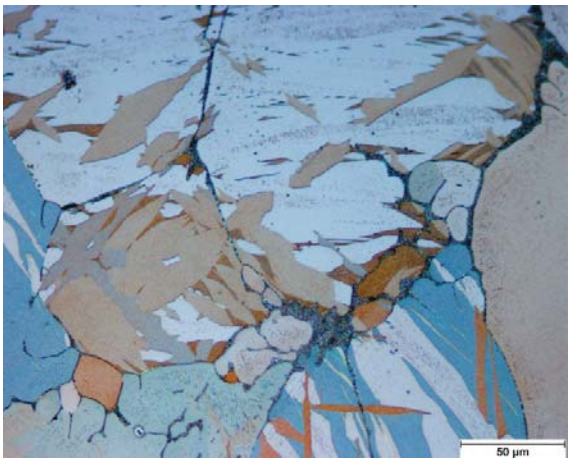

(e) 200°C and 80 MPa

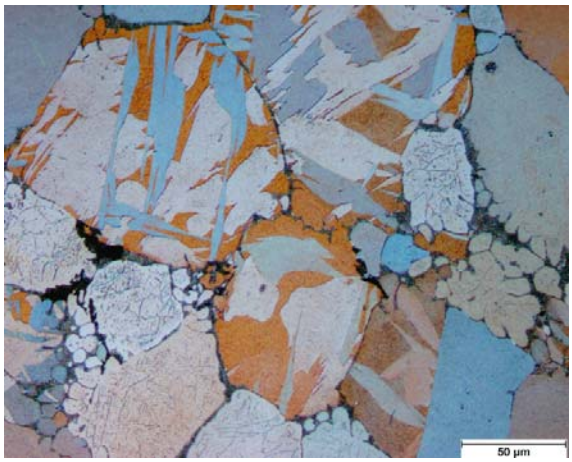

(f) 200°C and 100 MPa

Fig. 58 : Optical micrographs of the thixocast MEZ alloy after creep at temperatures from 175°C and 200°C.

Fig. 59 shows the microstructural analysis of the crept samples of thixocast MEZ focused on the grain boundaries. Signs of fracture of the intermetallic phase can be found even at 135°C, Fig. 59 (a). The straight fracture occurring in 90° to the tensile direction is a result of the high brittleness of the eutectic at the test temperatures, Fig. 59 (a + b). At higher temperatures, in particular at 200°C, the density of cracks in the eutectic phase significantly increases in accordance to the higher strain. The fracture is wavy and branched, because of the increased ductility of the intermetallic phase at these temperatures, Fig. 59 (c). In addition, at higher temperatures, a detachment of the eutectic phase from the α-grains and the rupture through the eutectic along the grain boundaries can be observed, Fig. 59 (d).

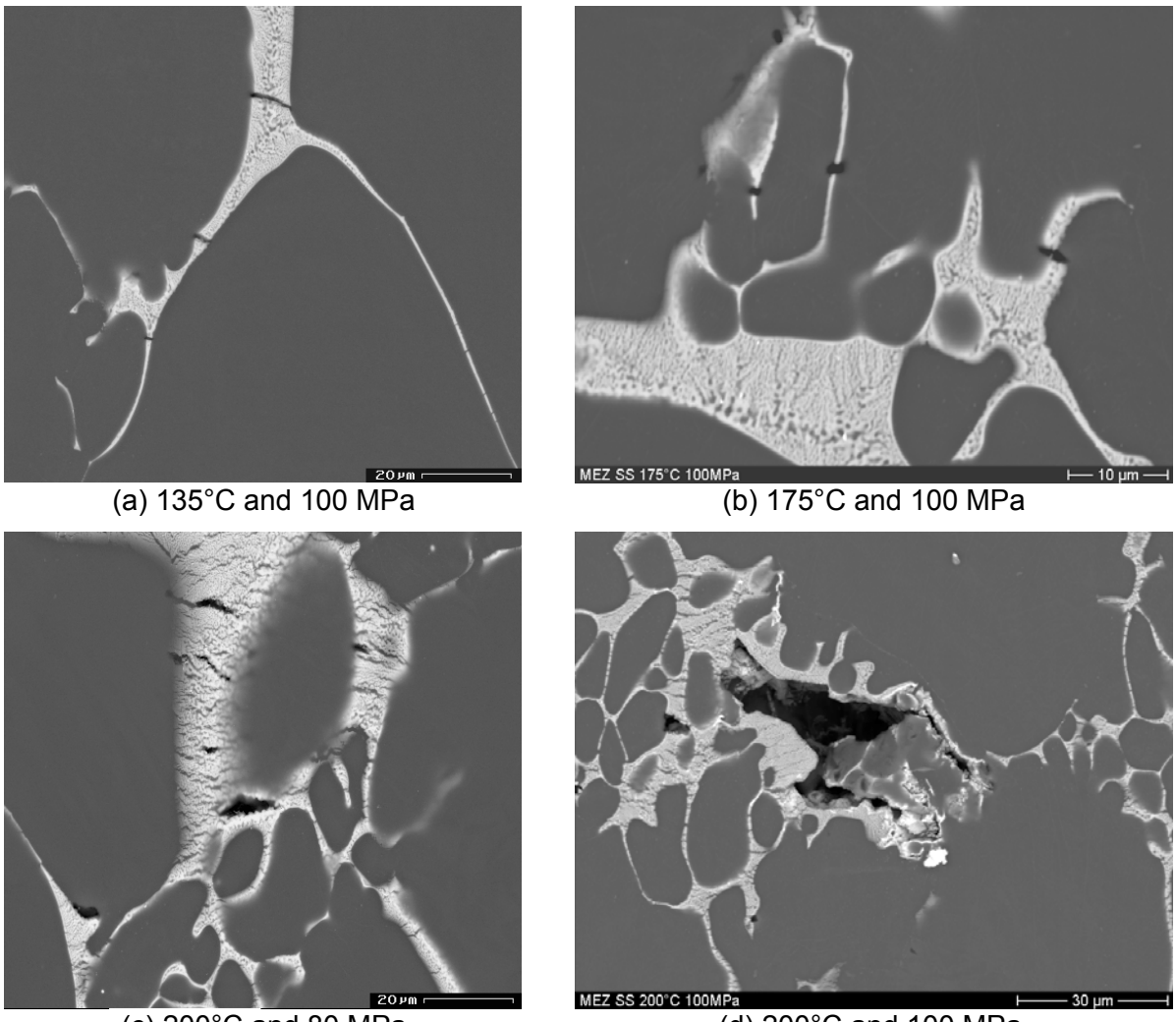

(a) 135°C and 100 MPa (b) 175°C and 100 MPa

(c) 200°C and 80 MPa (d) 200°C and 100 MPa

Fig. 59 : Thixocast MEZ alloy after creep at temperatures from 135°C to 200°C.

For a further characterization of the failure mechanism occurring at higher temperatures the surface of the sample has been analysed by scanning electron microscopy, Fig. 60. At 200°C and 90 MPa the sample shows detachments of grain

boundaries, preferably at triple junctions, commonly known as wedge formation, Fig. 60 (a). No clear evidence of grain boundary sliding can be observed, as shown in Fig. 60 (b), where horizontal marks are wavy because of the deformation, but remain continuos without steps between grain boundaries.

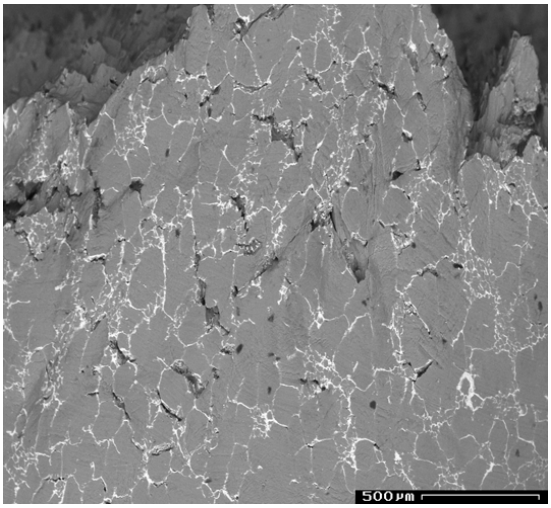

(a) 200°C and 90MPa, SEM-BSE

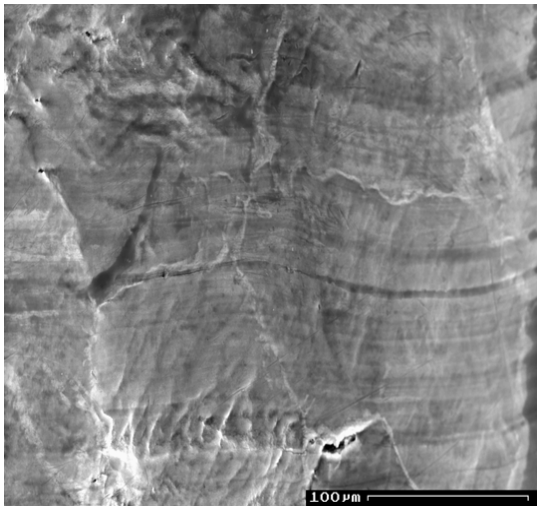

(b) 200°C and 90 MPa, SEM-SE

Fig. 60 : SEM analysis of the surface of samples of the MEZ alloy after creep and rupture at 200°C and 90 MPa (tensile direction is vertical)

The fracture surface analysis of a typically ruptured sample at 200°C and 90 MPa is shown in Fig. 61. In contrast to the fracture at room temperature, grains cannot be identified due to the ductile features overlaying the grain structure, Fig. 61 (a) . A closer look at the fracture surface shows predominantly shear lips of 10-50 µm length, Fig. 61 (b). Ductile shear fracture in the α-Mg phase is observed, resulting possibly from fracture of the eutectic, combined with transgranular fracture.

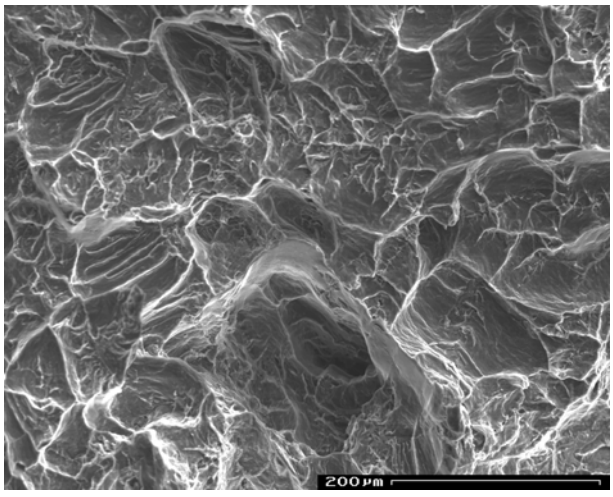

(a)

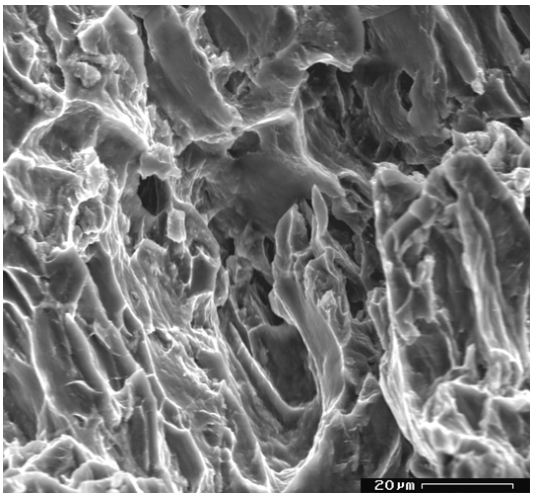

(b)

Fig. 61 : SEM micrographs of the fracture surface of the MEZ alloy after creep at 200°C and 90 MPa.

The twin formation observed already in optical microscopy is confirmed by TEM analysis of a sample crept at 175°C and 80 MPa (Fig. 62 (a)). Round precipitation of typically 200 nm is observed close to the grain boundaries already at 175°C (Fig. 62 (b)). Dislocation pinning can be discerned because of the dislocations attached to these precipitations (Fig. 62 (c + d)). Additionally, alignments of small plates found in the as-cast samples can be also found in the crept samples (Fig. 62 (e)). Areas of high density of dislocations are observed in the grain interior, which could not be seen in the as-cast condition (Fig. 62 (f)). In some cross sections these areas of high dislocation density show parallel lines, result of dislocation slip in the basal plane (Fig. 62 (g)). A high number of dislocation tangles perpendicular to basal plane are the result of strong dislocation climb or cross slip (Fig. 62 (h)).

The TEM micrographs at higher temperatures and stresses (200°C and 80MPa), where significant pseudo-tertiary creep has prevailed, also show additionally signs of severe recrystallization. Grains of a few micrometers are observed, indicating recrystallization of sub-structures (Fig. 63 (a)). Additionally, in areas of high dislocation density, elongated strain free grains appear, which are result of recrystallization or recovery of twinned grains (Fig. 63 (b)). Precipitations of about 30 nm can also be observed within the grains, which are result of the higher heat exposure, like the observed after aging of the thixocast sample (Fig. 63 (c)). These precipitations can also be found in wavy alignments, indicating preferred precipitation at sub-grain boundaries (Fig. 63 (d)). The alignment of small plates all with the same orientation can also be found in the crept samples (Fig. 63 (e)). The bowed out shape of these alignment shows that these plate shaped defects have moved in the direction of their orientation and have been pinned to precipitates. Still areas of high dislocation densities can be found as for the lower creep temperature (Fig. 63 (f+g)). Again these areas show dislocation forests, sometimes with perpendicular orientation of the dislocation lines as typical for dislocation climb or cross slip. In some parts, also large dislocations of 300 nm can be found, which are oriented in the same direction as the plate shaped and aligned features observed in the as cast condition (see Fig. 27).

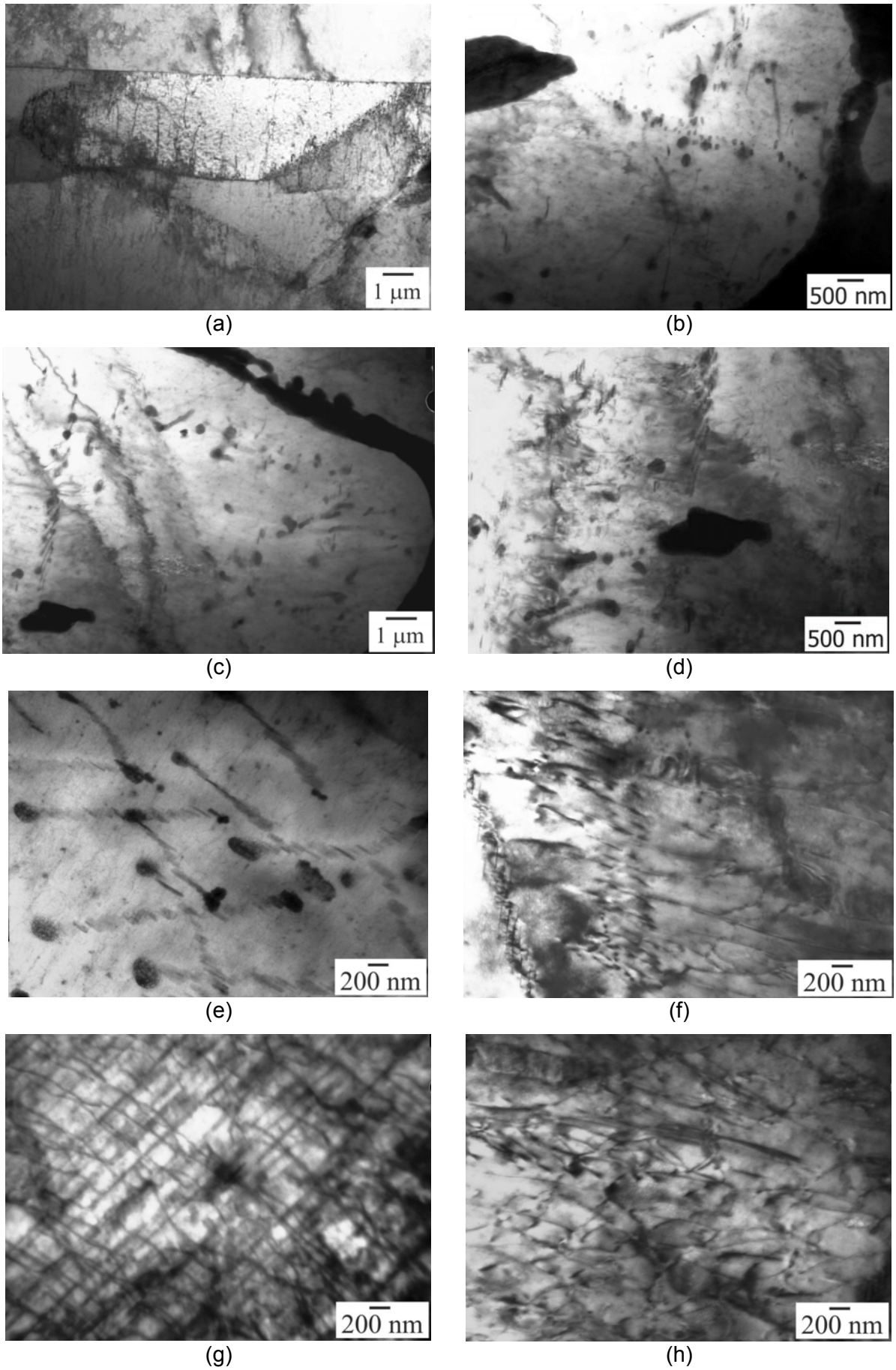

Fig. 62 : TEM micrographs of the MEZ alloy after creep at 175°C and 80 MPa.

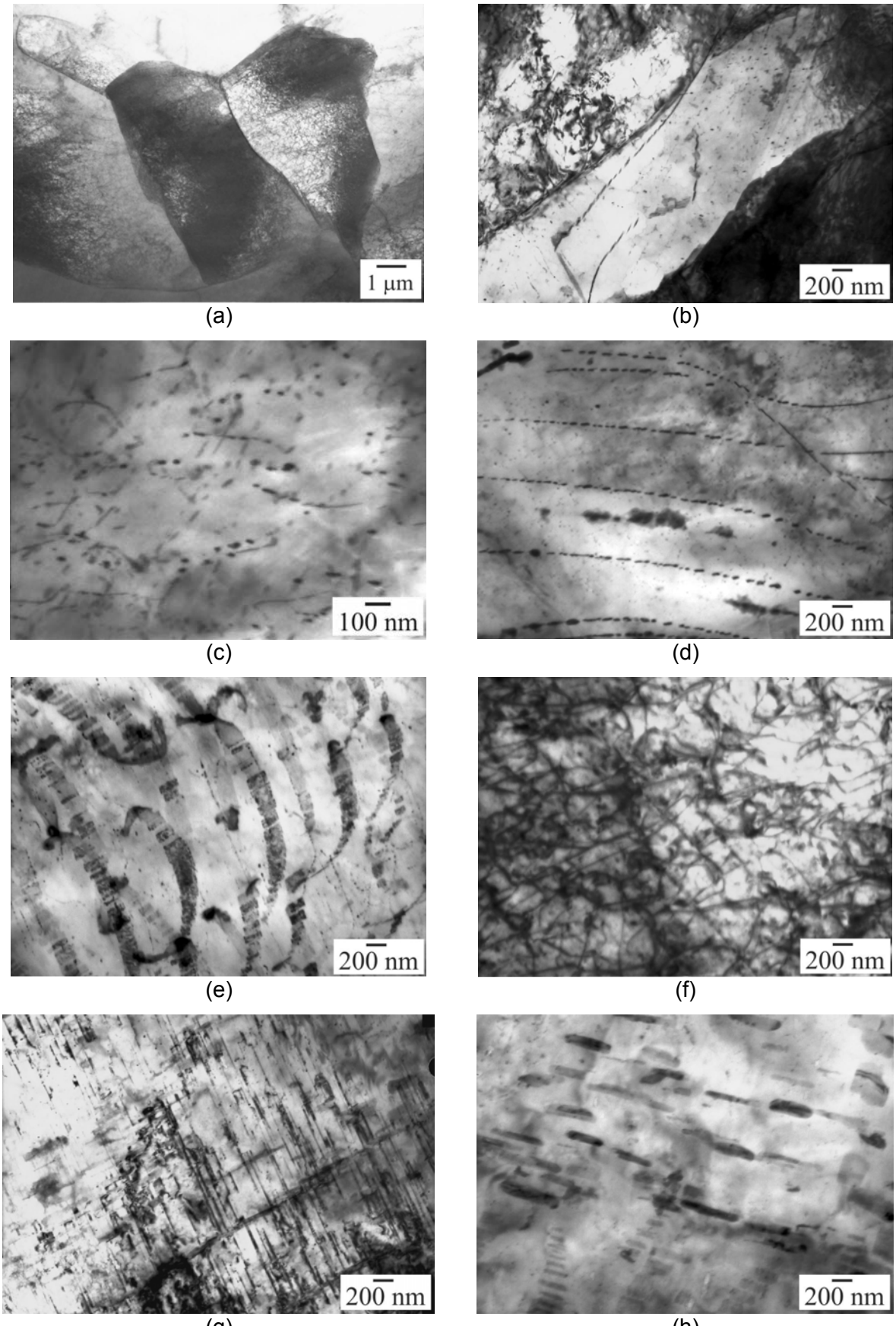

Fig. 63 : TEM micrographs of the MEZ alloy after creep at 200°C and 80 MPa.

6.2 ZECa-System

6.2.1 Mechanical properties at room temperature

6.2.1.1 Hardness, tension and compression tests

The hardness value of the as-cast ZECa material was measured as 53.1 ±1.0 HV10.

Representative engineering stress-strain curves for the thixocast ZECa alloy at room temperature in tension and compression are displayed in Fig. 64. The ZECa alloy shows a wider elastic range in comparison to the MEZ alloy, corresponding to a higher tensile yield strength and a faster transition to the plastic mode. The higher tensile yield strength of the ZECa sample is nevertheless accompanied by a lower elongation. The same trend is observed for the compressional load. Although the values of tensile and compressive yield strength are almost the same, like for the MEZ alloy, the ultimate compressive strength is more than two times higher than the value of the ultimate tensile strength. The strain in compression is four times higher than in tension. The tensile curve shows two deformation stages, while the compressive curve shows three.

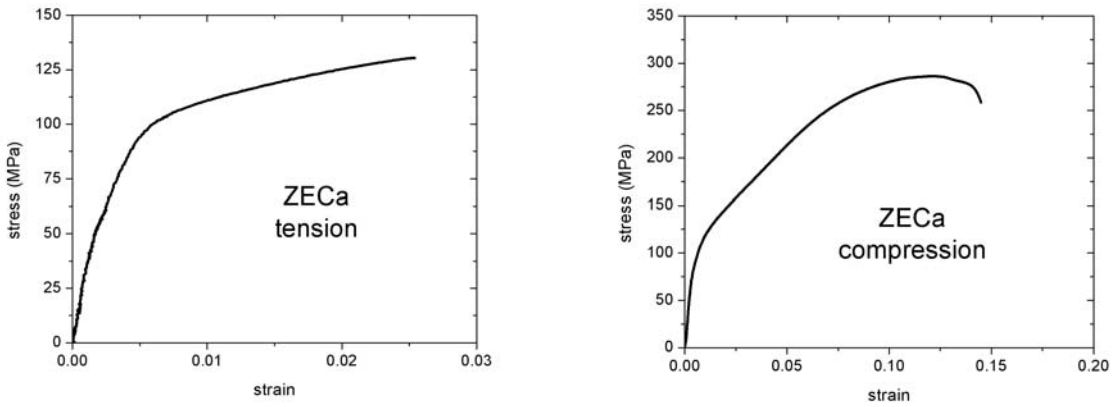

(a) (b)

Fig. 64 : Representative stress-strain curves of the ZECa alloy in tension and compression.

The strain hardening exponent, n, and the strength coefficient, K, were determined after plotting the true-stress versus true-strain curves of the tensile tests. The tensile and compressive properties of the ZECa alloy are summarized in Table 13. The values represent the average of 6-8 tests at room temperature.

Table 13 : Tensile and compressive properties of the thixocast ZECa alloy at room temperature.

ZECa	Tension	Compression
0.2% TYS (MPa)	91.6 ± 6	
UTS (MPa)	125.9 ± 6	
% elongation	2.4 ± 1	
0.2% CYS (MPa)		93.8 ± 6.9
UCS (MPa)		284.9 ± 4.3
% compression		12.3 ± 0.7
n (strain hardening exponent)	0.16 ± 0.004	
K (strength coefficient), MPa	235.5 ± 9	

6.2.1.2 Microstructural analysis of deformed samples

Fig. 65 shows the microstructure of the ZECa alloy after tension at room temperature. The main feature is the presence of primary and secondary twins mainly with lenticular shape, Fig. 65 (a). Massive coarse twinning is also present in some grains heavily deformed, with serrrated boundaries, Fig. 65 (b).

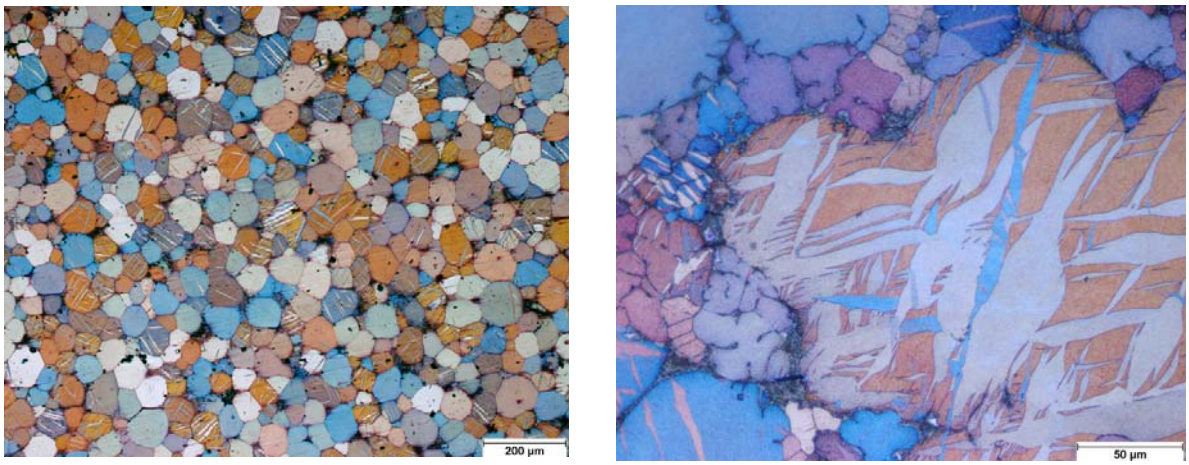

(a) (b)

Fig. 65 : Thixocast ZECa alloy after tension tests at room temperature, optical microscopy.

Analyses of the fracture surface of tensile specimens of the ZECa alloy are presented in Fig. 66. The observed fracture is ductile-brittle and mainly intergranular. The intergranular fracture exhibits typical fine eutectic structure and substantial crack branching of the intermetallic phases, Fig. 66 (a). Some parts present fracture through the α-phase, showing relatively poor deformation, Fig. 66 (b).

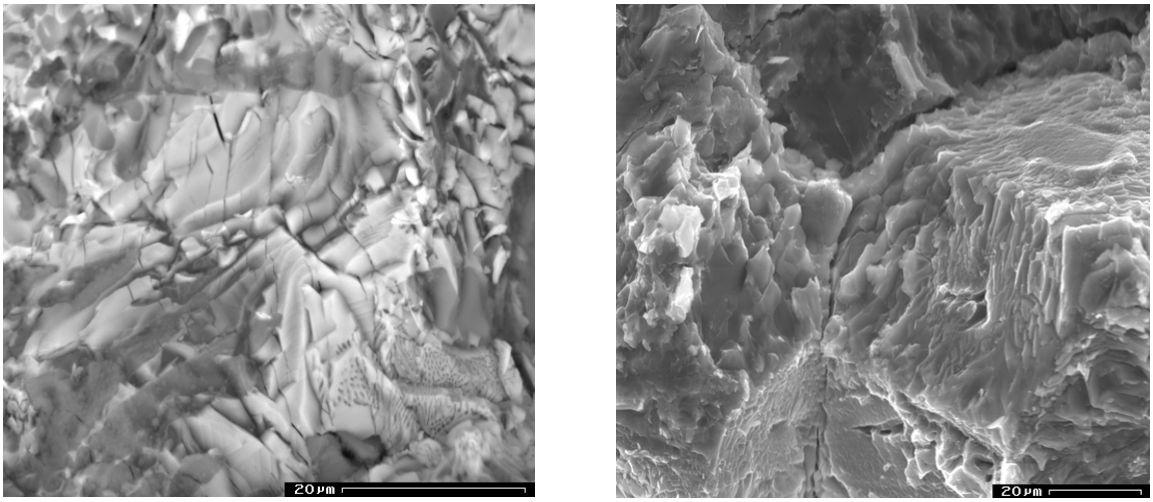

(a) SEM-BSE (b) SEM-SE

Fig. 66 : Fracture surface of the thixocast ZECa alloy tested at room temperature in tension.

Fig. 67 shows the microstructure of the thixocast ZECa alloy after compression at room temperature. In accordance to the high strain achieved in compression, the originally globular grains are elongated. The formation of shear bands can be observed, as is indicated by their typical wavy form, Fig. 67 (a). Moreover, dynamical recrystallization is also observed, Fig. 67 (b). Massive twinning is observed, particularly in regions away from the fractured surface.

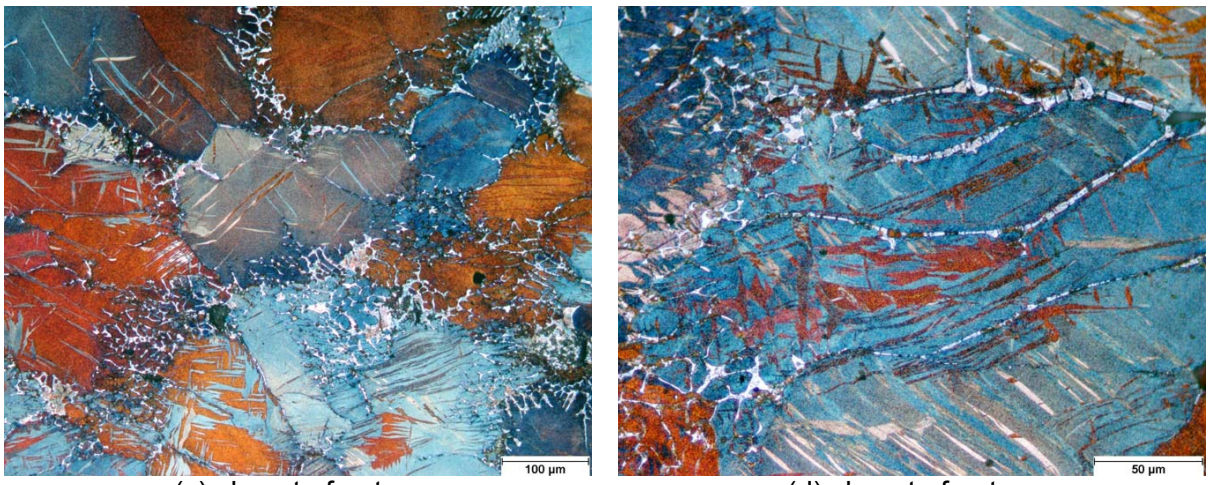

(c) close to fracture (d) close to fracture

Fig. 67 : Thixocast ZECa alloy after compression tests at room temperature, optical microscopy.

Fig. 68 shows the microstructure of the deformed material in compression using SEM. The intermetallic phases fracture in the compression direction mainly at the grain boundaries of the primary α-grains. No crack propagation is observed along the grain boundaries. However, it can be seen that the crack is initiated at the intermetallic phase and then propagates intragranulary into the magnesium grains.

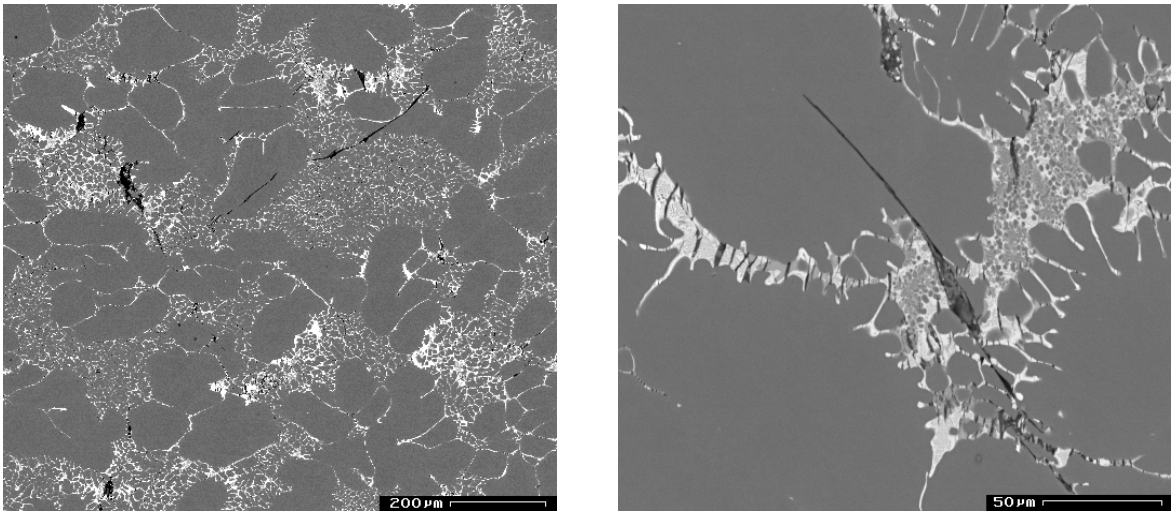

(a) (b)

Fig. 68 : Thixocast ZECa alloy after compression tests, SEM-BSE.

Fig. 69 shows the fracture surface of the ZECa alloy after compression tests. The fracture propagates mainly transgranular, showing only little sections of the intermetallic phase on the fracture surface, Fig. 69 (a). The close-up view indicates cross slip lines, arising in a slant angle to the main shear direction, Fig. 69 (b).

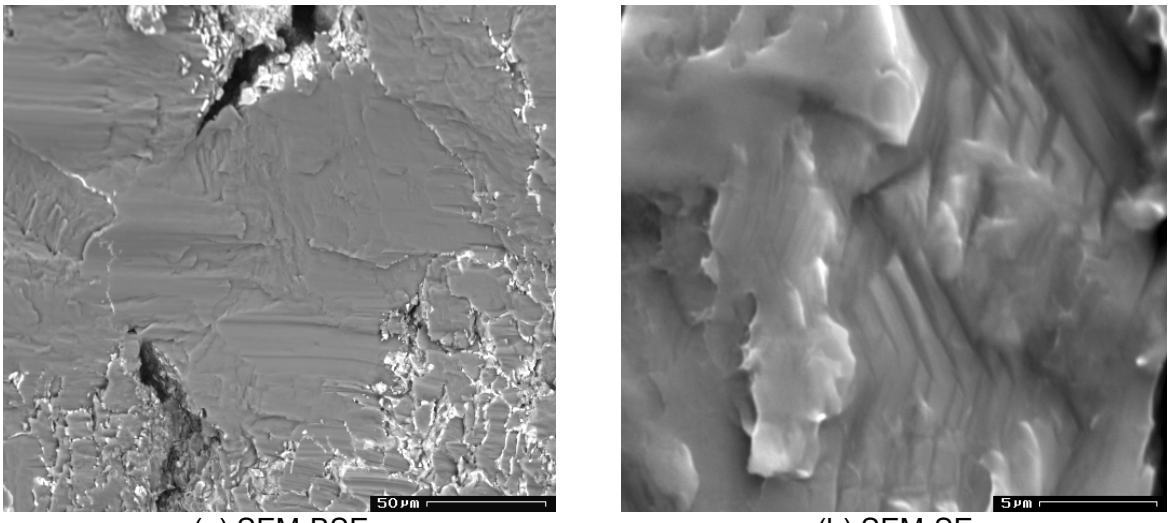

(a) SEM-BSE (b) SEM-SE

Fig. 69 : Fracture surface of the thixocast ZECa alloy after compression at room temperature.

6.2.2 Microstructural stability with temperature

6.2.2.1 Hardness evolution after aging

Fig. 70 shows the evolution of hardness at different times of temperature exposure for the ZECa alloy. At 135°C, the hardness decreases first and then increases again to about the initial value after 200h. At 150°C, the hardness increases slowly with the exposure time up to 100 h and then remains constant, while at 175°C the hardness increases markedly up to 200h, resulting of an aging effect. At 200°C there is a sharp hardness increase during the first 25h, and then it remains constant up to 100h and after that it decreases drastically at 200h up to about the initial value.

The hardness does not drop below the initial value, except at 135°C, even at temperature exposure of 200°C for 200h. Additionally, overaging initiates only after a prolonged time of thermal stability, i.e. after 100h at 200°C.

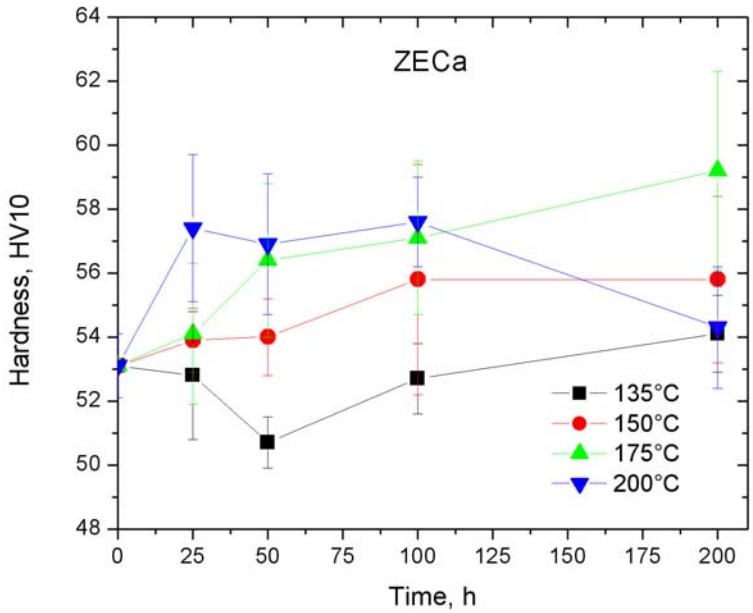

Fig. 70 : Hardness evolution of the thixocast ZECa alloy at the exposure to elevated temperatures (initial hardness was 53 HV10).

6.2.2.2 Microstructural evolution after aging

Microstructural changes were not detected up to 175°C, meaning that the precipitation hardening observed takes place on a very small scale, which usually cannot be resolved by the scanning electron microscope. After thermal exposure at 200°C for 200h, secondary precipitation becomes visible also as sub-grain

boundaries within the α-grains, Fig. 71 (a + b). When the exposure time is increased, the precipitates become thicker and decorate the sub-grain boundaries of particular α-grains, Fig. 71 (c + d).

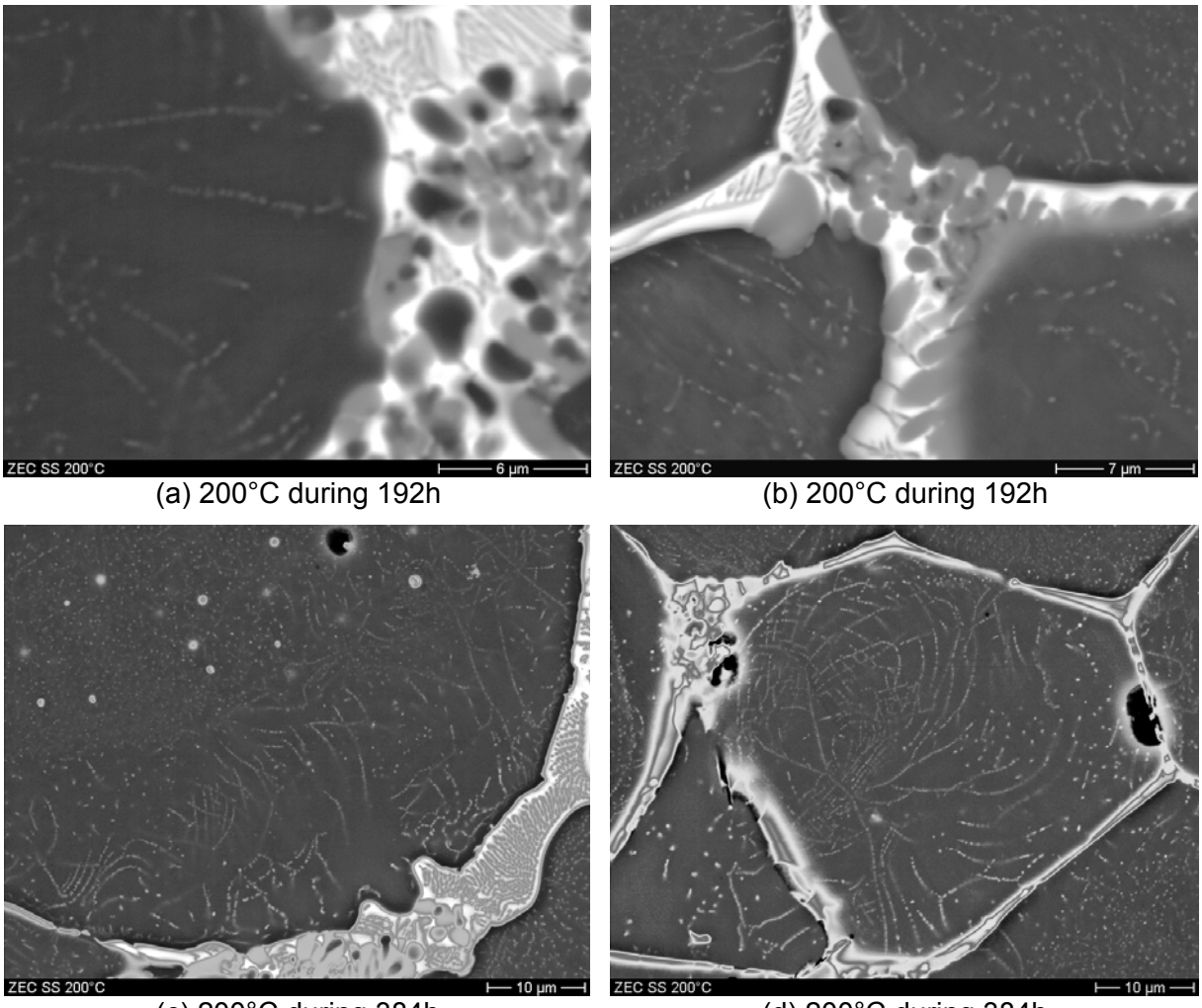

(a) 200°C during 192h (b) 200°C during 192h

(c) 200°C during 384h (d) 200°C during 384h

Fig. 71 : Microstructural evolution of the thixocast ZECa alloy exposed to 200°C at different times, SEM-BSE.

6.2.3 Creep behaviour

6.2.3.1 Creep curves

The creep strain versus time curves of the thixocast ZECa alloy tested from 50 to 100 MPa at different temperatures are displayed in Fig. 72. Primary creep in the ZECa alloy occurs shortly after loading at 135 and 150°C, which can be observed in the detailed diagrams of the right side. For all temperatures, initial creep strain increases progressively with the stress applied with one exception at 175°C at 90 MPa, where

the initial strain rate is unusually high, meaning a heterogeneous or mixed microstructure or even local failure in the sample.

At low stresses, the observed initial strains are very low and do not increase as temperature increases, which corresponds to only elastic deformation of the samples. At higher stresses, loading exceeds significantly the yielding of the material, which is 91 MPa at room temperature and therefore the experimental handling can significantly contribute to the initial strain.

At 135°C the total creep strain after 200h of thermal exposure is below the 0.3 % for lower stresses (up to 70 MPa) and also the creep rates are very low. At 150°C, a jump in the initial strain can be observed between 60 MPa and 70 MPa, corresponding to the trespassing of yield at this temperature. However, the creep strain is significantly below 0.25 % up to 80 MPa, which indicates that even at stresses exceeding the yield strength at this temperature, low total strain can be achieved by strain hardening, possibly aided by further hardening mechanisms. At 175°C, still very low total strains (<1 %) can be observed up to about 70 MPa. Above this value, there is a clear onset of the tertiary creep seen at 80, 90 and 100 MPa already within the 200h of testing time. At 200°C total creep strains smaller or equal to 1 % after 200h of testing without a clear onset of tertiary creep can only be reached at stresses of 50 MPa or below. At higher stresses, the tertiary creep sets in after only a few hours, leading to abrupt elongation of the samples before the maximum test time of 200 h is completed.

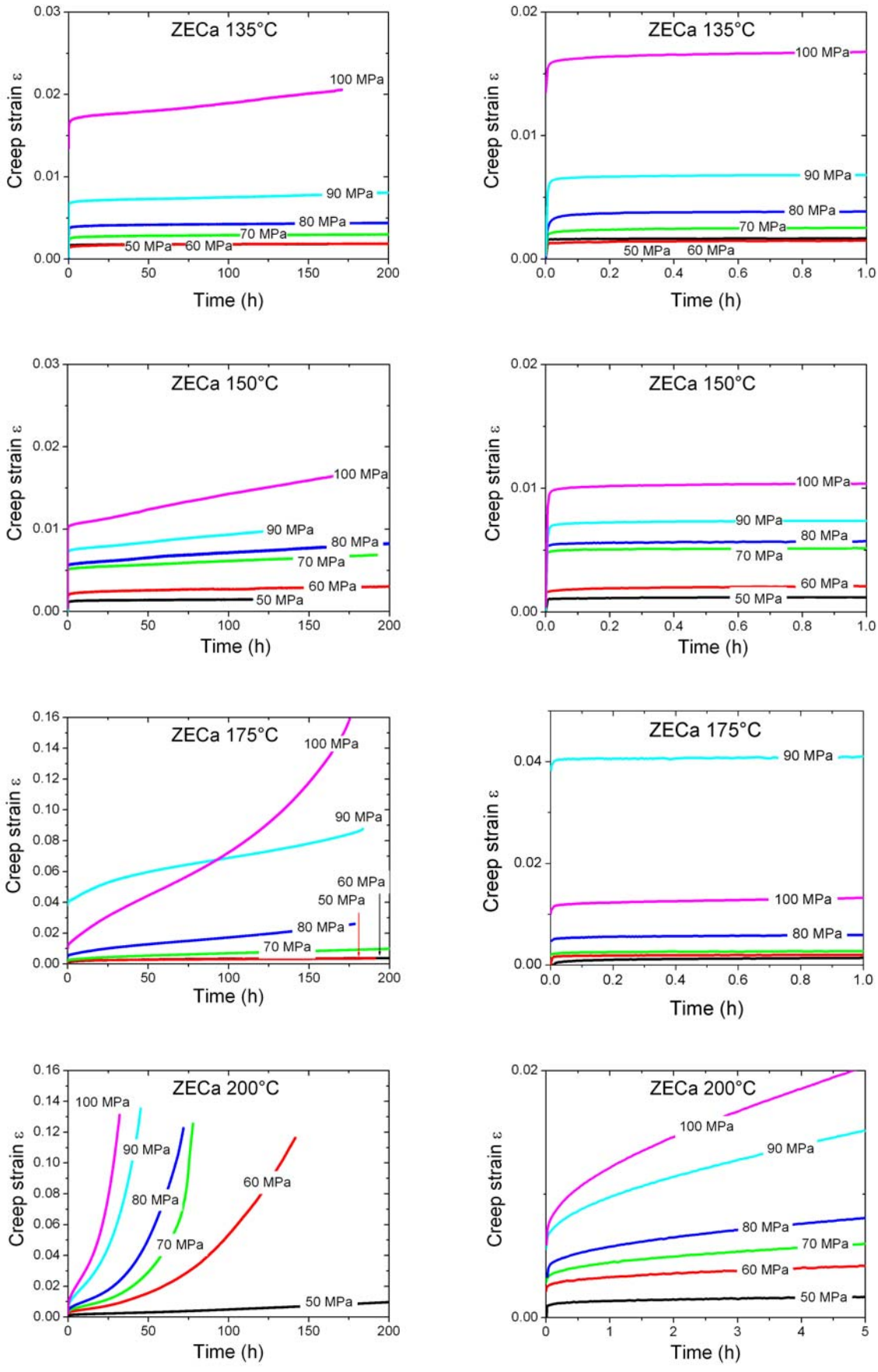

Fig. 72 : Strain versus time of the thixocast ZECa alloy at temperatures from 135°C to 200°C.

In order to further elucidate the change of creep rates with the advancing strain, the strain rate versus strain curves are represented in Fig. 73. As in the MEZ alloy, at 135°C and 150°C, after a short primary creep no significant change of strain rates can be observed with respect to the advancing strain within the scatter found. At 175°C, strain rates firstly tend to decrease with advancing creep strain and at stresses of 70 MPa and higher, tend to increase with proceeding creep strain, indicating a softening mechanism or the onset of tertiary creep. At 200°C, a highly enlarged primary region is followed by direct, smooth transition to constantly increasing creep rate, indicating a hardening mechanism followed by thermal softening.

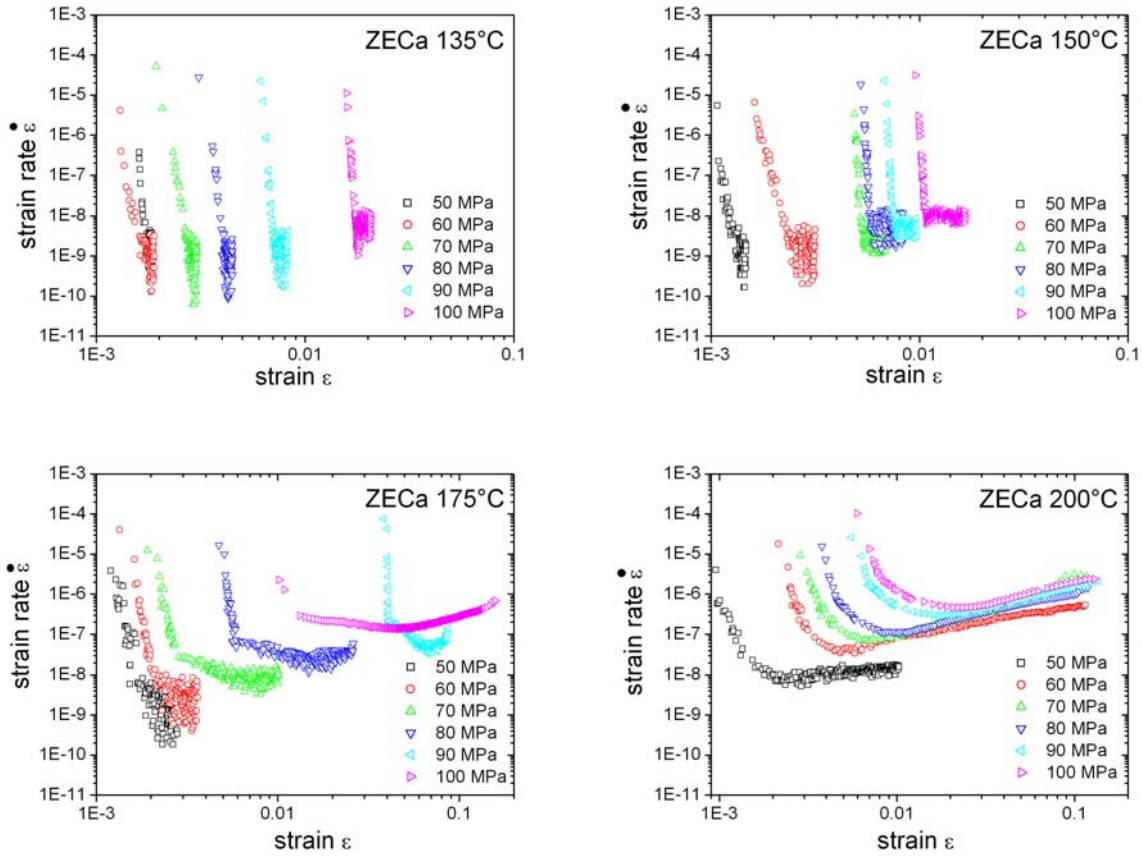

Fig. 73 : Strain rates versus strain of the ZECa alloy at temperatures from 135°C to 200°C.

6.2.3.2 Microstructural evolution after creep

The thixocast ZECa alloy does not show marked changes in its microstructure after creep at 135°C and 150°C. As for the MEZ alloy, primary and secondary twinning is found only scarcely, Fig. 74 (a + c), except at higher stresses, Fig. 74 (b + d), where twinning increases slightly.

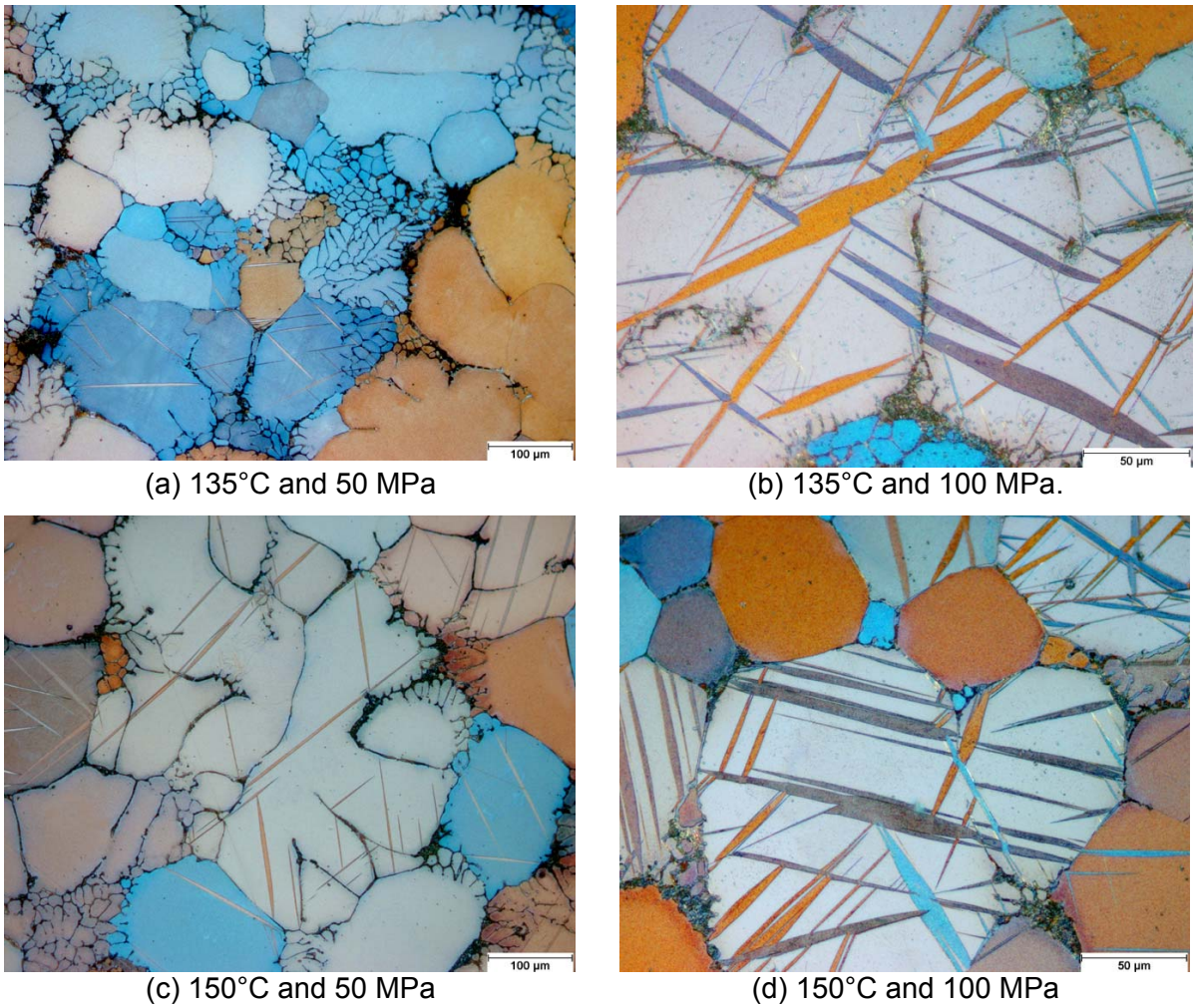

(a) 135°C and 50 MPa (b) 135°C and 100 MPa.

(c) 150°C and 50 MPa (d) 150°C and 100 MPa

Fig. 74 : Microstructure of the thixocast ZECa alloy after creep at 135°C and 150°C and 50 MPa and 100 MPa, optical microscopy.

At 175°C, primary twinning is observed at low stresses in some α-grains. As the stress increases, secondary twinning is activated. Only at very high stresses (100 MPa), dynamical recrystallisation can be found in some α-grains, Fig. 75 (a + b). At 200°C, twinning as well as dynamical recrystallisation is observed already at 80 MPa, Fig. 75 (c + d). At higher stresses, twinning is replaced by dynamical recrystallisation. The severe appearance of precipitations inside the grains, as observed in the MEZ alloy cannot be found in the ZECa alloy.

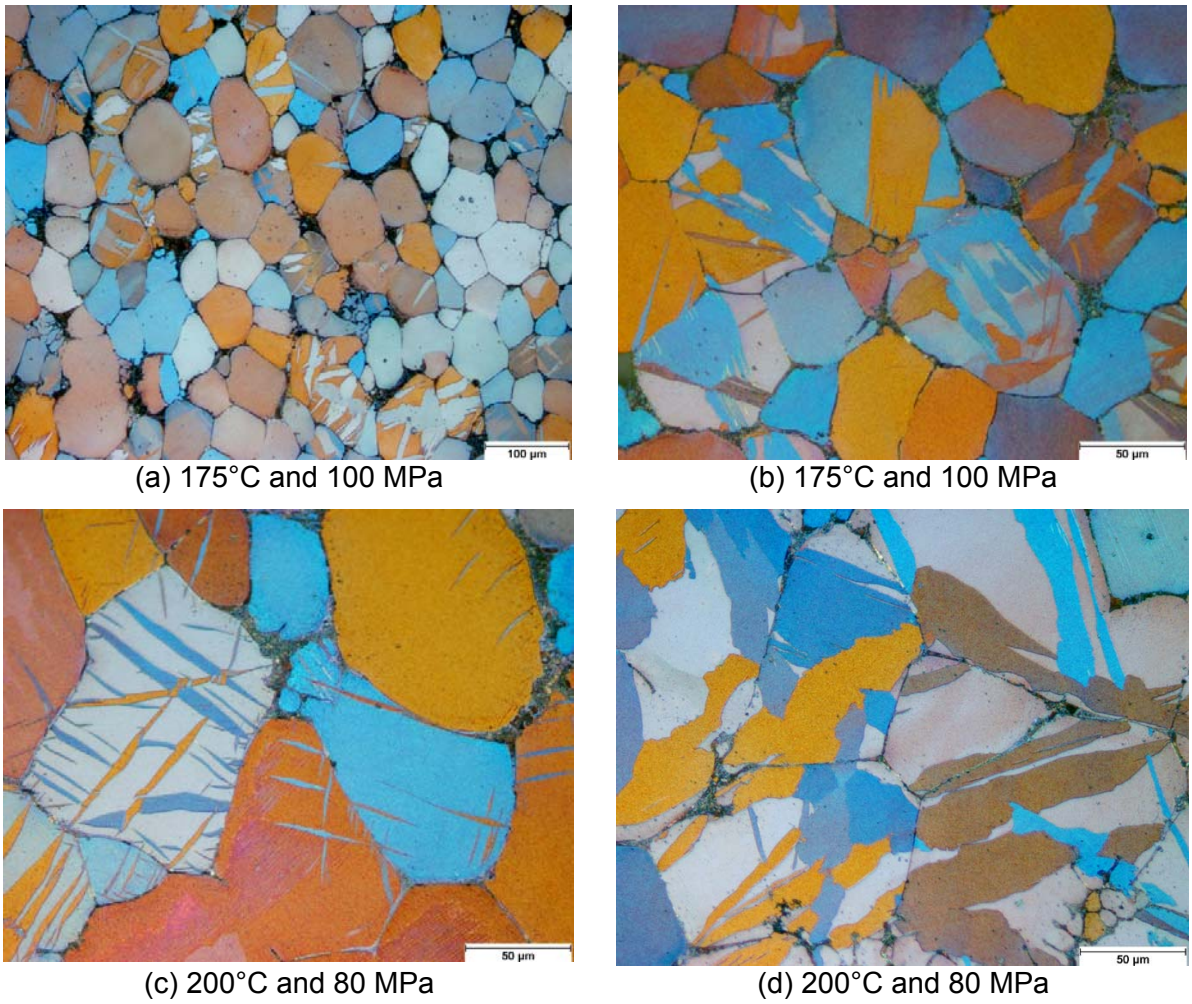

(a) 175°C and 100 MPa (b) 175°C and 100 MPa

(c) 200°C and 80 MPa (d) 200°C and 80 MPa

Fig. 75 : Microstructure of the thixocast ZECa alloy after creep at 175°C and 200°C at different stresses, optical microscopy.

Representative SEM-BSE micrographs of the thixocast ZECa alloy after creep tests are shown in Fig. 76. In general, the microstructure reveals breakage and deterioration of the ternary eutectic phase even at low stresses, Fig. 76 (a). As the stress increases, this effect becomes more evident in the material. Because of creep deformation, intermetallic phases at grain boundaries appear broken and displaced from its original position, Fig. 76 (b). At temperatures of 175°C and higher, wavy cracks are found in the ternary eutectic phase, Fig. 76 (c + e). The binary phase also breaks when it is found together with the ternary phase. At high stresses, cavities are formed after breakage of the ternary phase in triple junctions, like in Fig. 76 (d). Severe deformation is observed at the grain boundaries as indicated by small cracks in the eutectic phase preferably in an 45°-angle to the tensile direction, Fig. 76 (g). At higher temperatures, precipitation in the α-grains is detected, Fig. 76 (f + h). Grain boundaries which are free of eutectic are also decorated with precipitates, Fig. 76 (e).

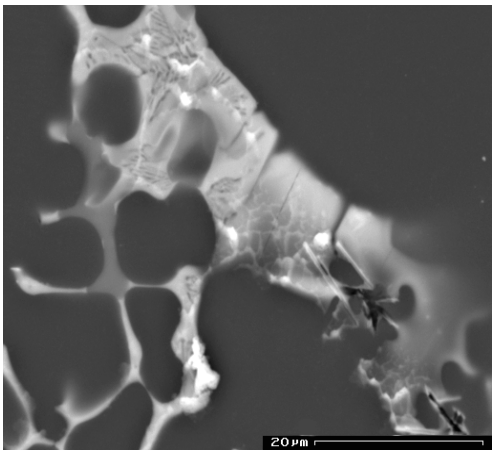

(a) 135°C and 80 MPa

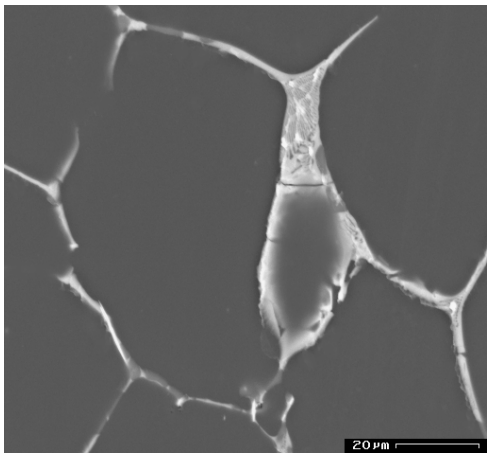

(b) 150°C and 80 MPa

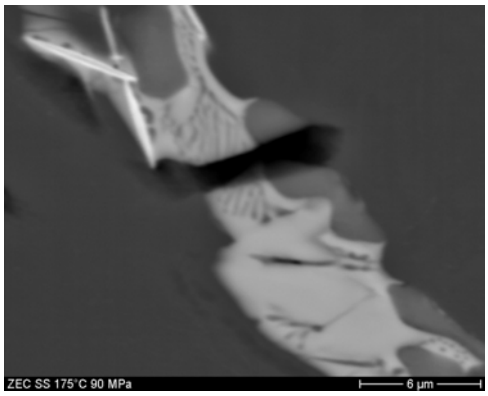

(c) 175°C and 90 MPa

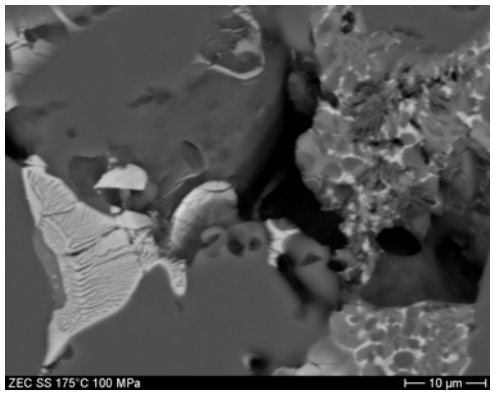

(d) 175°C and 100 MPa

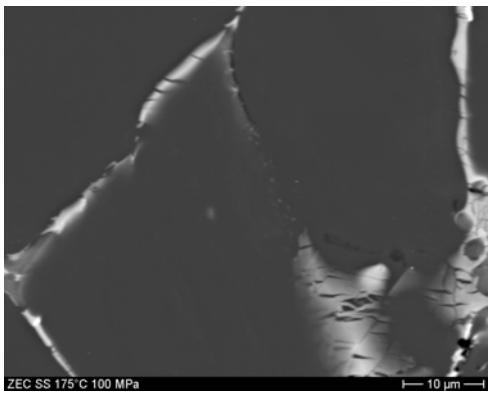

(e) 175°C and 100 MPa

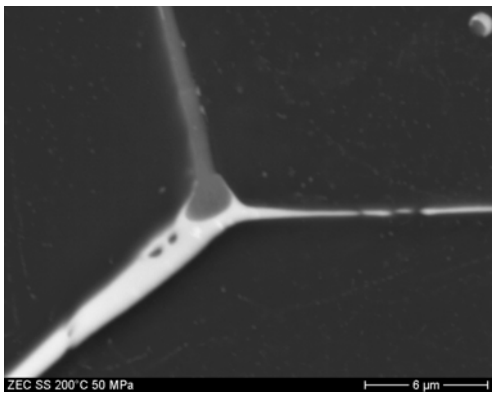

(f) 200°C and 50 MPa

(g) 200°C and 100 MPa

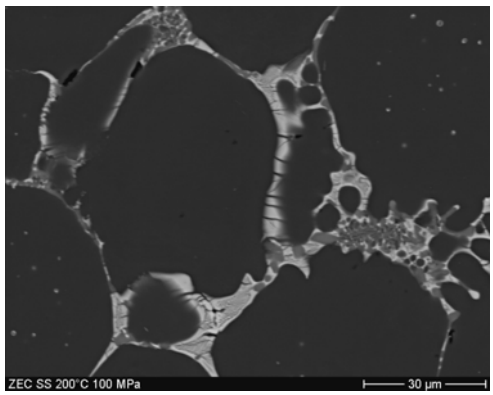

(h) 200°C and 100 MPa

Fig. 76 : Microstructure of the thixocast ZECa alloy after creep at different temperatures and stresses (tensile direction vertical, bright: $Mg_6Ca_2Zn_3$, grey: Mg_2Ca, dark grey: α-Mg), SEM.

For a further characterization of the failure mechanism occurring at higher temperatures, the surface of the sample has been analyzed by scanning electron microscopy in Fig. 77. At 200°C and 90 MPa, the sample shows severe detachments of grain boundaries, preferably at triple junctions, commonly known as wedge formation, Fig. 77 (a + c). Breakage of the ternary phase can also be clearly observed, Fig. 77 (b). A closer look at the grains shows that significant grain boundary sliding has occurred. This can in particular be evidenced by the stripes resulting from the turning of the samples, which are clearly offset against each other, Fig. 77 (d). It should be noted that grain boundary sliding is obvious even at boundaries with a low concentration of eutectic phases.

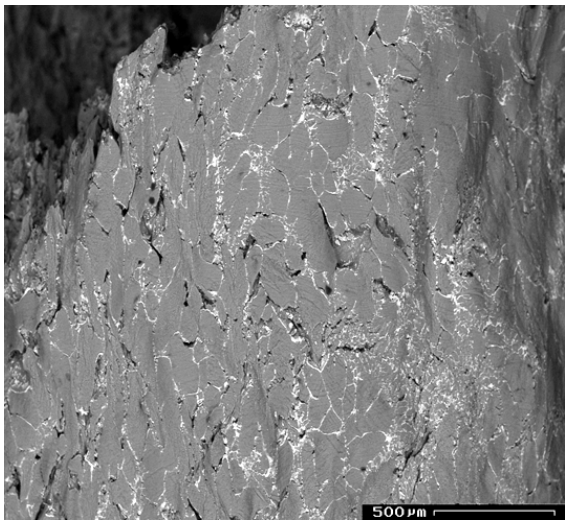

(a) 200°C and 90MPa, SEM-BSE

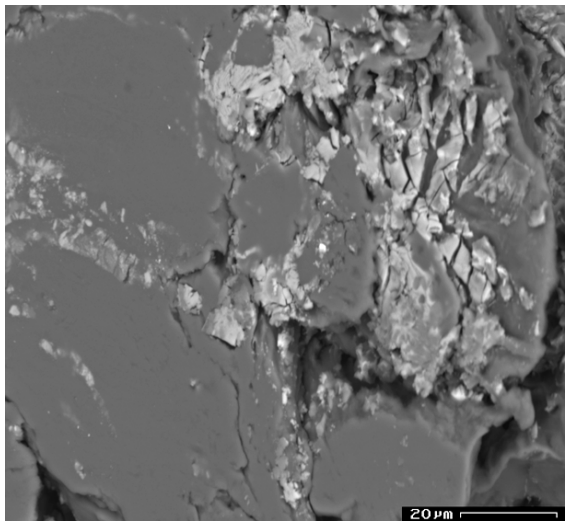

(b) 200°C and 90 MPa, SEM-BSE

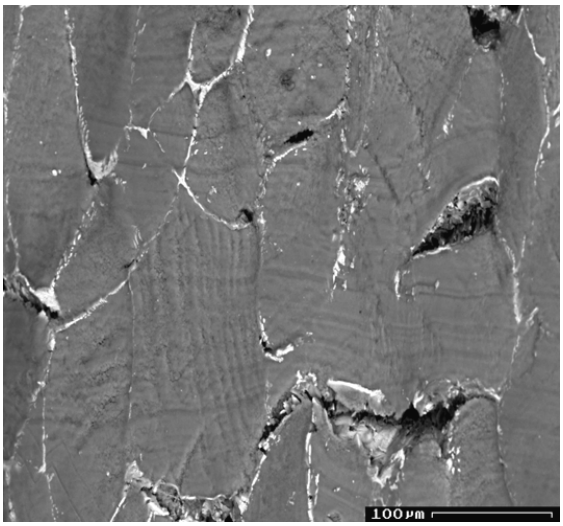

(c) 200°C and 90MPa, SEM-BSE

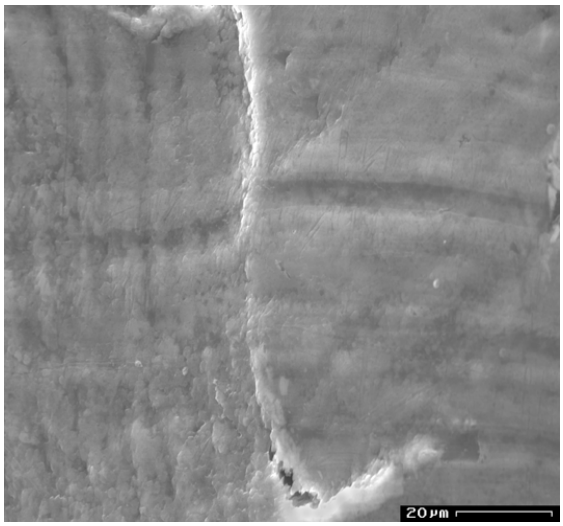

(d) 200°C and 90 MPa, SEM-SE

Fig. 77 : Analysis of the suface of samples of the thixocast ZECa alloy after creep and rupture at 200°C and 90 MPa (tensile direction vertical), SEM-BSE.

The fracture surface analysis of a typically ruptured sample is shown in Fig. 78. In contrast to the fracture at room temperature, grains cannot be clearly identified due to the ductile features overlaying the grain structure, Fig. 78 (a). A closer look at the fracture surface shows dimples of 10-50 µm indicating ductile fracture in the α-Mg phase. The eutectic phase is typically visible only as small islands in the surface, Fig. 78 (b).

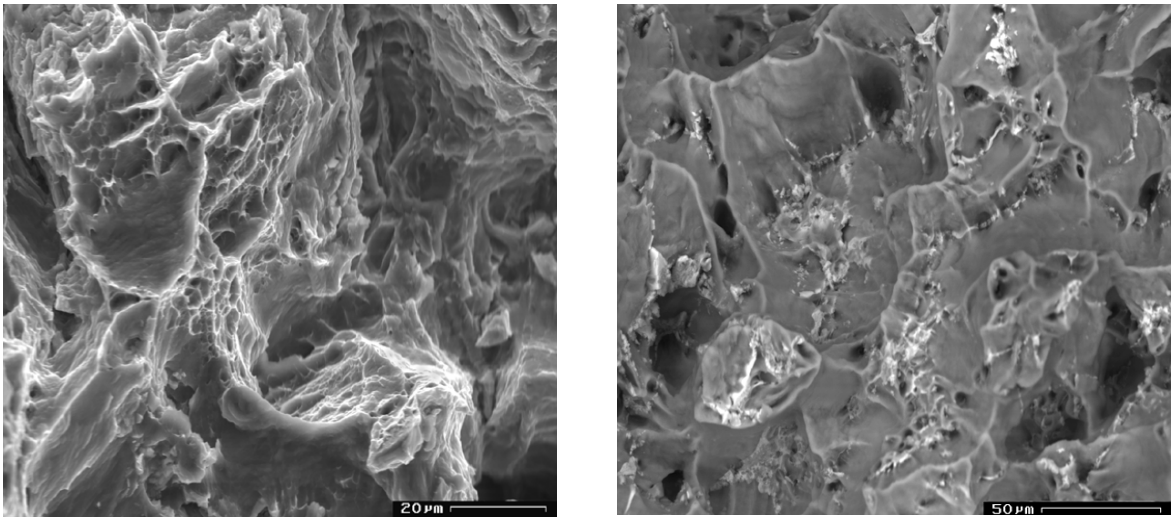

(a) 200°C and 90 MPa, SEM-SE (b) 200°C and 90 MPa, SEM-BSE

Fig. 78 : Analysis of the fracture suface of the thixocast ZECa alloy at 200°C and 90 MPa.

7 DISCUSSION

7.1 Microstructural evolution during processing

The microstructural transformation of the feedstock material during its partial reheating and after thixocasting processing has been presented in former sections. The formation of a globular microstructure during the the semi-solid processing of strained materials is explained and compared with other works.

7.1.1 Extruded feedstock material

The presence of elongated grains in the extrusion direction of the as-received MEZ alloy indicates that the material did not reach a complete dynamic recrystallization after hot working, which is the reason of the bimodal grain shape. Differences on the grain shape are attributed to the non-uniform strain in the alloy during prior deformation. The eutectic phase identified in this alloy has been designated as $Mg_{12}RE$ instead of $Mg_{12}Nd$, phase identified with X-ray diffraction and the powder diffraction file [17-0401], because this phase is a mixture of several rare earth metal atoms which are replacing Nd, being Ce the main alloying element; zinc is also detected in this phase. Therefore, the slightly lower melting temperature observed by DTA (587°C) is a result of the additional elements present in the alloy, which slightly reduce the eutectic temperature (592°C). Since the determined melting point is 645°C, the MEZ alloy has accordingly a relatively narrow solidification and melting temperature, resulting in about 60°C of semi-solid range, which difficult its processing in the semi-solid state. The $Mg_{12}RE$ phase appears fractured in the extrusion direction, indicating the brittle condition of this phase. The zirconium used as grain refiner is found sparingly in the microstructure as Mn_2Zr particles. The matrix of the alloy consists mainly of magnesium, because of the low solubility of Ce and Nd in Mg at low temperatures [92Nay].

The microstructure of the as-received ZECa alloy shows a more homogeneous grain size and shape distribution in the extrusion direction, which is attributed to a complete dynamic recrystallization stage after hot working. Three eutectic phases were identified in this alloy: Mg_2Ca, with some Zn atoms replacing Ca in its structure, $Mg_6Zn_3Ca_2$, with some rare earths atoms replacing Ca/Zn atoms in its structure, and Mg_7Zn, also with some rare earths in its structure. Therefore, the markedly lower phase melting temperatures observed by DTA are, like in the case of the MEZ alloy,

also result of the additional elements present in the phases. The lowest eutectic temperature measured by DTA is 419°C, while the melting temperature is 629°C, resulting in a semi-solid range of about 210°C, which facilitates its semi-solid processing. Strontium has been detected in all the three phases in concentrations up to 3.5 wt. %, but not in the matrix. The only elements present as solid solution in the matrix are Ca, in a low concentration (up to 0.3 wt. %) and Zn, in a higher concentration (up to 1.3 wt. %), which agrees with the solubility of both elements in magnesium [92Cla, 92Nay]. The Mg_2Ca phase appears as elongated particles in the extrusion direction of the alloy, while the ternary phase appears sometimes as fractured particles, indicating that the binary phase is more ductile than the ternary. A fourth unexpected phase, a Zn-Nd-Si type phase, has also been found sparingly distributed heterogeneously in the microstructure. This phase is result of residual SiO_2 proceeding of the mineral monazite, $ZnNd_4(SiO_4)_3O$, which is a mineral rich in rare earths [03Rok] and probably source of the mischmetall used for the production of the ZECa alloy.

The microhardness of the extruded MEZ alloy is with 52 HV10 slightly softer than the ZECa alloy, which is result of the very large grains partially recystallized in the MEZ.

7.1.2 Partial remelting of the extruded material

Upon heating of the extruded feedstock material, the originally small grains of typically 10 µm grow continuously when subjected to increasing temperature, resulting into grains of typically 65 µm in the case of the MEZ alloy and 50 µm in the case of the ZECa alloy. The reheating experiments in chapter 5 show that this grain growth occurs to the largest extend already during heating and within a small soaking time in the order of 5 minutes.

The grain growth starts already in the state where the secondary intermetallic phases are not melted. This is evidenced in the MEZ alloy with a high partial melting temperature of 587°C. Upon heating to 500°C, the original grain size of about 10 µm has increased to about 20 µm, while the ZECa alloy with a first melting onset at 419°C shows the same increase of grain size already when heated to 400°C. This first grain growth is found without any change of the intermetallic phase distribution in the alloys. Grains already recrystallized dynamically in the initial extruded condition are growing without being pinned by the main intermetallic phases. This is in accordance to the generally assumed mechanism of spherodization of the grains,

induced by the mechanically stored energy due to the mechanical treatment, which is in the present case the extrusion.

The mechanism of structural evolution of strained materials during partial remelting is not completely understood. The reason for the structural spheroidizing has been already proposed as the eutectic liquid penetration into the high energy subgrain boundaries formed during recrystalization of the material in the deformation process (extrusion in this case) or the melting of the subgrain boundaries self [02Che2]. The work by this author proved that microstructural spheroidization is induced by prior deformation. The degree of liquid penetration depends on the local balance of surface energies, i.e. on the magnitude of the local grain boundary and solid-liquid surface energy.

However, the major grain growth and the formation of a suitable, globular semi-solid microstructure with the eutectic phase homogeneously distributed around the grain boundaries can only be found at significantly elevated temperatures after further evolution of the microstructure in partially melted state. Partial melting of the secondary phases takes place at temperatures above 587°C for the MEZ alloy and 419°C for the ZECa alloy. The most obvious effect of melting can be observed in the MEZ alloy, where the grain size increases substantially once the eutectic phases is melted-up above the eutectic temperature of the Mg-RE system and the eutectic phase is aligned along the grain boundaries of globular α-grains. This supports the suggestion by Chen et al. [02Che2] that the molten up phase serves as an enhanced, diffusion medium for Mg atoms, resulting in strong spherodisation and growth of the grains, leaving the molten-up phase at the grain boundaries.

In addition to the liquid eutectic in the grain boundaries, also a minor amount of liquified phase is trapped within the grains, thus not contributing to the decrease of viscosity in the semi-solid state. It must be noted that the amount of such entrapped eutectic phase is significantly less than the observed by other authors, [02Che2, 04Kle]. One reason for this positive material behaviour may be the use of extruded material instead of slightly deformed material as was used by Chen et al [02Che2]. The chill cast zinc-aluminium alloy designated by the author as ZA27 was only slightly pressed by a ratio of 20% and therefore not dynamically recrystallized. Additionally, the dendrites microstructure with the corresponding distribution of intermetallic phases was still present in the initial material. According to the author,

small aggregates are formed as a result of recrystallization, which are subsequently agglomerated. Although not stated by the author, entrapping of liquified intermetallic phases must take place during this agglomeration. In contrary, the extruded material in the present work does not lead to the formation of aggregates, thus preventing entrapped intermetallic phases. Additionally, the significantly lower soaking times of only a few minutes used before casting in the present work prevent the agglomeration of grains.

Also Kleiner et al. [04Kle] used dynamically recrystallized extruded material of AZ80 as feedstock, resulting in a very inhomogeneous distribution of liquified phases with a high amount of entrapped liquified phase within the primary grains, disqualifying the material for semi-solid casting. These results were obtained even after very small holding times of 5 min. This unfavourable result is explained only by the lack of microsegregation of the secondary alloy elements, however, the mechanisms of formation of these inhomogeneities remains elusive. A possible explanation is the highly inhomogeneous distribution of intermetallic phases already present in the initial extruded material, demonstrating the importance of the quality of the extruded bars used.

In addition to the processing, also the alloy composition itself may have an influence on the microstructural formation of the semi-solid material. The results of the reheating experiments show that entrapped intermetallic phases are even more efficiently suppressed in the ZECa alloy than already in the MEZ alloy. In contrary to the MEZ alloy, the secondary phases in the ZECa alloy melt up at significantly lower temperatures. Additionally, even after partial melting grain growth is only slightly enhanced by the presence of the liquid phase, which is result of the lower diffusivity of Mg in the Mg-Ca-Zn-containing liquid. The lower grain size decreases the probability of entrapping secondary phases within the grains. Additionally, microsegregation of these phases is enhanced.

7.1.3 Thixocast material

The thixocasting experiments have demonstrated that the chosen processing route of reheating extruded material in the semi-solid range and thixocasting using a squeeze casting equipment leads to castings of low porosity with a relatively homogeneous microstructure in both investigated alloys.

The microstructure of the thixocast material consisted of globular- or rosette-like primary α-Mg grains surrounded with eutectic and secondary α-Mg grains. The formation of spherodized grain boundaries in most of the plates suggests that a suitable thixotropic slurry material was achieved during casting, that the heating temperature was high enough and that the casting parameters, like pressure and piston speed, were, if not optimal, sufficient. Correspondingly, the mould has been completely filled and only a small amount of pores is present.

The difference between the microstructure at the rim and at the core of the stepped plates, particularly for the MEZ alloy, can be explained after the sponge effect model proposed by Kaufmann et. al [08Kau]. A semi-solid slug consists of a solid primary α-phase, which is interconnected three-dimensionally forming a skeleton, and of a liquid phase, which fills the spaces in between. Macrosegregation occurs when the solid skeleton cannot be separated at the beginning of the die filling (i.e. high solid fraction). The solid structure is then compressed like a sponge as a consequence of the deformation (plunger movement) and the liquid phase moves forward into the die cavities. After more deformation, the sponge finally ruptures and the primary phase floats into the die. The sponge effect is strongly shear-rate-dependent (dependent on flow speed, viscosity and geometry of the die) [08Kau]. As a consequence of the sponge effect, the amount of eutectic or intermetallic phases (formerly liquid phase) is higher at the rim than at the core. The phases are homogenously distributed in the microstructure and the finer α-grains tend to be more globular than at the core. The center of the casting consists of rosette- or globular-type α-grains, whose size and form can also be explained by the lower cooling rates in this region. The inhomogeneous distribution of the eutectic phases in the core of the microstructures, resulting in the formation of some agglomerations, is the result of the high mechanical shear forces acting on the semi-solid material during injection into the mould. Additionally, some macro- and meso-segregation caused by tensile stresses as a result of the shrinkage can also contribute to this effect.

The larger α-grains developed in the core of the MEZ castings showed the typical spherodized grain boundaries observed when the material was reheated in its extruded state to higher temperatures or exposed for larger times to high temperature. On the other hand, the microstructure of the rim showed more globular grains as those observed in the reheating experiments when lower temperatures or

lower times of exposure were present. This corresponds to the higher cooling rates at the rim of the sample, leaving less time for temperature exposure.

In addition to the spherodization of the primary α-grains and the alignment of liquefied eutectic phases at the grain boundaries, a change of grain boundaries to spherodized grain boundaries and the formation of new significantly smaller grains are observed within the thixocast material. Similar microstructures can be observed in the literature, but generally lack any explanation of their formation mechanisms.

The reheating experiments in chapter 5 clearly demonstrate that the spherodized grain boundaries are formed only at high temperatures and prolonged times of thermal exposure. The formation of small α-grains surrounding the large primary α-grains is always preceded by the formation of spherodized grain boundaries. After the formation of spherodized grain boundaries, networks of liquid are found at the rim of large primary particles resulting in zones of very small grains. The optical micrographs of the reheated samples, Fig. 21 and Fig. 39, clearly evidence that these small grains have the same orientation as the adjacent large grains. On the other hand, the microstructure of the thixocast material exhibits grains with random orientation. This indicates that change of orientation takes place only in the thixocast process. Therefore the following mechanism of formation of randomly orientated small grains of typically 10 µm is proposed:

- Penetration of liquid in the grain boundaries of large primary particles, resulting in spherodized grain boundaries
- Disintegration of the spherodized grain boundaries by further penetration of liquid and forming of liquid networks
- Change of the orientation of the newly formed grains by the shear forces resulting from the semi-solid flow during the casting process

Due to the lower casting temperature of about 615°C of the ZECa alloy in comparison to 640°C of the MEZ alloy, the formations of such a bimodal microstructure is significantly less pronounced in the ZECa alloy, resulting in a more favourable homogeneous microstructure. Additionally, the lower possible casting temperature due to the lower melting point of the eutectic phases leads to a smaller maximum grain size in the ZECa.

It is known that a larger solidification range may also help the die-castability (elimination of hot tearing and improvement of fluidity) by increasing the length of

time that metal stays liquid [03Pek]. The ZECa alloy has a wider solidification range that the MEZ alloy (ΔT of 210°C vs ΔT of 60°C, respectively), which also explains the more homogeneous shape and size of the castings microstructure.

The microstructural overview showed that the thixocast ZECa alloy has a significantly finer microstructure (up to 100 µm) as compared to the thixocast MEZ alloy (up to 300 µm), corresponding to the lower temperature of melting and to the finer grain sizes developed after the reheating experiments (sizes of about 50 µm for the ZECa alloy compared with the about 65 µm for the MEZ alloy). Another point to consider is that the extruded ZECa alloy had reached an almost complete dynamic recrystallization stage before reheating in the semi-solid state.

Although zinc has a good solid solubility in magnesium (6.2 wt. % at 340°C [92Cla]) it couldn't be detected by means of SEM-EDX in the matrix of the thixocast MEZ alloy, probably because of its low content in the alloy (around 0.5 wt. %). Zinc may nevertheless be present at trace levels, which are difficult to detect by means of a semi-quantitative method, like EDX, but at sufficient level to give the matrix strengthening. Zinc is found replacing some atoms of RE in the $Mg_{12}RE$ eutectic phase. Like in the extruded condition, manganese and zirconium are found combined together forming Mn_2Zr. The effect of Zr as grain refiner cannot be concluded in this work because of the lack of a comparing MEZ alloy with other Zr levels. In any case, the alloy did not show grain refinement after thixocasting.

The eutectic phases already detected in the extruded state were also found in the thixocast ZECa alloy, although the binary Mg-Zn phase changed its stoichiometry, indicating its thermodynamically instability during cooling of the thixocast plates. Strontium was found in the Mg_2Ca and $Mg_6Zn_3Ca_2$ phase (up to 1.2 wt. %). Some zinc was detected in the Mg_2Ca phase, while the rare earths were present in the ternary phase, substituting Ca atoms. The Si-containing phase was also detected sporadically in the thixocast plates, sometimes containing also Fe. Calcium (up to 0.5 wt. %) and zinc (up to 1.8 wt. %) were found in solid solution in the matrix.

7.2 Mechanical properties at room temperature

The mechanism of deformation and fracture of both thixocast alloys MEZ and ZECa are similar. In tension and compression primary and secondary twinning is observed in optical micrographs, which is generally accepted as the first mechanism of

deformation in parallel to dislocation glide on the basal planes [05Bla]. In tensile load, the fracture occurs mainly intercrystalline through the intermetallic phases, which was also observed by Bettles et al. and by Podosek et al. for the MEZ alloy [03Bet, 00Pod] and by Chang et al. for Mg6Zn2Ca1.5Zr [98Cha].

The experimental ZECa alloy shows slightly lower elongation under tensile loads than the MEZ alloy, indicating less ductility. However, the strength of the ZECa alloy is superior to the MEZ alloy in both tension and compression. This fact is consequence of the presence of Ca and Zn in the ZECa alloy, elements that are used to increase strength at room temperature. The strain hardening exponent of the MEZ alloy (0.21) is slightly higher than the exponent of the ZECa alloy (0.16), accordingly with the lower values of strength in tension for the MEZ alloy. In compression, the differences in strength are explained in terms of grains size. The ZECa alloy posses a finer grain size and has therefore higher yield strength.

As is usual for magnesium alloys, for both MEZ and ZECa materials, the elongation and the ultimate strength are significantly higher in compression than in tension because magnesium twins in compression and twinning is used to activate new slip systems [05Agn]. This corresponds to the different fracture mechanism in compression as compared to the tensile load. In compression, crack initiation can be found, as in tensile load, in the intermetallic phase; however, the crack propagates in compression preferably through the α-Mg grains, providing sufficient toughness for further deformation without catastrophic failure.

The further deformation in compression is characterized by the activation of different slip systems as can be concluded from the stress-strain curve. It should be noted here that the activation of non-basal slip systems, usually accepted to be the first deflection in the stress-strain curve, occurs at lower stresses for the MEZ system than for the ZECa alloy. Additionally, the ultimate stress is also lower for the MEZ alloy. Apart from the activation of slip systems a higher extent of recovery and even dynamic recrystallization may also explain the lower strain hardening in the MEZ alloy. This is also corroborated by the observation of severe recrystallization in compression samples, in particular in the MEZ alloy.

The compression curves of the thixocast alloys show the typical shape of magnesium deformed to high strains, with three distinct ranges in the stress-strain curve [05Bla], generally attributed to the subsequent activation of the basal slip and twinning, the

prismatic slip and the pyramidal slip (see explanation in chapter 2). The transition of the two alloys from one range to the subsequent occurs about at the same strain. The stress necessary for the transitions is, as for the tensile case, also in the compressional load higher for the ZECa alloy.

The microstructure after compression at room temperature shows massive twinning, shear bands and dynamic recrystallization. As the deformation during compression is not homogeneous in the material, zones of twinning and shear bands are formed for an optimal orientation of the grains, far and close to the fractured surface respectively. Twinning occurs during initial stages of deformation. The twins have a characteristic lenticular morphology and during subsequent straining, sideways growth of the twinned plates occurs, until twins consume entirely the original grains [82Ion]. On the other hand, shear bands appear when the specimen deforms inhomogenously above a critical strain; one or more shear zones propagate through the specimen, and thereafter plastic flow occurs almost solely within this zones [82Ion]. The appearance of dynamic recrystallization in extremely twinned areas is another feature of deformation. Recrystallization constitutes a recovery mode after deformation and dynamic recovery can take place in Mg alloys during room temperature deformation. Koike et al. [03Koi] founded dynamic recovery in fine grained AZ31 alloys at room temperature at 16% tensile elongation.

7.2.1 Thixocast MEZ alloy

The thixocast MEZ alloy shows reasonable properties as compared to other MEZ alloys produced by competitive methods shown in the literature. Higher tensile yield strength, ultimate tensile strength and elongation than the MEZ alloys produced by gravity casting [03Bet, 00Pod] are observed (Table 14). The strength of the high pressure die cast alloy [03Mor] is slightly higher than the strength of the thixocast alloy of this work, which can be a result of the higher cooling rates occurring during HPDC. Higher cooling rates lead to smaller grain size, which is confirmed by the results: micrographs in [03Mor] show that the grain size is around 30 µm, while a typical grain found in this investigation is around 200µm. Another point to be considered is that in the present work, all mechanical properties have been measured on machined specimens, where the casting skin has been removed. Sequeira [00Seq] investigated the effect of skin removal on flat die-casting tensile specimens of AZ91D. He found that specimens with skin have better yield strength

than specimens without skin, indicating that the casting skin is partially responsible for the better tensile properties. The casting surface has a finer solidified microstructure and higher micro hardness than the core, where coarser grains and micro porosity are present, as described by Yang et al. in AZ91D and in Mg-3%La [10Yan, 10Yan2]. In addition to the hardening effect of smaller grains (Hall-Petch effect), a stronger precipitation hardening effect due to higher quench rates might be another reason for the slightly higher strength in the HPDC material. Accordingly, the elongation of the thixocast alloy is higher than for the HPDC alloy. This could be explained by the higher ductility due to less effective hardening precipitates. The fracture analysis, however, shows that the main failure mechanism is intergranular fracture. This was observed in the present work in accordance with [03Bet] et al. and [00Pod] et al. Therefore, also the relatively homogeneous distribution of intermetallic phases as observed in this investigation may contribute to the good ductility.

Table 14 : Tensile properties of MEZ alloys in the as-cast state at room temperature.

Material	0.2% TYS (MPa)	UTS (MPa)	% elongation
MEZ HPDC [03Mor]	97.6	134.8	2.9
MEZ gravity cast [03Bet]	62±3	100±2	2.8
MEZ conventional casting [00Pod]	67	130	3.5
MEZ thixocast – this work	75.5 ± 10.1	124.7 ± 12.5	3.7 ± 1.3

7.2.2 Thixocast ZECa alloy

A direct comparison to Mg-Ca-Zn alloy with literature is not possible due to a lack of data in that field. Chang et al. [98Cha] (see Table 15) investigated the tensile properties of Mg6Zn2Ca1.5Zr in squeeze casting and a process designated as semi-solid squeeze casting and found significantly higher strength for the squeeze cast material, while lower strength for the reheated semisolid processed material. The higher strength of the squeeze cast material produced by Chang et al. can be explained by the higher amount of strengthening phases. In addition, the grain size is about 25µm. It should however be noted that only a cylinder was produced during

squeeze casting. Casting of small flat parts as in the present investigation was not demonstrated.

Despite the high fraction of strengthening elements in the alloys used by Chang et al. [98Cha], the tensile yield strength is lower than on the ZECa material produced in the present investigation. The semi-solid squeeze casting process of Chang et al. is characterized by applying a subsequent reheating and pressing of the initial cylinder, resulting in rather inhomogeneous microstructure and significant grain growth. The comparable grain size, estimated by micrographs, as in the present work, obviously leads to slightly lower yield strength. The higher yield strength of this investigation may also be a result of the higher solidification rates present during casting as compared to mere cooling of a bulky cylinder.

The tensile yield strength almost reaches the value of the state of the art alloys with high temperature resistance as AE42 (see Table 15). The ultimate tensile strength and the elongation of AE42 are significantly higher. This might be due to the lower grain size of the typical die cast AE42 alloys, which amounts to be about 10 µm, as concluded from a micrograph in [94Luo]. The smaller grain size can result in a higher ductility due to smaller dimensions of the intermetallic phase at the grain boundary and thus increase also the ultimate strength. However, it should be noted that a typical AE42 die cast material shows typically a high amount of microporosity, which can result in crack formation by expanding gas upon further heat treatment or welding. The negligible amount of microporosity in the thixocast material should be noted as an advantage for further processing.

Table 15 : Tensile properties of Mg-Zn-Ca alloys in the as-cast state at room temperature.

Material	0.2%TYS (MPa)	UTS (MPa)	% elongation
Mg6Zn2Ca1.5Zr squeeze casting[98Cha]	~130	~175	~3
Mg6Zn2Ca1.5Zr semi-solid squeeze casting [98Cha]	83	170	~6
ZECa (Mg3Zn3Ca1RE) thixocast - this work-	91.6 ± 5.6	125.9± 6.0	2.4 ± 0.5
AE42, die cast [03Mor]	113	194	7.3
AE42, die cast [94Luo]	110	244	17

7.3 Determination of the stress exponent and activation energy

7.3.1 Creep rate analysis of the thixocast MEZ alloy

The total creep strain of the thixocast MEZ alloy after 10 hours of testing is presented in Table 16. The values in this table show the effect of the primary creep, which develops during the first minutes of testing. The minimum creep rates of the thixocast MEZ alloy are listed in Table 17.

The relationship between the secondary creep rate and the stress is shown for all temperatures in Fig. 79. The experimental results show a reasonable fit to a straight line with the stress exponent very close to 4. The value of the stress exponent n calculated after fitting the points in Fig. 79 varies between 3.9 and 4.3.

The temperature dependence is shown in Fig. 80. In the determination of the activation energy of creep for the MEZ alloy, two stages are clearly delimited. The first one includes temperatures up to 175°C and has a value of 80-89 kJ/mol, which is close to the value of grain boundary diffusion (80 kJ/mol) and is also close to the value for dislocation pipe diffusion of ~92 kJ/mol [98Reg]. The second region comprises temperatures higher than 175°C and up to the studied temperature range of 200°C. This value is significantly higher, ranging from about 195-210 kJ/mol.

Table 16 : Total creep strain of the MEZ alloy after 10 hours of creep testing.

MEZ	135°C	150°C	175°C	200°C
50 MPa	0.0019	0.0028	0.0035	0.0041
60 MPa	0.008	0.0038	0.0063	0.0087
70 MPa	0.0097	0.0136	0.0119	0.0114
80 MPa	0.018	0.017	0.0186	0.0313
90 MPa	0.039	0.044	0.0339	0.0537
100 MPa	0.050	0.048	0.070	0.055

Table 17 : Minimum creep rates of the MEZ alloy.

MEZ	135°C	150°C	175°C	200°C
50 MPa	5.59E-11	1.65E-10	4.91E-10	8.8E-9
60 MPa	1.16E-10	3.33E-10	1.05E-9	1.8E-8
70 MPa	2.11E-10	6.01E-10	1.92E-9	3.22E-8
80 MPa	3.12E-10	9.34E-10	3.38E-9	6.52E-8
90 MPa	5.4E-10	1.57E-9	5.96E-9	1.29E-7
100 MPa	9E-10	2.54E-9	9.98E-9	2.1E-7

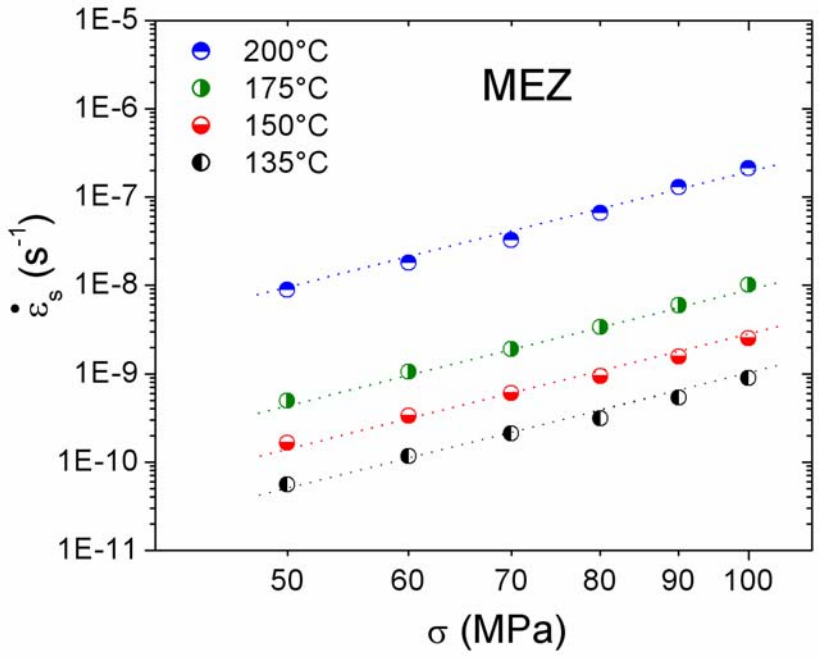

Fig. 79 : Creep rates versus stresses at different temperatures for the thixocast MEZ alloy (double logarithmic scale). Straight lines indicate the fit for the determination of the stress exponent.

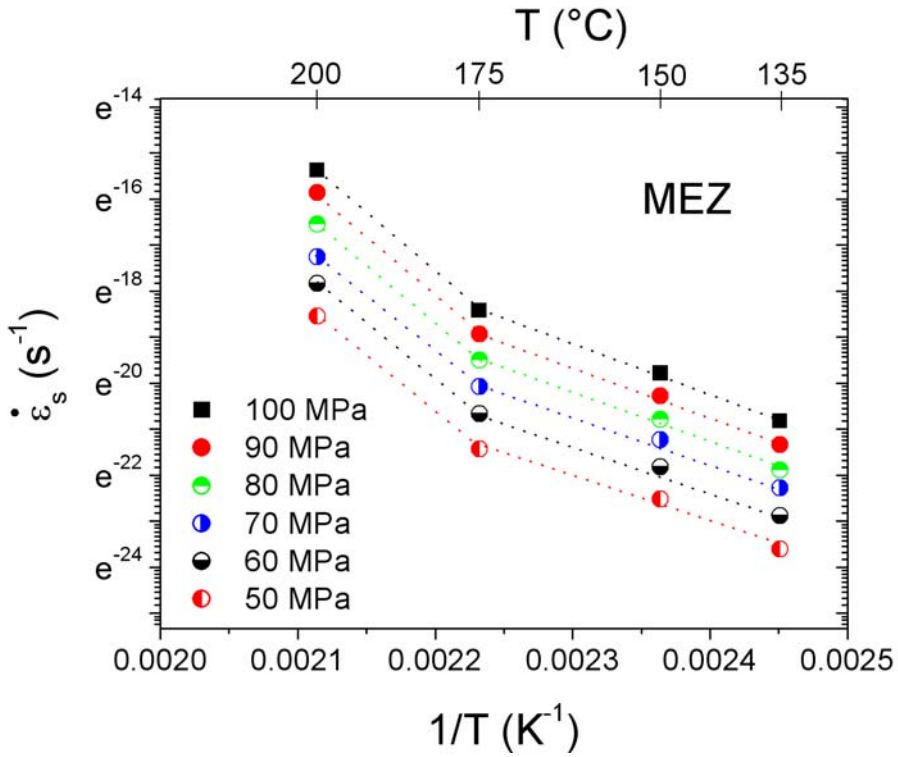

Fig. 80 : Creep rates versus 1/T at different stresses for the thixocast MEZ alloy (logarithmic scale). Straight lines indicate the fit for the determination of the activation energy.

7.3.2 Creep rate analysis of the thixocast ZECa alloy

The total creep strain of the thixocast ZECa alloy after 10 hours of testing is presented in Table 18, which gives information of the primary creep of the alloy. The minimum creep rates of the thixocast ZECa alloy are listed in Table 19.

Table 18 : Total creep strain of the ZECa alloy after 10 hours.

ZECa	135°C	150°C	175°C	200°C
50 MPa	0.0016	0.0013	0.0020	0.0019
60 MPa	0.0017	0.0023	0.0023	0.0049
70 MPa	0.0027	0.0053	0.0035	0.0072
80 MPa	0.0040	0.0059	0.0078	0.010
90 MPa	0.0070	0.0077	0.046	0.021
100 MPa	0.0170	0.0108	0.020	0.029

Table 19 : Minimum creep rates of the ZECa alloy.

ZECa	135°C	150°C	175°C	200°C
50 MPa	6.2E-11	2.62E-10	1.46E-9	7.9E-9
60 MPa	1.36E-10	6.45E-10	3.27E-9	1.98E-8
70 MPa	2.7E-10	1.37E-9	8.2E-9	6.84E-8
80 MPa	5.71E-10	3.05E-9	2.4E-8	1.15E-7
90 MPa	1.2E-9	5.78E-9	4.74E-8	2.45E-7
100 MPa	2.96E-9	1.18E-8	1.2E-7	4.92E-7

In the ZECa alloy the creep rates increase exponentially with the stress, fulfilling the exponential law in the creep equation as can be seen in the linear dependence in the double logarithmic diagram (Fig. 81). As in the MEZ alloy, no significant difference in the exponential law can be detected between the temperatures, indicating that the stress exponent is independent of temperature and stress. Fitting of points give a stress exponent between 5.5 and 6.4.

Creep rate also increases exponentially with 1/T fulfilling the Arrhenius equation, as can be seen by the linear dependence in the plot of the logarithmic strain rate versus 1/T (Fig. 82). In contrast to the MEZ alloy, no significant increase of the slope, i.e. the activation energy, can be detected for the ZECa alloy. The evaluation of the activation energy from the plot yields values between 115-125 kJ/mol (average of 122 kJ/mol). This value is very close to the activation energy for the self diffusion in magnesium (134 kJ/mol). For the tested temperature (135–200°C), the activation energy value of 115-125 kJ/mol of the ZECa alloy is corresponding to 125 kJ/mol measured for high-temperature creep of pure Mg. It is also in the range of 92–135 kJ/mol reported for the activation energy for dislocation glide in basal planes in pure Mg which is also the self diffusion activation energy in the Mg lattice [88Die]. In addition, Luo et al. [01Luo] have measured Q ~ 120 kJ/ mol for AC53 at 83 MPa. These results suggest that the rate determining creep mechanism is dislocation glide with an activation energy of 115-125 kJ/mol. The value of the stress exponent at these temperatures suggests that dislocation climb is the rate controlling process.

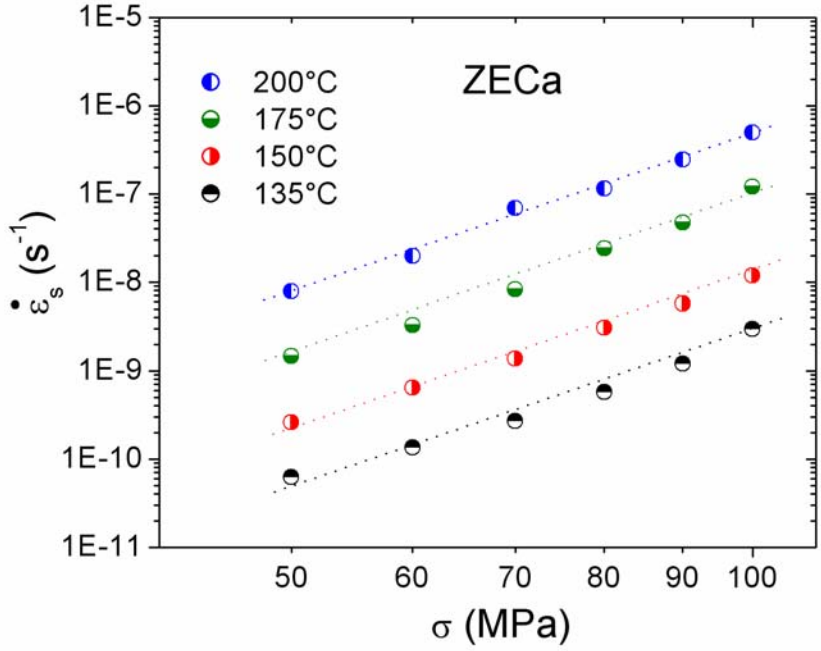

Fig. 81 : Creep rates versus stress at different temperatures for the thixocast ZECa alloy (double logarithmic scale). Straight lines indicate the fit for the determination of the stress exponent.

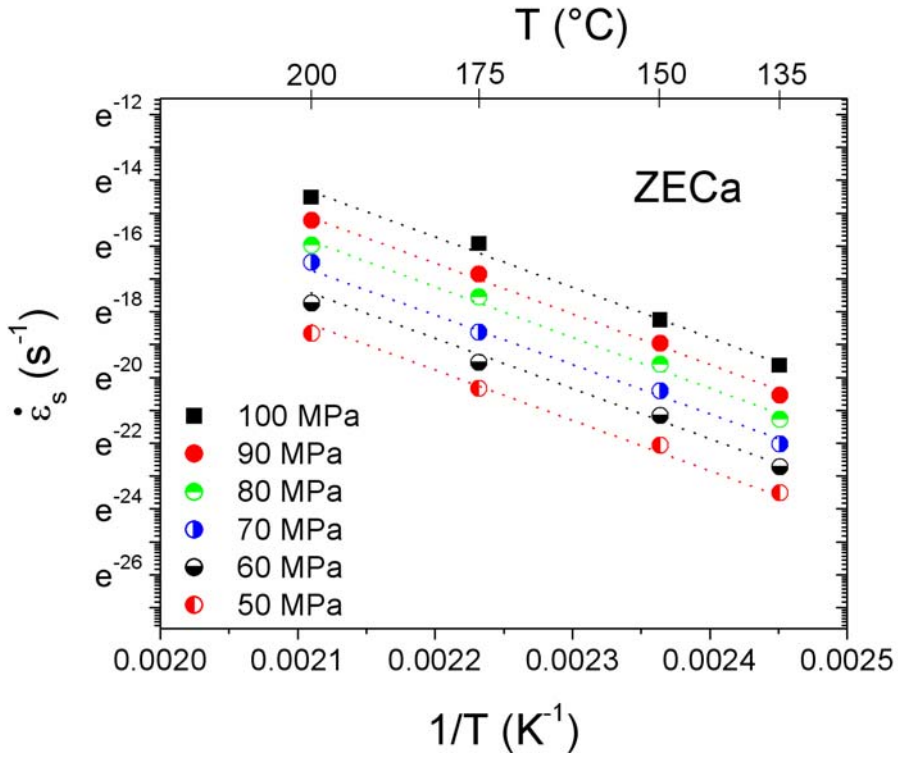

Fig. 82 : Creep rates versus 1/T at different stresses for the thixocast ZECa alloy (logarithmic scale). Straight lines indicate the fit for the determination of the activation energy.

7.4 Creep mechanisms

According to the intact microstructure obtained by the thixocasting process, reasonable creep properties could be evidenced in the two alloys. Fig. 83 gives a comparison to state of the art alloy AE42 as well as to the MEZ alloy both processed by high pressure die casting. It shows the superior creep behaviour of the MEZ alloy as well as the ZECa alloy as compared to the AE42 alloy in the die cast condition.

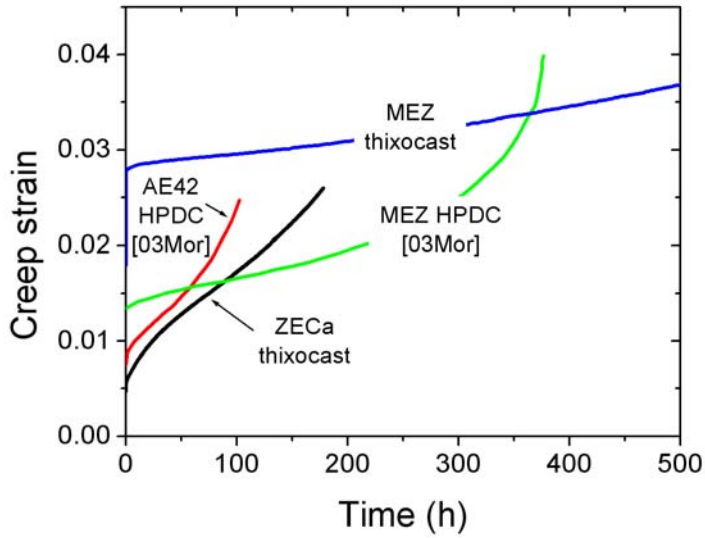

Fig. 83 : Comparison of creep strain vs. time of the thixocast MEZ and ZECa alloy of this work with MEZ HPDC and AE42 HPDC alloys characterized by Moreno et al. [03Mor] at 175°C and 80 MPa.

7.4.1 Creep of the thixocast MEZ alloy

A direct comparison between the MEZ thixocast alloy obtained from extruded bars and the MEZ HPDC shows a significantly later onset of the tertiary creep in the MEZ alloy of this investigation. The early onset of the tertiary creep observed by Moreno et al. goes along with a drastic increase of the stress exponent with higher stresses from 6-7 at 50-60 MPa to 37-44 at 70-100 MPa [03Mor]. Both phenomena are usually associated with failure mechanisms such as void and wedge formation at grain boundaries, originating from pores or accumulation of secondary phases. This demonstrates the superior mechanical properties of the material processed by thixocasting from extruded material.

On the other hand, a significantly higher initial primary creep can be observed in the MEZ material from this investigation than in the HPDC material produced by Moreno et al. This higher initial primary creep coincides with the lower yield strength of the

thixocast alloy. It can be assumed that the yield stress at 175°C is already below the applied stress of 80 MPa, resulting in yielding upon heating. To increase the maximum applicable stress for this material an aging treatment could be applied, because an aging response was noted in the hardness measurements upon temperature exposure. An increase in the yield strength could be achieved by decreasing the grain size, e.g. more rapid solidification with increase injection times or further optimization of the reheating step.

The lower creep rates in the secondary creep range observed for the MEZ thixocast alloy of the present investigation shows that the significantly finer grain size of the HPDC alloy (see Table 20) does obviously not improve the creep properties. It should be noted that a high amount of recovery and also recrystallization at these high temperatures can occur. At slightly higher temperatures of 200°C severe recrystallization could be evidenced by optical microscopy and TEM in crept material. A hardening due to accumulation of dislocations on grain boundaries as necessary for the Hall-Petch effect can thus not occur.

Another factor that makes the creep rate independent of the grain size is that grain boundary sliding obviously not occurs in the MEZ alloy. No relative movement of grains was observed for the MEZ alloy, even up to 200°C as this was observed for the ZECa. In accordance, Moreno et al. [03Mor] reports that no change of grain boundaries was observed in crept samples up to the investigated range of 175°C.

These observations are in line with the observation that even at 200 h, in most cases, no tertiary creep was observed in the thixocast MEZ alloy. It seems that the clear tertiary creep observed in the sample crept at 200°C and 90 MPa was an exception, where the observed detachments of grain boundaries are probably the result of a locally imperfect initial microstructure, e.g. due to small pores or inhomogeneously distributed intermetallic phase.

Slight changes during secondary creep also indicate further influences of the microstructure of thixocast alloy on the creep behaviour. The slight decrease of creep rates during secondary creep at temperatures up to 175°C can be explained by an additional precipitation hardening, which was also observed under thermal exposure up to this temperature. Accordingly, the slight increase of creep rate at the beginning of secondary creep at 200°C may be a result of thermal softening. This can be caused by an overaging effect at this temperature, which is supported by the

decreasing hardness in the temperature exposure experiments and by the observation of larger precipitates, preferably at sub-grain boundaries, which were observed in optical microscopy and TEM. Additionally, at 200°C the crept samples show extensive recrystallization, which also could be clearly evidenced by optical microscopy and TEM. This recrystallization can additionally cause thermal softening. Twinning can initiate dynamic recrystallization in early stages of plastic deformation, as concluded by recent works [01Gal, 02Mys, 03Sit]. Moreover, Sitdikov et al. [03Sit] have proposed the following mechanism of dynamic recrystallization in coarse grained Mg: (1) the formation of dynamic recrystallized nuclei results from the mutual intrersections of deformed twins, (2) the twin boundaries convert then into random boundaries of high strain due to their interaction with mobile dislocations, and (3) the new grains formed are in non-equilibrium and exhibit almost rectangular shape.

Table 20 : Comparison of achieved grain sizes and creep analysis for MEZ materials and further alloys from literature and in the present investigation.

Alloy **Casting process**	**Grain size**	**Temperature (°C)**	**Stress (MPa)**	**Q (kJ/mol)**	**n**	**Reference**
Sand cast	290 µm	150 and 177	35 and 46	147	~0	[00Bet]
HPDC (cold chamber)	30 µm[2)]	150 and 175	50-100	n.a.	6-7 (37-44)	[03Mor] [01Mor]
Thixocast[1)]	150 µm	135-175	50-100	80-89	3.9-4.3	This work
Thixocast[1)]	150 µm	175-200	50-100	195-210	3.9-4.3	This work

1) thixocast from extruded material using squeeze cast process

2) as estimated from micrograph [01Mor]

However, all these small changes in the secondary creep rate do not explain the strong increase of minimum creep rates between 175°C and 200°C. The analysis of the minimum creep rate shows that between these temperatures a significant change in the creep mechanism occurs. At temperatures up to 175°C, an activation energy of 80-89 kJ / mol and a stress exponent of 3.9 – 4.3 could be deduced. An activation energy of 81-135 kJ / mol is in general attributed to the lattice self diffusion for

magnesium and its solid solutions [82Vag]. The self diffusion corresponds to the mechanism of dislocation climb on the basal plane. For this mechanism a stress exponent of 5.5 is analytically deduced and is also measured by Tegart et al. on pure magnesium [61Teg]. However, also slightly deviating stress exponents were measured and could be attributed to dislocation glide on the basal plane of magnesium and the corresponding dislocation climb as rate limiting step.

At temperatures higher than 175 °C the activation energy changes abruptly to 195-210 kJ/mol. Such a change of activation energy from 117 to 218 kJ / mol was also observed by Tegart et al. (associated with a slight change of the stress exponent from 5.5 and 4) for pure magnesium and could be attributed to the change of creep mechanism from dislocation climb on the basal plane to cross slip from basal to prismatic planes [61Teg]. However, this change of mechanism is observed at the significantly higher temperature of 277°C.

In accordance to the typical change in activation energy observed when cross slip is activated at a certain temperature, above 175°C cross-slip could be evidenced for the thixocast MEZ of this investigation in TEM by dislocation orientations in two preferred directions. This change of mechanism explains the strong increase of creep rate at temperatures above 175°C and limits the applicability of the alloy at temperatures above 175°C.

7.4.2 Creep of the thixocast ZECa alloy

Due to the lower strain hardening of the ZECa alloy, the primary creep of this alloy is lower than the primary creep of the MEZ alloy (see Tables 16 and 18). Despite this difference, some microstructural characteristics of the crept samples are similar in the ZECa thixocast material as compared to the MEZ thixocast material. Primary and secondary twinning can be observed even at low stresses and low temperatures, indicating the first steps of deformation. Under further load intermetallic phases break at the grain boundaries in order to accommodate the deformation of the primary grains as in the MEZ alloy. The ternary eutectic $Mg_6Zn_3Ca_2$ shows more signs of deformation and fracture than the binary Mg_2Ca phase. Additionally, the results of reheating the extruded material into the semi-solid state showed that the ternary phase melts before than the binary phase, indicating that the ternary phase is the low melting eutectic responsible for the grain boundary sliding of the crept samples at higher temperatures. Furthermore, as in the MEZ alloy, at 200°C the crept samples

showed extensive recrystallization at high stresses. As indicated before, dynamic recrystallization can cause thermal softening of the material, allowing extended deformation before failure.

The evaluation of the activation energy from the plot yields values between 115-125 kJ/mol (average of 122 kJ/mol). This value is very close to the activation energy for the self diffusion in magnesium (134 kJ/mol). It is also in the range of 92–135 kJ/mol reported for the activation energy for dislocation glide in basal planes in pure Mg [88Die], suggesting that dislocation climb is also the rate determining step in the ZECa alloy. This is also supported by the measured stress exponent of 5.5 - 6.4. Theses stress exponents agree very well to the stress exponents of 6.2 and 7.2 measured at 150°C at a similar stress range by Gao et al. [05Gao] on Mg1Ca1Zn0.6Zr and Mg1Ca1Zn1Nd0.6Zr, respectively (see Table 21). Although cross slip could be evidenced by cross slip lines in fracture surfaces of the crept samples, the rate limiting step for secondary creep is obviously dislocation climb on the basal plane up to the investigated range of 200°C and 100 MPa.

Increased creep rates were however observed in connection with tertiary creep at 175°C for higher stresses 90 MPa and at 200°C within the investigated time range of 200 h. Accordingly Gao et al. [05Gao] did observe tertiary creep at 175°C and 90 MPa even for significantly smaller amounts of hardening alloy elements and in T6 condition. This onset of tertiary creep might be attributed to overaging effects of the hardening phases. However, the temperature exposure experiments conducted in chapter 6.2.2.2 did not show thermal softening of the alloy up to 175°C within the investigated time range of 200 h for creep. This also corresponds to the thermal exposure experiments conducted by Finkel et al. [02Fin, 03Fin] and by Zilberov et al. [04Zil], which did not observed significant thermal softening up to 200°C and temperature exposure times up to 40 days.

However, it was also observed e.g. by Finkel et al. [02Fin, 03Fin] that even at 160°C and 40 days diffusion of elements from the grain interior to the grain boundaries has occurred, indicating that grain boundaries are prone to diffusion processes even at low temperatures. In accordance the microstructure of crept samples showed clear signs of grain bounday sliding for the ZECa thixocast material after creep. It has to be noted that melting of the $Mg_6Zn_3Ca_2$ (τ_1-phase) was observed already at 419°C in DTA experiments in chapter 5. The equilibrium stability of the τ_1-phase was even

calculated to be only up to 350°C, with a decreasing amount of thermodynamically stable phase already at significantly lower temperatures [04Zil, 06Lev]. Therefore, it has to be assumed that the application temperatures of the Mg-Ca-Zn alloys are in general limited by the low stablity of the τ_1-phase.

Table 21 : Summary of creep analysis from magnesium-calcium-zinc alloys in comparison to the thixocast ZECa alloy of this investigation.

Alloy **Casting process**	**Temperature (°C)**	**Stress (MPa)**	**n**	**Q (kJ/mol)**	**Reference**
Mg-3Zn-1Ca-1.5Ce-0.5La, planar flow casting (rapid solidification)	200 250	< ~ 85 > ~ 85	2-3 ~ 7	185 135	[96Čad] [96Šus]
Mg1Ca1Zn0.6Zr, gravity cast, T6 condition	150	70-120	6.2	n.a	[05Gao]
Mg1Ca1Zn1Nd0.6Zr processed as above	150	90-120	7.2	n.a	[05Gao]
ZECa, thixocast	135-200	50-100	5.5-6.4	115-125	This work

8 CONCLUSIONS

This work has shown that aluminium-free, zinc containing magnesium alloys can be processed in the semi-solid state as an alternative to die-casting. The thixocasting process, using extruded feedstock material reheated for short time in the semi-solid state and subsequently squeeze cast, has proven feasibility for producing relatively fine grained casts of magnesium-zinc alloys with low porosity. A key parameter in this process, in particular for the grain size and grain shape distribution after semi-solid processing, has been identified as the time and temperature of the reheating step.

The succesful use of extruded alloys as feedstock material for thixocasting processes has been demonstrated. The present work has shown that a correct reheating step selection is enough to originate spheroidized grain boundaries in the semi-solid state of magnesium-zinc alloys. The microstructural evolution of the extruded materials and its underlying mechanisms upon reheating have been carefully analysed in order to establish a basis for the effective process optimization for Mg-Zn alloys.

The two investigated thixocast aluminium-free, zinc-containing magnesium alloys showed better creep properties than the state of the art AE42 alloy after 100 h of creep exposure up to 175°C and 80 MPa. The characterization of the creep behaviour has shown that an early onset of a tertiary creep due to casting defects - as observed in former investigations - could be avoided in the thixocast alloys.

The creep mechanisms of the thixocast materials have been analysed in detail in order to evaluate the limits of application and to establish a basis for further alloy optimisation. The general rate determining step for creep in the MEZ alloy could be identified as dislocation climb on the basal plane for temperatures below 175°C and as cross slip from basal to the prismatic plane for temperatures above 175°C. Due to the good quality of the cast, the material was highly resistant to tertiary creep up to temperatures of 200°C. Nevertheless, rapidly increasing secondary creep rates above 175°C limit the application to this temperature. Another drawback is the relatively low yield strength at room temperature, which could be increased by decreasing the grain size, e.g. by more rapid solidification or further optimization of the reheating step. For long application times of the material it has to be noted that thermal softening, probably due to overaging effects, was noted at relatively short exposure times at high temperatures.

The creep mechanism of the ZECa remains to be dislocation climb on the basal plane as the rate limiting factor for secondary creep up to the investigated temperature of 200°C. An application is promising up to about 175°C and about 80 MPa, above which tertiary creep sets in already before 200 h. This could be attributed to grain boundary sliding, induced by thermal softening of the ternary $Mg_6Zn_3Ca_2$ phase, mainly evolving in this alloy. Even though the MEZ alloy shows lower minimal creep rates than the ZECa alloy, the higher values of primary creep of the MEZ alloy, due to the strain hardening effect, make of the ZECa alloy a promissory material where initial loading plays an important role, like in the case of bolted connections in power train components. Additionally, the yield strength of the ZECa alloy is almost comparable to the state of the art alloys such as AE42, thus providing a reasonable alternative for diecast AE42 with improved creep resistance.

The thixocasting process used in this work achieved a bimodal microstructure in the castings, which consisted of larger primary α-grains of spheroidized grain boundaries surrounded by many smaller secondary α-grains, with the eutectic phases distributed homogeneously around both grain types. Although some microstructural variations were found at the different thicknesses of the thixocast plates (grain size and grain shape), especially in the MEZ alloy, a logical sequence for the minimal creep rate was obtained, fact that permitted the determination of the creep parameters. It can be concluded then that the creep behaviour was not detrimentally affected by the shape or the size of the α-Mg grains and that the achievement of better thixocast microstructures through better process parameters may even increase the creep resistance of the alloys. The creep resistance was mainly determined by the bimodal microstructure of the thixocasting. Smaller secondary α-grains delay the onset of grain movement by grain boundary sliding. In the case of thermally stable eutectic phases at the grain boundaries, like in the MEZ alloy, grain boundary sliding can even be hindered. The grain deformation relies thus on the effect of solute elements in the matrix that cause precipitation strengthening (zinc) or cause decreasing of the stacking fault energy (rare earths). This is a promissory result for the casting of complex parts in automotive applications, with thicker and thinner walls. Nevertheless, it has been shown that microstructural variation does have an effect on the mechanical properties at room temperature and therefore, it is important to control it selecting correct casting parameters.

9 BIBLIOGRAPHY

[53Mel] Mellor, G.A.; Ridley, R.W.: "Creep at 250°C and 300°C of some magnesium alloys containing cerium", Journal Inst. Metals **81** (1953) 245-253

[61Teg] Tegart, W.J. McG.: “Activation energies for high temperature creep of polycrystaline magnesium”, Acta Metallurgica **9** (1961) 614-617

[63Jon] Jones, R.B.; Harris, J.E.: Proceedings of the Joint International Conference on Creep, Vol. 1, The Institution of Mechanical Engineers, London (1963)

[64Teg] Tegart, W.J. McG.: “Independent slip systems and ductility of hexagonal polycrystals”, Philosophical Magazine **9** (98) (1964) 339-341

[65Jon] Jones, R.B.: “Difussion creep in polycrystalline magnesium”, Nature **207** (1965) 70

[66Eml] Emley, E.F.: *Principles of Magnesium Technology*, Pergamon Press, Oxford (1966)

[67Par] Partridge, P.G.: “The crystallography and deformation modes of hexagonal close-packed metals” , Metallurgical Reviews **118** (12) (1967) 169-194

[70Mil] Milička, K.; Čadek, J.; Ryš, P.: “High temperature creep mechanismus in magnesium”, Acta Metallurgica **18** (10) (1970) 1071-1082

[72Cro] Crossland, I.G.; Jones, R.B.: “Dislocation creep in magnesium”, Metal Science Journal **6** (1972) 162-166

[72Spe] Spencer, D.B.; Mehrabian, R.; Flemings, M.C.: “Rheological behaviour of Sn-15% Pb in crystallization range”, Metallurgical Transactions **3** (1972) 1925

[76Fle] Flemings, M.C.; Riek, R.G.; Young K.P.: “Rheocasting”, Materials Science and Engineering **25** (1976) 103-117

[77Cro] Crossland, I.G.; Jones, R.B.: “Grain boundary diffusion creep in magnesium”, Metal Science **11** (11) (1977) 504-508

[81Vag] Vagarali, S.S.; Langdom, T.G.: “Deformation mechanisms in H.C.P. metals at elevated temperatures (I): Creep behaviour of magnesium”, Acta metallurgica **29** (1981) 1969-1982

[81Yoo] Yoo, M.H.: “Slip, twinning, and fracture in hexagonal close-packed metals”, Metallurgical Transactions **12A** (1981) 409-418

[82Ion] Ion, S.E.; Humphreys, F.J.; White, S.H.: “Dynamic recrystallisation and the development of microstructure during the high temperature deformation of magnesium”, Acta metallurgica **30** (1982) 1909-1919

[82Vag] Vagarali, S.S.; Langdom, T.G.: “Deformation mechanisms in H.C.P. metals at elevated temperatures (II): Creep behaviour of a Mg - 0.8 % Al solid solution alloy”, Acta metallurgica **30** (1982) 1157-1170

[84Doh] Doherty, R.D.; Lee, Ho-In; Feest, E.A.: “Microstructure of stir-cast metals”, Materials Science and Engineering **65** (1984) 181-189

[84Hon] Honeycombe R.W.K.: *The plastic deformation of metals*, second edition, Edward Arnold Ltd, London (1984)

[88Die] Dieter, George E.: *Mechanical Metallurgy*, SI Metric edition, McGraw-Hill Book Company (1988)

[89Uns] Unsworth, W.: “The role of rare earth element in the development of magnesium base alloys”, International Journal of Materials and Product Technology **4** (4) (1989) 359-378

[91Fle] Flemings, M.C.: “Behaviour of metal alloys in the semisolid state”, Metallurgical Transactions **22A** (5) (1991) 957-981

[92Cla] Clark, J.B.; Zabdyr, L.; Moser, Z.: “Mg-Zn” in *Binary alloys phase diagrams*, edited by T.B. Massalski, H. Okamoto, P.R. Subramanian and L. Kacprzak, Materials Park, Oh, ASM International (1992) pp. 2571

[92Nay] Nayeb-Hashemi, A.A.; Clark, J.B.: “Ca-Mg”, “Ce-Mg”, “La-Mg”, “Mg-Nd”, “Mg-Pr” in *Binary alloys phase diagrams*, edited by T.B. Massalski, H. Okamoto, P.R. Subramanian and L. Kacprzak, Materials Park, Oh, ASM International (1992) pp. 925, 1077, 2400, 2527, 2537

[93Bro] Brown, S.; Flemings, M.C.: “Net-shape forming via semi-solid processing”, Advanced Materials and Processes **1** (1993) 3640

[93Eva] Evans, R.W.; Wilshire, B.: *Introduction to creep*, The Institute of Materials, London (1993) Ch. 5, 6

[94Luo] Luo, A.; Pekguleryuz, M.O.: “Review: cast magnesium alloys for elevated temperature applications”, Journal of Materials Science 29 (1994) 5259-5271

[94Miy] Miyazaki, T.; Kaneko, J.; Sugamata, M.; “Structures and properties of rapidly solidified Mg-Ca based alloys”, Materials Science and Engineering **A181/A182** (1994) 1410-1414

[95Nav] Nabarro, F.R.N.; de Villiers, H.L.: *The physics of creep*, Taylor and Francis, London (1995) Ch. 3

[95Pol] Polmear, I.J.: *Light Alloys: Metallurgy of the light metals*, Arnold, London (1995) Chapters 4 and 5

[96Čad] Čadek, J.; Šustek, V.; Kloc, L.; Evangelista, E.: "Threshold creep behaviour of an Mg-Zn-Ca-Ce-La alloy processed by rapid solidification", Materials Science and Engineering **A215** (1-2) (1996) 73-83

[96Šus] Šustek, V.; Spigarelli, S.; Čadek, J.: "Creep behaviour at high stresses of an Mg-Zn-Ca-Ce-La alloy processed by rapid solidification", Scripta Materialia **35** (3) (1996) 449-454

[96Lan] Langdon, T.: "Transitions in creep behaviour", Materials Transactions, JIM, **37** (3) (1996) 359-362

[97Hum] Humble, P.: "Towards a cheap creep resistant magnesium alloy", Materials Forum **21** (1997) 45-56

[97Nie] Nie, J.F.; Muddle, B.C.: "Precipitation hardening of Mg-Ca(-Zn) alloys", Scripta Materialia **37** (10) (1997) 1475-1481

[98Cha] Chang, S.Y.; Fukatsu, A.; Tezuka, H. and Kamio, A.: "Mechanical properties and microstructure of ignition-proof Mg-Ca-Zr system alloys produced by semi-solid squeeze casting" in *Magnesium Alloys and their Applications*, edited by B.L. Mordike and K.U. Kainer, Werkstoff-Informationsgesellschaft, Frankfurt, Germany (1998) 527-532

[98Num] Numakura, H.; Koiwa, M.: "Dislocations in metal and alloys with the hexagonal close-packed structure", Metallurgical Science and Technology **16** (1-2) (1998) 4-19

[98Reg] Regev, M.; Aghion, E.; Rosen, A.; Bamberger, M.: "Creep studies of coarse grained AZ91D magnesium castings", Materials Science and Engineering **A252** (1998) 6-16

[99Ave] ASM Specialty Handbook, *Magnesium and Magnesium Alloys*, edited by M.M. Avedesian and H. Baker, ASM International, Materials Park, Ohio (1999)

[99Sma] Smallman, R.E.; Bishop, R.J.: *Modern physical metallurgy and materials engineering*, sixth edition, Butterworth-Heinemann, Great Britain (1999)

[00Bet] Bettles, C.J.; Dargusch, M.S.: "Creep and bolt-load retention of sand cast Elektron MEZ" in *Magnesium Alloys and their Applications*, edited by K.U. Kainer, Wiley-VCH, Germany (2000) 705-710

[00DIN] DIN 50-125 *DIN-Taschenbuch 19, Materialprüfnormen für metallische Werkstoffe 1,* "Prüfung metallische Werkstoffe: Zugproben", Deutsches Institut für Normung e.V.; Beuth Verlag GmbH, Berlin, Germany (2000) 81-88

[00Gar] Garat, M.; Maenner, L.; Sztur, Ch.: "State of the art of thixocasting" in *6th International Conference on Semi-Solid Processing of Magnesium Alloys and Composites*, edited by G.L. Chiarmetta and M. Rosso, EDIMET, Italy (2000) 187-194

[00Hor] Horie, T.; Iwahori, H.; Seno, Y.; Awano, Y.: "Development of high creep resistant magnesium alloy strengthened by Ca addition" in *Magnesium Technology 2000*, edited by H.I. Kaplan, J. Hryn, and B. Clow, TMS, USA (2000) 261-269

[00Kas] Kassner, M.E.; Pérez-Prado, M.-T.: "Five-power-law creep in single phase metals and alloys", Progress in Materials Science **45** (2000) 1-102

[00Kin] King, J.F.: "Development of practical high temperature magnesium casting alloys" in *Magnesium Alloys and their Applications*, edited by K.U. Kainer, Wiley-VCH, Germany (2000) 15-22

[00Lys] Lysova, E.; Rokhlin, L.; Grytsiv, A.: "Calcium-Magnesium-Zinc" in *Ternary Alloys: a comprehensive compendium of evaluated constitutional data and phase diagrams*, Volume 17, edited by G. Effenberg, F. Aldinger and P. Rogl, MSI (2000) 68-72

[00Pod] Podosek, M.; Lorimer, G.: "The influence of intergranular microstructure of Mg-Zn-RE alloys on properties at elevated temperatures", Archives of Metallurgy **45** (1) 47-55

[00Seq] Sequeira, W.: *The microstructure and mechanical properties of high pressure diecast magnesium alloy AZ91D*, Ph.D. thesis, the University of Queensland, Brisbane, Australia (2000)

[00Suz] Suzuki, M.; Inoue, R.; Sugihara, M.; Sato, H.; Koike, J.; Maruyama, K.; Oikawa, H.: "Effects of Yttrium on creep behaviour and deformation substructures of magnesium", *Materials Science Forum Vols. 350-351*, Trans Tech Publications(2000), Switzerland, 151-156

[00Tzi] Tzimas, E.; Zavaliangos, A.: "A comparative characterization of near-equiaxed microstructures as produced by spray casting, magnetohydrodynamic casting and

the stress induced, melt activated process", Materials Science and Engineering **A289** (2000) 217-227

[00Tzi2] Tzimas, E.; Zavaliangos, A.: "Evolution of near-equixed microstructure in the semi-solid state", Materials Science and Engineering **A289** (2000) 228-240

[00Wal] Walukas, D.; LeBeau, S.; Prewitt, N.; Decker, R.: "Thixomolding® – technology opportunities and practical uses" in *6th International Conference on Semi-Solid Processing of Magnesium Alloys and Composites*, edited by G.L. Chiarmetta and M. Rosso, EDIMET, Italy (2000) 109-114

[00Wag] Wagener, W.; Hartmann, D.: "Feedstock material for semi-solid casting of magnesium" in *6th International Conference on Semi-Solid Processing of Magnesium Alloys and Composites*, edited by G.L. Chiarmetta and M. Rosso, EDIMET, Italy (2000) 301-306

[01Agn] Agnew, S.R.; Yoo, M.H.; Tomé, C.N.: "Application of texture simulation to understanding mechanical behaviour of Mg and solid solution alloys containing Li or Y", Acta Materialia **49** (20) (2001) 4277-4289

[01Gal] Galiyev, A.; Kaibyshev, R.; Gottstein, G.: "Correlation of plastic deformation and dynamic recrystallization in magnesium alloy ZK60", Acta Materialia **49** (2001) 1199-1207

[01Jor] Jorstad, J.: "Practical considerations of processing" in *Science and Technology of Semi-Solid Metal Processing*, edited by Anacleto de Figueredo, North American Die Casting Association, USA, (2001), Ch. 4

[01Kau] Kaufmann, H.; Uggowitzer, P.J.: "Fundamentals of the new rheocasting process for magnesium alloys", Advanced Engineering Materials **3** (12) (2001) 963-967

[01Lar] Larionova, T.V.; Park, W.-W.; You, B-S: "A ternary phase observed in rapidly solidified Mg-Ca-Zn alloys", Scripta Materialia **45** (2001) 7-12

[01Luo] Luo, A.A.; Powell, B.R.: "Tensile and compressive creep of magnesium-aluminium-calcium based alloys" in *Magnesium Technology 2001*, edited by J. Hryn, TMS, USA (2001) 137-144

[01Mor] Moreno, I.P.; Nandy, T.K.; Jones, J.W.; Allison, J.E.; Pollock, T.M.: "Microstructural characterization of a die-cast magnesium-rare earth alloy", Scripta Materialia **45** (2001) 1423-1429

[01Pow] Powell, B.R.; Rezhets, V.; Balogh, M.P.; Waldo, A.: "The relationship between microstructure and creep behaviour in AE42 magnesium die casting alloy" in *Magnesium Technology 2001*, edited by J. Hryn, TMS, USA (2001) 175-181

[01Suz] Suzuki, M.; Sato, H.; Maruyama, K.; Oikawa, H.: “Creep deformation behaviour and dislocation substructures of Mg-Y binary alloys”, Materials Science and Engineering **A319-321** (2001) 751-755

[01Wan] Wang, J.G.; Hsiung, L.M.; Nieh, T.G.; Mabuchi, M.: “Creep of a heat treated Mg-4Y-3RE alloy”, Materials Science and Engineering **A315** (2001) 81-88

[02Agn] Agnew, S.R.; Horton, J.A.; Yoo, M.H.: “Transmission electron microscopy investigation of <c+a> dislocations in Mg and α-solid solution Mg-Li alloys”, Metallurgical and Materials Transactions **33A** (2002) 851-858

[02AST] ASTM Standard E112, 2002 “Standard Test Methods for Determining Average Grain Size”, ASTM International, West Conshohocken, PA, 2002, DOI: 10.1520/E0112-02

[02Bam] Bamberger, M.; Jardim, P.M.; Solórzano, G.; Sande, J.V.: “Precipitation hardening in Mg-Zn-Ca alloys” in *Magnesium Technology 2002*, edited by H.I. Kaplan, TMS, USA (2002) 75-80

[02Cac] Cáceres, C.H.; Blake, A.: “The strength of concentrated Mg-Zn solid solutions”, Physica Status Solidi **A194** (1) (2002) 147-158

[02Che] Chen, J.Y.; Fan, Z.: “Modelling of rheological behaviour of semisolid metal slurries Part 1 – Theory”, Materials Science and Technology **18** (2002) 237-242

[02Che2] Chen, T.J.; Hao, Y.; Sun, J.: “Microstructural evolution of previously deformed ZA27 alloy during partial remelting”, Materials Science and Engineering **A337** (2002) 73-81

[02Fan] Fan, Z.: “Semisolid metal processing”, International Materials Reviews **47** (2) (2002) 49-85

[02Fan2] Fan, Z.; Chen, J.Y.: “Modelling of rheological behaviour of semisolid metal slurries Part 2 – Steady state behaviour”, Materials Science and Technology **18** (2002) 243-249

[02Fan3] Fan, Z.; Chen, J.Y.: “Modelling of rheological behaviour of semisolid metal slurries Part 4 – Effects of particle morphology”, Materials Science and Technology **18** (2002) 258-267

[02Fin] Finkel, A.; Shepeleva, L.; Bamberger, M.; Rabkin, E.: “The effect of exposure to elevated temperatures on the microstructure and hardness of Mg-Ca-Zn alloy” in *Magnesium Technology 2002*, edited by H.I. Kaplan, TMS, USA (2002) 81-86

[02Lee] Lee, Young: *Grain refinement of magnesium*, Ph.D. thesis, the University of Queensland, Brisbane, Australia (2002)

[02Mar] Maruyama, K.; Suzuki, M.; Sato, H.: “Creep strength of magnesium-based alloys”, Metallurgical and Materials Transactions **33A** (2002) 875-882

[02Mys] Myshlyaev, M.M.; McQueen, H.J.; Mwembela, A.; Konopleva, E.: “Twinning, dynamic recovery and recrystallization in hot worked Mg-Al-Zn alloy”, Materials Science and Engineering **A337** (2002) 121-133

[02Mor] Mordike, B.L.: “Creep resistant magnesium alloys”, Materials Science and Engineering **A324** (2002) 103-112

[02Pet] Pettersen, K.; Bakke, P.; Albright, D.: “Magnesium Die Casting Alloy Design” in *Magnesium Technology 2002*, edited by H.I. Kaplan, TMS, USA (2002) 241-246

[02Yoo] Yoo, M.H.; Morris, J.R.; Ho, K.M.; Agnew, S.R.: “Nonbasal deformation modes of HCP metals and alloys: Role of dislocation source and mobility”, Metallurgical and Materials Transactions **33A** (2002) 813-822

[02Wei] Weiss, D.; Kaya, A.A.; Aghion, E.; Eliezer, D.: “Microstructure and creep properties of a cast Mg-1.7%wt rare earth-0.3%wt Mn alloy”, Journal of Materials Science **37** (2002) 5371-5379

[03Bet] Bettles, C.J.; Venkatesan, K.; Nie, J.F.: “Microstructure and mechanical properties of MEZ casting alloy”, *Materials Science Forum Vols. 419-422* (2003) 273-278

[03Fin] Finkel, A.; Shepeleva, L.; Bamberger, M.; Rabkin, E.: “The effect of exposure to elevated temperatures on the microstructure and hardness of Mg-Ca-Zn-Sn alloy compared with Mg-Ca-Zn alloy” in *Magnesium Technology 2003*, edited by H.I. Kaplan, TMS, USA (2002) 189-194

[03Gup] Gupta, Chiranjib Kumar: *Chemical Metallurgy: Principles and Practice*, Wiley-VCH, Weinheim (2003) pp. 68

[03Hu] Hu, H.; Yu, A.; Li, N.; Allison, J.E.: “Potential magnesium alloys for high temperature die cast automotive applications: a review”, Materials and Manufacturing Processes **18** (5) (2003) 687-717

[03Jor] Jorstad, J.L.; Apelian, D.; Makhlouf, M.: “Novel, slurry-based, semi-solid processing routes” in *Proceedings f the 1st International Light Metals Technology Conference 2003*, edited by Arne Dahle, Brisbane, Australia (2003) 109-114

[03Kai] Kainer, K.U.; Benzler, T.: “Squeeze casting and thixocasting of magnesium alloys” in *Magnesium - alloys and technologies*, edited by K.U. Kainer, Wiley VCH Verlag GmbH, Weinheim (2003) 56-71

[03Kau] Kaufmann, H.; Uggowitzer, P.J.: “The latest development of new rheocasting for Al- and Mg-alloys”” in *Proceedings f the 1st International Light Metals Technology Conference 2003*, edited by Arne Dahle, Brisbane, Australia (2003) 115-119

[03Koi] Koike, J.; Kobayashi, T.; Mukai, T.; Watanabe, H.; Suzuki, M.; Maruyama, K.; Higashi, K.: “The activity of non-basal slip systems and dynamic recovery at room temperature in fine-grained AZ31B magnesium alloys”, Acta Materialia **51** (2003) 2055-2065

[03Mor] Moreno, I.P.; Nandy, T.K.; Jones, J.W.; Allison, J.E.; Pollock, T.M.: “Microstructural stability and creep of rare-earth containing magnesium alloys”, Scripta Materialia **48** (2003) 1029-1034

[03Rok] Rokhlin, L.L.: *Magnesium alloys containing rare earth metals: structure and properties*, Taylor and Francis, London (2003)

[03Pek] Pekguleryuz, M.O.; Kaya, A.A.: “Creep resistant magnesium alloys for power train applications”, Advanced Engineering Materials **5** (12) (2003) 866-878

[03Pin] Ping, D.H.; Hono, K.; Nie, J.F.: “Atom probe characterization of plate-like precipitates in a Mg-RE-Zn-Zr casting alloy”, Scripta Materialia **48** (2003) 1017-1022

[03Sie] Siederslebnen, M.: “Vacuum die casting of magnesium parts with high pressure” *in Magnesium - alloys and technologies*, edited by K.U. Kainer, Wiley VCH Verlag GmbH & Co. KGaA, Weinheim (2003) 45-48

[03Sit] Sitdikov, O.; Kaibyshev, R.; Sakai, T.: “Dynamic recrystallization based on twinning in coarse-grained magnesium” in *Materials Science Forum 419-422*, Trans Tech Publications, Switzerland (2003) 521-526

[03Suz] Suzuki, M.; Kimura, T.; Koike, J.; Maruyama, K.: “Strengthening effect of Zn in heat resistant Mg-Y-Zn solid solution alloys”, Scripta Materialia **48** (2003) 997-1002

[03Vil] Villa Fanjul, F.; Srimanosaowapak, S.; McNee, K.R.; Greenwood, G.W.; Jones, H.: ”The effect of Nd substitution for mischmetal on creep performance of Mg-2.5 RE-0.35 Zn-0.3 Mn-0.03 Zr alloy”, Zeitschrift für Metalllkunde **94** (1) (2003) 25-29

[03Wil] Wilson, R.; Bettles, C.J.; Muddle, B.C.; Nie, J.F.: “Precipitation hardening in Mg-3 wt%Nd(-Zn) casting alloys”, *Materials Science Forum Vols. 419-422* (2003) 267-272

[04Agh] Aghion E.; Bronfin, B.: “Physical metallurgy of magnesium alloys” in *Magnesium alloys – Science, Technology and Applications*, edited by E. Aghion and E. Eliezer, Israeli Consortium for the Development of Magnesium Technologies, Israel (2004) Ch.1, 7-43

[04Agu] Aguilar, J.; Fehlbier, M.; Ludwig, A.; Bührig-Polaczek, A.; Sahm, P.R.: “Non-equilibrium globular microstructure suitable for semisolid casting of light metal alloys by rapid slug cooling technology (RSCT)”, Materials Science and Engineering **A375-377** (2004) 651-655

[04Bel] Bell, A.; Srivatava, V.; Greenwood, G.W.; Jones, H.: “The creep performance of a sand-cast Mg-2.8Nd-0.8Zn-0.5Zr-0.3Gd at 241 to 262°C”, Zeitschrift für Metallkunde **95** (5) (2004) 369-371

[04Bet] Bettles, C.J.; Gibson, M.A.; Venkatesan, K.: “Enhanced age-hardening behaviour in Mg-4 wt.% Zn micro-alloyed with Ca”, Scripta Materialia **51** (2004) 193-197

[04Gill] Gill, L.; Lorimer, G.W.; Lyon, P.: “Microstructure/property relationships of three Mg-RE-Zn-Zr alloys” in *Magnesium: Proceedings of the 6th International Conference on Magnesium Alloys and their Applications*, edited by K.U. Kainer, Wiley-VCH, Germany (2004) 421-426

[04Kle] Kleiner, S.; Beffort, O.; Uggowitzer, P.J.: “Microstructure evolution during reheating of an extruded Mg–Al–Zn alloy into the semisolid state”, Scripta Materialia **51** (5) (2004) 405-410

[04Kre] Kree, V.; Bohlen, J.; Letzig, D.; Kainer, K.U.: “The metallographic examination of magnesium alloys”, Praktische Metallographie **41** (5) (2004) 233-246

[04Jar] Jardim, P.M.; Solórzano, G.; Vander Sande, J.B.: “Second phase formation in melt-spun Mg-Ca-Zn alloys”, Materials Science and Engineering **A381** (2004) 196-205

[04Smo] Smola, B.; Stulíkova, I.; Pelcová, J.; Mordike, B.L.: “Significance of stable and metastable phases in high temperature creep resistant magnesium-rare earth base alloys”, Journal of Alloys and Compounds **378** (2004) 196-201

[04Suz] Suzuki, M.; Kimura, T.; Koike, J.; Maruyama, K.: “Effects of zinc on creep strength and deformation substructures in Mg-Y alloy”, Materials Science and Engineering **A387-389** (2004) 706-709

[04Zil] Zilberov, A.; Gören-Muginstein, G.R.; Bamberger, M.: “High temperature behaviour of a new Mg-Ca-Zn alloy” in *Magnesium: Proceedings of the 6th International Conference on Magnesium Alloys and their Applications*, edited by K.U.Kainer, Wiley-VCH, Germany (2004) 134-139

[05Agn] Agnew, S.R.; Duygulu, Ö.: “Plastic anisotropy and the role of non-basal slip in magnesium alloy AZ31B”, International Journal of Plasticity **21** (2005) 1161-1193

[05Bak] Bakke, P.; Westengen, H.: “The role of rare earth elements in structure and property control of magnesium die casting alloys” in *Magnesium Technology 2005*, edited by N.R. Neelameggham, H.I. Kapplan, and B.R. Powell, TMS (2005) 291-296

[05Bla] Blake, A.H.; Cáceres, C.H.: “Solid solution effects on the tensile behaviour of concentrated Mg-Zn alloys” in *Magnesium Technology 2005*, edited by N.R. Neelamegghan, H.I. Kaplan, and B.R. Powell, TMS (2005) 403-407

[05Boe] Boehlert, C.J.; Knittel, K.: “The microstructure, tensile properties,and creep behaviour of Mg-Zn alloys containing 0-4.4 wt.% Zn”, Materials Science and Engineering **A417** (2006) 315-321

[05Cze] Czerwinski, F.: “Semisolid processing and its application to magnesium alloys” in *Magnesium Technology 2005*, edited by N.R. Neelamegghan, H.I. Kaplan, and B.R. Powell, TMS (2005) 341-344

[05DIN] DIN EN ISO 6507-1:2005, *Metallische Werkstoffe* - Härteprüfung nach Vickers - Teil 1: Prüfverfahren, (ISO 6507-1:2005), Deutsches Institut für Normung e.V.; Beuth Verlag GmbH, Berlin, Germany (2006)

[05Fan] Fan, Z.: “Development of the rheo-diecasting process for magnesium alloys”, Materials Science and Engineering **A413-414** (2005) 72-78

[05Gao] Gao, X.; Zhu, S.M.; Muddle, B.C.; Nie, J.F.: “Precipitation-hardened Mg-Ca-Zn alloys with superior creep resistance”, Scripta Materialia **53** (2005) 1321-1326

[05Kli] Kliauga, A.M.; Ferrante, M.: “Liquid formation and microstructural evolution during re-heating and partial melting of an extruded A356 aluminium alloy”, Acta Materialia **53** (2005) 345-356

[05Nie] Nie, J.F.; Gao, X.; Zhu, S.M.: “Enhanced age hardening response and creep resistance of Mg-Gd alloys containing Zn”, Scripta Materialia **53** (2005) 1049-1053

[05Seo] Seo, P.K.; Kang, C.G.: “The effect of raw material fabrication process on microstructural characteristics in reheating process for semi-solid forming”, Journal of Materials Processing Technology **162-163** (2005) 402-409

[05Wei] Wei, L.Y.; Dunlop, G.L.; Westengen, H.: “Precipitation hardening of Mg-Zn and Mg-Zn-RE alloys“, Metallurgical and Materials Transactions **26A** (1995) 1705-1716

[05Zal] Žaludová, N.: “Mg-RE alloys and their applications” in *WDS'05 Proceedings of Contributed Papers: Part III - Physics*, edited by J. Safrankova, Matfyzpress, Prague (2005) 643-648

[06Bam] Bamberger, M.; Lev, G.; Vander Sande, J.B.: “Precipitation hardening in Mg-Ca-Zn alloys”, Metallurgical and Materials Transactions **37A** (2006) 481-487

[06Fin] Finkel, A.; Shepeleva, L.; Bamberger, M.; Rabkin, E.: “The effect of exposure to elevated temperatures on the microstructure and hardness of Mg-Ca-Zn alloy”, Zeitschrift für Metallkunde **97** (1) (2006) 64-71

[06Lev] Levi, G.; Avraham, S.; Zilberov, A.; Bemberger, M.: “Solidification, solution treatment and age hardening of an Mg - 1.6 wt. % Ca - 3.2 wt. % Zn alloy”, Acta Materialia **54** (2006) 523-530

[06Fri] Friedrich, H.E.; Mordike, B.L.: *Magnesium Technology: Metallurgy, Design Data, Applications*, Springer-Verlag Berlin Heidelberg (2006)

[07Kie] Kielbus, A.: “Microstructure and mechanical properties of Elektron 21 alloy after heat treatment”, Journal of Achievements in Materials and Manufacturing Engineering **20** (1-2) (2007) 127-130

[07Kie2] Kielbus, A.: “Microstructure of Elektron 21 magnesium alloy after heat treatment” in *Magnesium: Proceedings of the 7th International Conference on Magnesium Alloys and their Applications*, edited by K.U.Kainer, Wiley-VCH, Germany (2007) 459-465

[07Li] Li, Q.; Wang, Q.; Wang, Y.; Zeng, X.; Ding, W.: “Effect of Nd and Y addition on microstructure and mechanical properties of as-acst Mg-Zn-Zr alloy”, Journal of Alloys and Compounds **427** (2007) 115-123

[07Neu] Neubert, V.; Stulíková, I.; Smola, B.; Mordike, B.L.; Vlach, M.; Bakkar, A.; Pelcová, J.: “Thermal stability and corrosion behaviour of Mg-Y-Nd and Mg-Tb-Nd alloys”, Materials Science and Engineering **A462** (2007) 329-333

[07Smo] Smola, B.; Stulíková, I.; Pelcová, J.; Žaludová, N.: “Phase composition and creep behaviour of Mg-RE-Mn alloys with Zn addition” in *Magnesium: Proceedings of*

the 7th International Conference on Magnesium Alloys and their Applications, edited by K.U.Kainer, Wiley-VCH, Germany (2007) 67-73

[08Kau] Kaufmann, H.; Uggowitzer, P.J.: *Metallurgy and Processing of High-Integrity Light Metal Pressure Castings*, Schiele and Schön GmbH, Berlin (2007) Ch. 9

[08Yan] Yan, J.; Sun, Y.; Xue, F.; Xue, S.; Tao, W.: "Microstructure and mechanical properties in cast magnesium-neodymium binary alloys", Materials Science and Engineering **A476** (2008) 366-371

[09Zho] Zhou, T.; Chen, D.; Chen, Z.H.; Chen, J.H.: "Investigation on microstructures and properties of rapidly solidified Mg-6wt.%Zn-5wt.%Ca-3wt.%Ce alloy", Journal of Allloys and Compounds **475** (1-2) (2009) L1-L4

[10Yan] Yang, K.; Nagasekhar, A.V.; Caceres, C.H.: "The skin effect in a high pressure die cast Mg-9%Al alloy", Advanced Materials Research **97 - 101** (2010) 743-747

[10Yan2] Yang, K.; Nagasekhar, A.V.; Caceres, C.H.; Easton, M.A.: "The skin effect in an Mg-RE high pressure die cast alloy", *Materials Science Forum 654 - 656* (2010) 691-694

[11Wik] http://de.wikipedia.org/wiki/Mischmetall